AN ABSTRACT OF THE DISSERTATION OF

Ismail Hakki Uluer for the degree of Doctor of Philosophy in Electrical and Computer Engineering presented on December 9, 2022.

Title: Wireless Microwave Sensing in Environmental and Biomedical Applications

Abstract approved:

____

Thomas Weller

This dissertation studies two different wireless microwave sensing applications in the subjects of environmental monitoring and biomedical devices. The environmental sensing application presents a design of novel wireless sensor node configurations. These nodes are intended to be used specifically in a built environment of railroad track ballast for its health monitoring. Real-time, low-cost, and long-term health monitoring in the railroad track is vital for the prevention of infrastructure failures that can cause accidents or disrupt train operations. The critical parameters of health monitoring in railroad tracks are moisture level and displacement of the railroad track components. Therefore, the experimental work was done to develop a battery-free, mechanically tunable, and narrowband wireless sensor that can be used to monitor railroad track ballast moisture level, along with an interrogator. And the moisture level information is obtained by tracking the attenuation of the signal in the propagation environment between the sensor and the interrogator. This environment comprises a heterogeneous and multi-dielectric composition of ballast, fouling material, and

moisture. To approximate the actual moisture level, a dielectric mixing model is developed and presented. Additionally, a novel interferometric measurement technique that employs a pair of sensor nodes is proposed to localize the sensors and measure the displacement. The results that are in very good agreement with the analytical calculations reveal that the proposed model and technique have shown promise to accurately predict the moisture level and displacement in the real environment.

The biomedical microwave sensing application is studied in the remaining part of the dissertation. An end-fire dielectric rod antenna (DRA) is proposed as a heating device for integration with an array of electroporation electrodes in order to enable efficient delivery of DNA into the cells that comprise subcutaneous tumors. A 5-7 °C temperature elevation of tumors that are located near the fat-muscle boundary and 3-7 mm below the skin surface and 7.5 mm in diameter can be achieved in a short period of time without damaging surrounding tissues. This capability is demonstrated through a combination of a directional antenna applicator operating at 8 GHz, and utilization of forced air cooling of the outer surface (skin layer). The directionality of the antenna is improved by cladding its high permittivity core with 3D printed, low permittivity dielectric material. Experimental data using a pork skin-fat-muscle tissue show that the desired temperature elevation at the tumor location is obtained after 2.5 W RF illumination for 3 minutes, which is in good agreement with electro-thermal simulations. With the addition of realistic human body model parameters to the same simulation setup, the results indicate that tumors can be uniformly heated with 3 minutes of illumination at 2.5 W input power while keeping the surrounding healthy tissues at a safe temperature. Moreover, this applicator is able to treat different sizes of tumors, up to 16 mm in diameter, by just attaching proposed thin and planar diverging lenses to the front end of a DRA. The desired 5-7 °C temperature elevation of the tumors is achieved in 3 minutes by applying 2.1-3.6 W input power depending on the size of the tumor.

Wireless Microwave Sensing in Environmental and Biomedical Applications

by
Ismail Hakki Uluer

A DISSERTATION

submitted to

Oregon State University

in partial fulfillment of
the requirements for the
degree of

Doctor of Philosophy

Presented December 9, 2022
Commencement June 2023

Doctor of Philosophy dissertation of Ismail Hakki Uluer presented on December 9, 2022.

APPROVED:

Major Professor, representing Electrical and Computer Engineering

Head of the School of Electrical Engineering and Computer Science

Dean of the Graduate School

I understand that my dissertation will become part of the permanent collection of Oregon State University libraries. My signature below authorizes release of my dissertation to any reader upon request.

Ismail Hakki Uluer, Author

ACKNOWLEDGEMENTS

My Ph.D. journey started at the University of South Florida and ends at the Oregon State University after transferring along with my advisor, Dr. Thomas Weller. Besides difficulties with moving across the country and changing the research environment, the global pandemic hit and caused disruptions that negatively impacted my studies. Nevertheless, Dr. Weller's continuous support, understanding, and encouragement helped overcome all these challenges throughout this journey. His deep technical insight and patiently guidance always amazed me and incredibly enhanced my academic and professional development. I sincerely thank him for everything.

I would also like to thank my committee members, Dr. Jeff Frolik, Dr. Andreas Weisshaar, Dr. Matthew Johnston, and Dr. John Parmigiani for their service and constructive comments on my dissertation. Special thanks to Dr. Mark Jaroszeski and Dr. Joshua Gess who broaden my knowledge outside of my field and contribute to my research. Sincere thanks to Ibrahim Nassar whose past work pioneered my studies.

I am eternally grateful to the Republic of Türkiye whose generous financial support enabled me to get this high-quality graduate education in the US.

Many thanks to my family members, Ayse, Mehmet, Fatma, Abdullah, Zeynep, Mahmud, and Meryem Uluer, and Hasan and Imran Aydemir for their continuous support. I had an enjoyable time and unforgettable moments thanks to my colleagues and great friends: Omer Firat, Arya Menon, Derar Hawatmeh, Esat Ankarali, Mostafa Essawy, Yavuz Gurbuz, Ahmet Topcuoglu, Sinasi Cetinkaya, Mustafa Bozkus, Fatih Sen, Mehmet Yuksel, Erkan Babat, Muhammet Sahin, and Abdulkadir Alic.

Finally, and most importantly, I thank Allah (God) for all the blessings. All praises are due to him, Alhamdulillah!

TABLE OF CONTENTS

TABLE OF CONTENTS (Continued)

Page

TABLE OF CONTENTS (Continued)

Page

LIST OF FIGURES

LIST OF FIGURES (Continued)

LIST OF FIGURES (Continued)

Figure Page

LIST OF TABLES

LIST OF APPENDICES

Appendix | Page

DEDICATION

To my beloved wife, Rabiya, for her unconditional love, continual support, and tolerating my excessive study times and stress. She is the secret behind my success.

To the light of my eyes, my daughter Feride, for always giving me positive energy and making me happy.

To my dear father and beloved mother, Dr. Ihsan and Hatice Uluer, for being the perfect role model, encouraging me to study Ph.D. in the US, having a strong belief in my success, and for continuous support and love.

Chapter I :

Introduction

When electromagnetic waves travel through a lossy dielectric medium, some fraction of the power is absorbed and dissipated as heat. Although this situation can create challenges for many radio frequency (RF) applications, e.g., communication systems, the phenomenon can be beneficial in some circumstances and can be used as part of a sensing and material characterization strategy in others. As an example, microwave heating is one of the well-known applications that has been used in a variety of different purposes such as cooking (microwave ovens), food sterilization, and cancerous tumor treatment. Another example is in environmental sensing applications. For instance, the moisture content can be extracted from tracking the level of RF power dissipation in the environment.

This dissertation studies two different RF applications in lossy dielectric mediums: (1) environmental sensing, (2) cancerous tumor treatment. The background and motivation, technical challenges and solution approaches, and the specific contributions are explained for both studies in the following sections.

1.1. Environmental Sensing Studies

1.1.1. Motivation

The structural integrity of a built environment degrades over time for a variety of different natural or human-made reasons, such as weathering, erosion, landslides, excessive loading, material deformations, and design failures [1]. Monitoring the integrity continuously can help to ensure timely failure detection and planning for necessary maintenance and/or repair. The existing manual inspection methods typically require significant human effort; thus, they are expensive, time-consuming, and may lack sufficient accuracy. Moreover, the inspection frequencies of such methods tend to be limited, which restricts early detection of failure.

Non-destructive inspection methods with wireless sensors that are embedded in the environment have shown promise to overcome the issues with manual inspections and enable continuous sensing with higher accuracy [2]. One of the main challenges with employing these sensors is the power source requirement to continue their operation. The active sensors, e.g., radar backscatter tags [3], supply the necessary power from a battery, so their operation period depends on the battery's lifetime, and maintenance is necessary after that (the estimated battery life is 3 years [3]). The battery itself and the required field maintenance process are not cost-effective as well. Therefore, low-cost and long-term fully passive sensors have gained more attraction over the past years in sensing applications. The required power for these sensors can be provided by either RF energy harvesting [4] or an external RF source (an interrogator) [5]. Due to the lossy nature of the environments of interest, the embedded sensors typically cannot capture enough ambient power for energy harvesting. Thus, the latter method has advantages for embedded sensing applications.

Four types of passive sensors have been mainly studied for environmental sensing: (1) passive Radio Frequency Identification (RFID), (2) Surface Acoustic Wave (SAW), (3) Resonance Circuit (RC), and (4) Frequency Doubling Reflectenna (FDR). RFID and SAW sensors have been used for embedded monitoring [6,7,8] due to their small size since a single antenna is used to operate. Compared with RFID tags, SAW tags are more challenging to design (having a transducer and reflectors) and expensive, but their communication range is much higher than RFID tags. The time delay between the received and transmitted signals created in the SAW sensor helps to improve its range. The RC sensors are ultra-low cost since they are comprised of an antenna and an RC circuit that does not require any additional components. However, their communication range is very limited, and measurements are sensitive to antenna and RC circuit alignment [9]. Finally, the FDR (also referred to as a harmonic transponder) consists of two antennas, RX and TX, and a non-linear element, a Schottky diode, in between them. So, it is low-cost, but larger in size than RFID sensors [10].

Table 1.1 Comparison of passive sensors used for environmental sensing.

	RFID	SAW	RC	FDR
Size	Small	Small	Large	Large
Communication Range	Short	Long	Short	Long
Operation Frequency	Mono	Mono	Mono (Shifts)	Double
Cost	Low	High	Low	Low

The most important advantage of the FDR for environmental sensing is the long communication range compared to the mono-frequency transponders. The simple working principle of the FDR is that the RX antenna receives an f_0 signal from the interrogator and transmits it to the input of the diode. The diode generates the harmonics, and the second harmonic ($2f_0$) signal is radiated back (also called backscattered signal) to the interrogator by the TX antenna. The transmit and receive signal frequency difference reduces the backscatter and ground clutter interference dramatically, which results in improving the read range.

The second important advantage is the narrow-band operation and associated sensitivity to external stimuli-induced changes in the FDR transfer function, which extends its dynamic range [11]. These are particularly important aspects of sensing with embedded sensors in lossy environments.

In this dissertation, the passive FDR nodes are designed to be used specifically in a built environment of railroad track ballast for its health monitoring. Ballast is a principal component of the track structure. It performs several important functions:

- transmit and distribute the load to the subgrade;
- restrain the track vertically, laterally, and longitudinally;
- provide adequate drainage for the track; and
- maintain proper track geometry.

One of the main problems in the ballast and the proposed solution technique with the FDR are modeled in Fig. 1.1 When fouling (dust or dirt) fills the voids between ballast stones over time, the fouling starts holding the moisture that would otherwise drain away. Excessive moisture level in the fouling causes displacement of the ballast under the train load. Therefore, besides monitoring the moisture, continuous measurement of the displacement in the railroad ballast is extremely important for preventing infrastructure failures that can cause accidents or disrupt train operations.

Methods to evaluate subsurface conditions of ballast exist. One example is Ground Penetrating Radar (GPR) [12]. GPR systems are usually mounted on a moving platform and provide assessment for a given point in time, subject to testing frequencies. Traditional wayside monitoring, on the other hand, provides continuous measurement but is expensive and highly localized [13]. However, the presented energy-efficient, low-cost, and long-term wireless technology with RF frequency doubling reflectenna sensors has the capability of regularly and autonomously measuring and characterizing these parameters, while operating along with an interrogator. A drone-based interrogator concept is considered for further reducing human effort in the measurements.

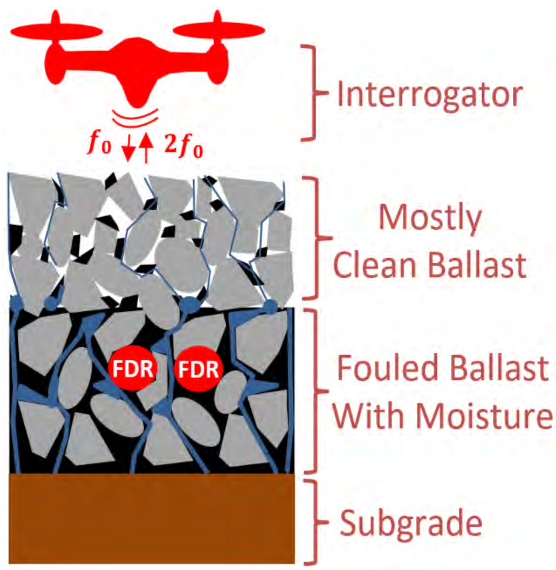

Figure 1.1 Ballast cross-section and two FDR sensors being interrogated with an RF signal in ballast.

1.1.2. Approaches to the Technical Challenges

Due to the highly lossy nature of the ballast environment, the read range extension of the FDR is an important technical challenge. The read range is dependent heavily on the frequency of operation, the diode, TX and RX antenna designs, and their impedance matching to the input and output of the diode. A lower operation frequency provides a higher read range due to lower path loss as the signal travels between the interrogator and the FDR. For example, if the minimum detectable signal is 125 dBm, the expected read range in free space is approximately ~60 m for the operation frequency of 2.4 GHz while it is ~120 m for 1.2 GHz and ~160 m for 915 MHz. However, this results in a larger FDR size which may not be preferred if there is a size constraint. The power dissipated during f_0 to $2f_0$ frequency conversion by the diode varies depending on the diode parameters. So, it is important to use the optimum diode in the FDR design that provides highest conversion efficiency at the input power level of interest. The receiver and transmitter antennas occupy most of the FDR space, thus they are expected to be small in size to be used in environmental sensing. However, shrinking their size reduces the radiation efficiency and complicates impedance matching. 3D miniaturized dipole antennas have shown promise in providing sufficient radiation efficiency by using the available volume effectively [14]. Their omnidirectional radiation pattern is especially drawing interest for sensing applications. Therefore, the read range extension for FDRs with miniaturized dipole antennas is studied in this dissertation.

The moisture level in the ballast environment can be determined by analyzing the difference between transmitted and received signals. Based on the moisture content, the dielectric properties of the environment change, resulting in varying received signal attenuation. For example, the higher moisture content has a higher permittivity and so greater signal loss. However, the complex permittivity of a heterogeneous and multi-dielectric environment does not increase linearly with the moisture content. As an example, according to [15], the soil and water mixture's dielectric constant (ε_r') increases gradually while the loss tangent ($\varepsilon_r''/\varepsilon_r'$) sharply increases from 0% to 5%

and then reduces slowly and stabilizes as seen in Fig. 1.2. Since dielectric mixing equations in the literature [16-23] underestimate the dielectric properties as noted in Chapter III, a semi-empirical dielectric mixing model is recommended in [15]. Therefore, the same needs to be studied for the ballast environment comprised of ballast, fouling (coal dust), moisture (water), and void (air). While this model enables the extraction of the moisture content from the complex permittivity of the mixture, it would also allow a reverse model which is predicting the dielectric properties of the environment from known moisture content.

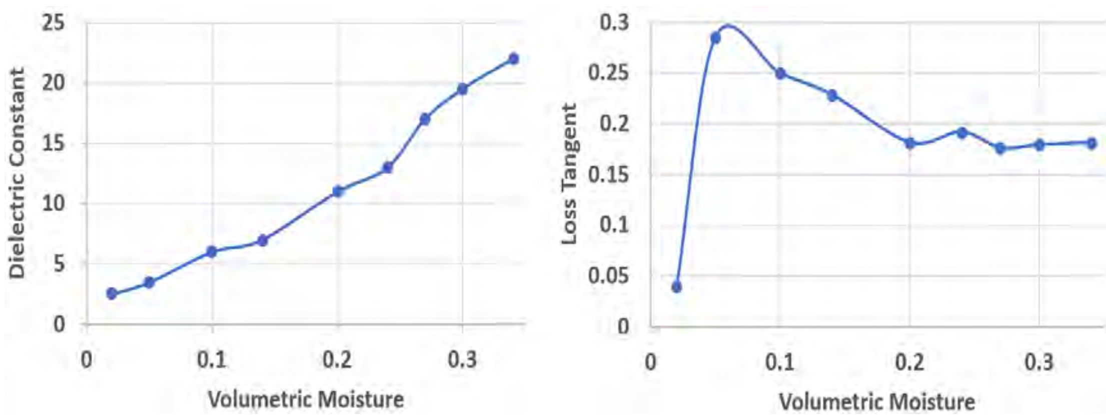

Fig. 1.2 Dielectric properties of soil and water mixture [13].

Figure 1.3 Dielectric mixing model and moisture level prediction relationship.

Displacement monitoring with wireless sensors is another technical challenge. A variety of different active and passive sensors has been studied for displacement monitoring such as sensors of global positioning system (GPS) [24], radars [25], and RFID tags [26]. But, their viability issues for the embedded environments are addressed in section 1.1.1.

A novel interferometric approach by employing a pair of FDRs is proposed in this dissertation. The basic principle of this technique relies on the received constructive and destructive interferences when two FDRs are interrogated from different angles. The peak and null locations in the received signal can help predict the separation distance of the FDRs and so the displacement. The same approach can also be applied to find the sensor locations with sufficient accuracy.

1.1.3. Contributions

The following contributions have been made in the field of environmental sensing:

1. The design and characterization of a mechanically tunable and narrowband miniaturized FDR sensor with improved efficiency is proposed and explained in detail.
2. A semi-empirical dielectric mixing model is developed to approximate the moisture content in the heterogeneous and multi-dielectric railroad ballast environment.
3. A novel interferometric localization measurement technique is proposed by using a pair of FDRs that has higher accuracy than GPS.
4. A novel interferometric displacement measurement technique is proposed by using a pair of FDRs that has high accuracy.

1.2. Cancerous Tumor Treatment Studies

1.2.1. Motivation

Gene therapy method has gained tremendous attention in cancerous tumor treatment over the past 20 years. The technique may allow doctors to treat tumors by inserting a gene into the patient's cells instead of using drugs or surgery. Early studies for skin cancerous treatment showed that applying infrared radiation to heat the tumor and bring its temperature 5-6 ºC above the human body temperature (37 ºC) helps improving the efficiency of the gene therapy method significantly. Fig. 1.4. illustrates the treatment process that starts with the injection of DNA encapsulated in a vector into the skin. It continues with local heating by applying the infrared radiation, ending with applying DC pulses to weaken the cell membrane's barrier [27]. However, infrared radiation is not a practical method for tumors within deeper tissues due to its lack of penetration depth, but microwave radiation is. Thus, this study focused on developing a microwave applicator to assist the gene therapy technique.

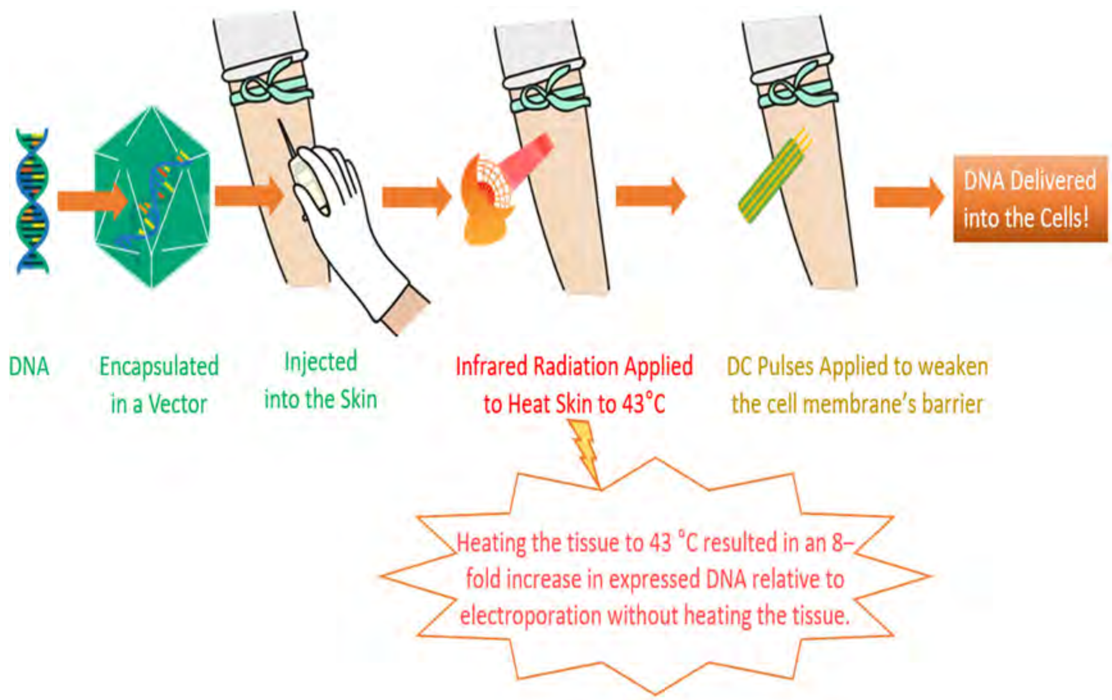

Figure 1.4 The tumor treatment process of heat and electroporation-based DNA delivery that provide higher efficiency.

1.2.2. Approaches to the Technical Challenges

One of the main challenges is finding the optimum microwave applicator based on tumor treatment requirements. There are mainly three key requirements that should be considered during the applicator selection, as seen in Fig. 1.5. If the application necessities faster heating time, then the directionality, impedance matching between the applicator and the human body should be improved, or the input power level can be increased. The microwave radiation beam size should be aligned with the tumor size for heating more efficiently. The penetration depth defines how deep the microwave energy can travel in the human body, and it is inversely proportional to the operating frequency. Therefore, based on the location of tumor in interest, the operation frequency needs to be determined and the applicator is designed.

In this dissertation, tumors that are located near the fat-muscle boundary and 3-7 mm below the skin surface are interested in heating by 5 to 7 ºC above the human body temperature in a short period of time without damaging surrounding tissues. Additionally, the microwave applicator is expected to integrate into a six-needle electrode that is used for the gene therapy application to apply DC pulses. A variety of different microwave applicators has been studied to elevate the temperature of tumors in human body [28-32]. However, none of these applicators are able to

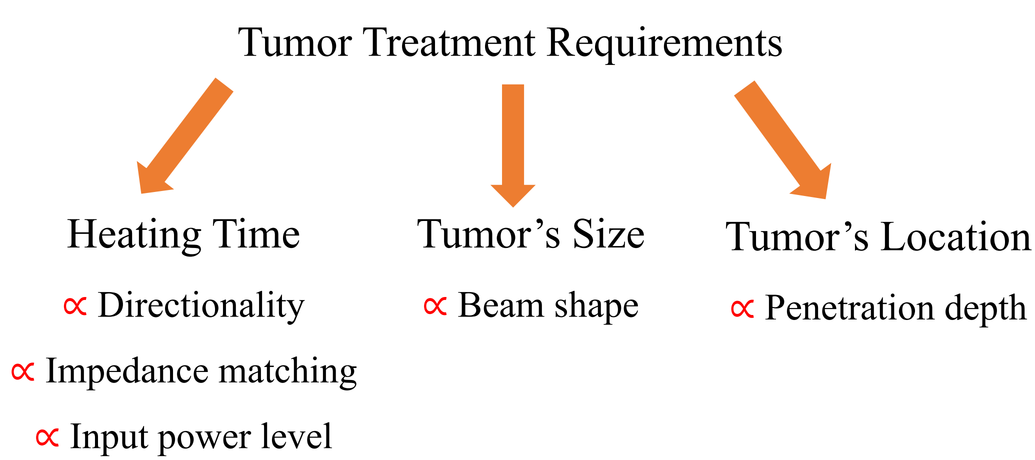

Figure 1.5 Microwave applicator selection criterion based on the tumor treatment requirements.

provide these treatment requirements. An end-fire dielectric rod antenna (DRA) proposed herein can integrate into the electrode and concentrates the microwave energy into the confined tumor location in a short period of time.

One of the limitation with the proposed antenna is being able to treat only a certain size of tumors, which is around 7.5 mm in diameter. In order to treat tumors of different sizes, a new design of the antenna would generally be required. However, an alternative approach is proposed by adding a thin layer dielectric lens to the front-end of DRA, which modifies the beam shape and so the heated area.

1.2.3. Contributions

The following contributions have been mainly made in a novel cancerous tumor treatment study:

1. Design and characterization of a 3D printed dielectric rod antenna that can integrate into the six-needle electrode and assist the electroporation-mediated DNA delivery method.
2. Creation of a multi-physics simulation model to analyze the temperature variation on the human body during RF illumination.
3. Design and characterization of thin dielectric lenses that can be attached to the front end of the antenna to treat different sizes of tumors with the same applicator.

1.3. Dissertation Organization

The dissertation is comprised of seven chapters. The motivation, background, and literature review parts are presented in Chapter I. The FDR design steps, three different FDR designs, temperature and bandwidth analysis, and two different mechanical tunability techniques are presented in Chapter II. A semi-empirical dielectric mixing model for moisture content approximation in railroad ballast is presented in Chapter III. Novel interferometric localization and displacement measurement approaches are explained in Chapter IV. The design, characterization, and testing of a 3D printed dielectric rod antenna to assist a novel cancerous treatment technique are presented in Chapter V. Design and characterization of thin dielectric lenses that can be attached to the front end of the antenna to treat different sizes of tumors with the same applicator is discussed in Chapter VI. And the conclusions are given in the final chapter.

Chapter II :

Battery-Free Wireless Sensor Design

2.1. Introduction

In this chapter, the design of an energy-efficient and low-cost wireless technology with RF frequency doubling reflectenna (FDR) sensors is presented for long-term environmental sensing. Fig. 2.1 shows the simplified FDR working principle. A low-loss Schottky diode is often employed for battery-less frequency multiplication because of its low barrier junction. When the receiver antenna receives an f_0 signal from the interrogator, it delivers the signal to the input of the diode. Since the input impedance of the diode is conjugately matched with the receiver antenna's impedance at f_0 frequency, maximum power is delivered to the diode. Then, the diode creates the harmonics of the signal and introduces conversion gain (CG) while converting the f_0 signal to $2f_0$. Since the output impedance of the diode at the second harmonic ($2f_0$) is conjugately matched to the input of the transmitter antenna, the maximum power at $2f_0$ frequency is collected and transmitted back to the interrogator. During this process, the receiver (RX) and transmitter (TX) antenna impedances should look short-circuited at the $2f_0$ and f_0 frequencies, respectively.

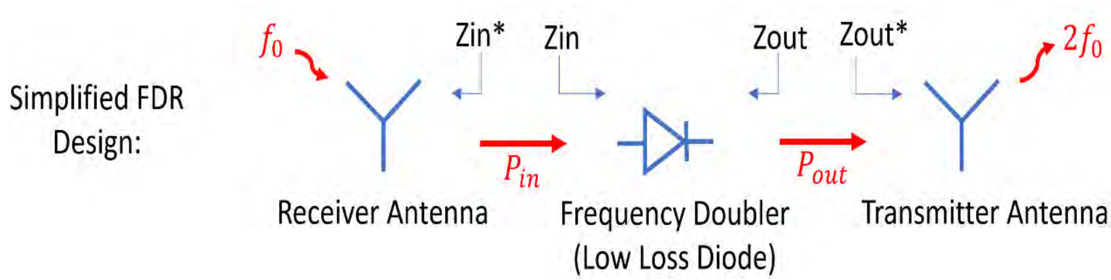

Fig. 2.1. Simplified FDR working principle.

Three types of losses must be considered while designing the FDR:

a) Conversion gain (the negative of conversion loss (CL)) that is described as the signal level difference between the input and output of the diode. CG is the most significant loss parameter. It comprises the losses due to the frequency conversion inside the diode and input and output impedance mismatches between the TX/RX antennas and the diode.

$$\text{Conversion Gain} = P_{out,2f_0} - P_{in,f_0} \tag{1.1}$$

b) dielectric/conductor losses due to the materials used in FDR,

c) dissipation and insertion loss due to lumped components if these are used in the matching network.

The diode is a nonlinear component, and its input and output impedances depend on operating frequency, input power level, temperature, and the diode's electrical characteristics. Therefore, the CG created by the diode also varies based on these parameters.

The interrogation range (or readout distance) is the maximum distance for the interrogator to be able to receive the signal from FDR. Depending on the application, the interrogation range requirement changes which plays a key role in the FDR design. The higher the interrogation distance, the lower the amount of power received from the FDR. At a certain distance, the returned signal may not be distinguishable due to being close to the noise floor of the utilized interrogator. There are a couple of ways to extend the reading distance, which are given in Fig. 2.2. a) The design frequency can be reduced to lower the path loss. However, this results in a larger FDR size which may

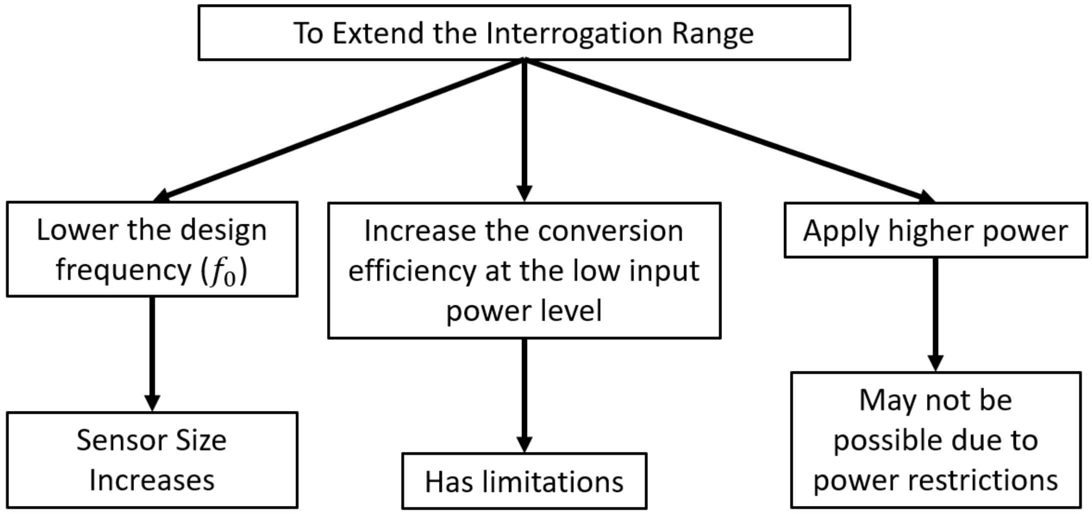

Figure 2.2. Ways to extend interrogation range and their disadvantages.

not be preferred if there is a size constraint. b) Input and output impedance matching networks can be designed to get as high as possible CG at the lower input power levels. But the improvement of CG is limited since the maximum achievable CG is -6 dB for a resistive diode. c) Higher power can be applied from the interrogator. However, there is an upper limit for the applied power, and high-power components used in the measurement setup (filters, circulators, amplifiers) are increasingly expensive and bulky as the power level increases. Since a drone-based interrogator is considered herein, the excessive weight would cause a concern. Therefore, based on the interrogation range requirement, these parameters should be considered as part of the FDR design process.

Our choice of $f_0 \cong 1.2$ GHz for the FDR design presented herein is based on tracking railroad ballast moisture application. According to the series of controlled laboratory experiments in which ballast is fouled with various moisture content, we found that under severe fouling, we were able to interrogate using EIRP of 16 dBm an

FDR embedded up to 40 cm below the surface at 1.2 GHz frequency range. Our data indicate that the return signal attenuates at a rate of at least 1 dB/m/% moisture; thus, the interrogator can readily detect typical "fouled" conditions. Since 2.4 GHz ($2f_0$) is in the ISM band and used for other commercial applications, the operation frequency (f_0) and ($2f_0$) are selected at 1.19 GHz and 2.38 GHz to avoid interferences.

As mentioned before, the brand/model choice of a Schottky diode is an important criterion in the FDR design since it has a strong relationship with the CG. Fig. 2.3. shows the equivalent circuit, and Table 2.1 defines the SPICE model parameters of a Schottky diode. Each diode model sold on the market has different values for the SPICE model parameters. According to [33], C_{j0}, R_j, M, and the ambient temperature parameters are inversely proportional to the CG, while I_s, V_j, and R_s are directly proportional. Therefore, these parameters of the diodes should be analyzed at the specific input power level of interest to find the optimum diode model to use in the design.

According to [14], the Keysight HSCH-9161 diode provides high CG (nearly -16 dB) at a low input power level (-30 dBm). Therefore, an FDR designed with this

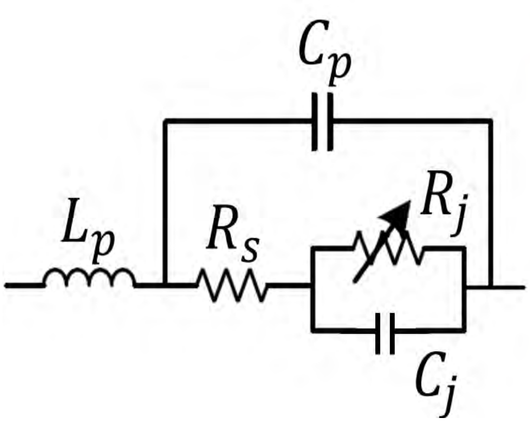

Parameter	Description
C_j	Junction Capacitance
R_j	Junction Resistance
R_s	Ohmic Resistance
L_p	Parasitic Inductor
C_p	Parasitic Capacitor

Figure 2.3. Equivalent circuit of a Schottky Diode and the description of its parameters.

Table 2.1 SPICE model parameters of a Schottky diode.

Parameter	Description
I_s	Saturation Current
C_{j0}	Zero-bias Junction Capacitance
V_j	Junction Potential
R_s	Ohmic Resistance
M	Grading Coefficient
N	Emission Coefficient
XTI	Saturation-Current Temperature Exponent
E_G	Energy Gap
B_V	Reverse Break Down Voltage
I_{BV}	Current at Reverse Break Down Voltage

diode is explained in the first part of this chapter. The proposed design adds the benefit of having a higher interrogator range due to the operating frequency, lower packaging size (0.20 λ_0 vs. 0.24 λ_0 in [14]), and being mechanically tunable. In the following part of the chapter, an FDR design with Skyworks SMS7630-079LF is presented. The proposed FDR provides a 5 dB improvement in CG at the same input power of interest (-30 dBm) as well as smaller in size compared with the FDR design in [33] that employs the same diode. The design parameters and the test results are given. The chapter ends with the conclusions.

2.2. Input and Output Impedance Simulations of Keysight HSCH-9161 Diode

This section describes the design process of an FDR with an HSCH-9161 diode. Keysight ADS v2021 is used to simulate the input and output impedances of the diode at a specific input power level and frequency. Fig. 2.4 shows the diode model and its

SPICE model parameters used in the simulations. The parameters are obtained from [34]. D1 and D2 model the diode for the forward and reverse bias conditions, respectively. 11 fF shunt capacitance and 0.3 nH series inductance represent the parasitics due to packaging.

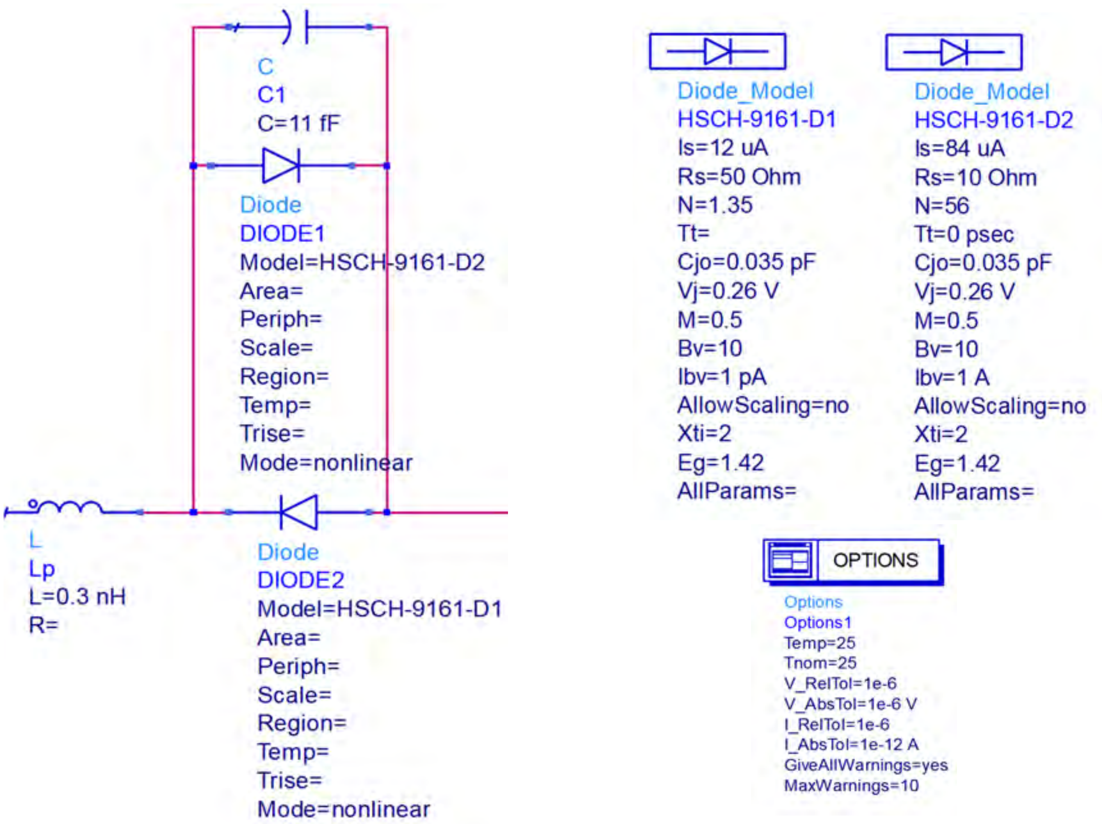

Figure 2.4 Equivalent circuit of the HSCH-9161 Schottky Diode.

Fig. 2.5. shows the data files used in the simulations representing 1st to 4th-order bandpass filters. The 5th and higher-order harmonics don't have a significant impact on the CG and are therefore excluded from the model [34]. The filters are employed at the

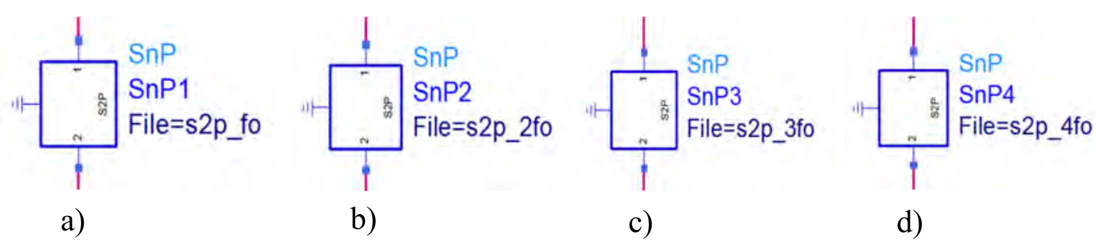

Figure 2.5 Data files used as a) f_0, b) $2f_0$, c) $3f_0$, and d) $4f_0$ bandpass filters.

input and output of the diode to make sure all the signals are blocked and only the desired harmonic of the signal pass. Appendix A gives an example of a data file that represents the f_0 bandpass filter.

Fig. 2.6 shows an impedance component that represents the impedance of the FDR RX/TX antennas at the specific harmonic frequency. These parameters will be obtained after designing the antennas in Ansys HFSS v22.

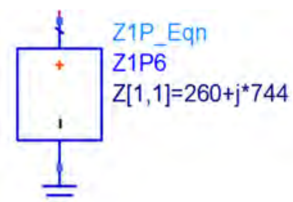

Figure 2.6 Impedance of the RX/TX antennas at the specific harmonic frequency.

The RF power source in Fig. 2.7 represents the signal received from the interrogator at f_0 frequency with the level of P_in. Since the FDR in this work is intended to be interrogated at a low input power level, -30 dBm is used as the nominal design point for P_in.

Figure 2.7 RF power source.

The complete schematic is given in Fig. 2.8 to find the input impedance of the diode that provides the highest CG at 1.19 GHz (f_0) and -30 dBm input power level when conjugately matched. It is important to note that all impedance parameters are defined as "0" except the impedances at f_0 on the RX side and $2f_0$ on the TX side. This is an ideal case for the FDR since the harmonics are desired to look shorted to get

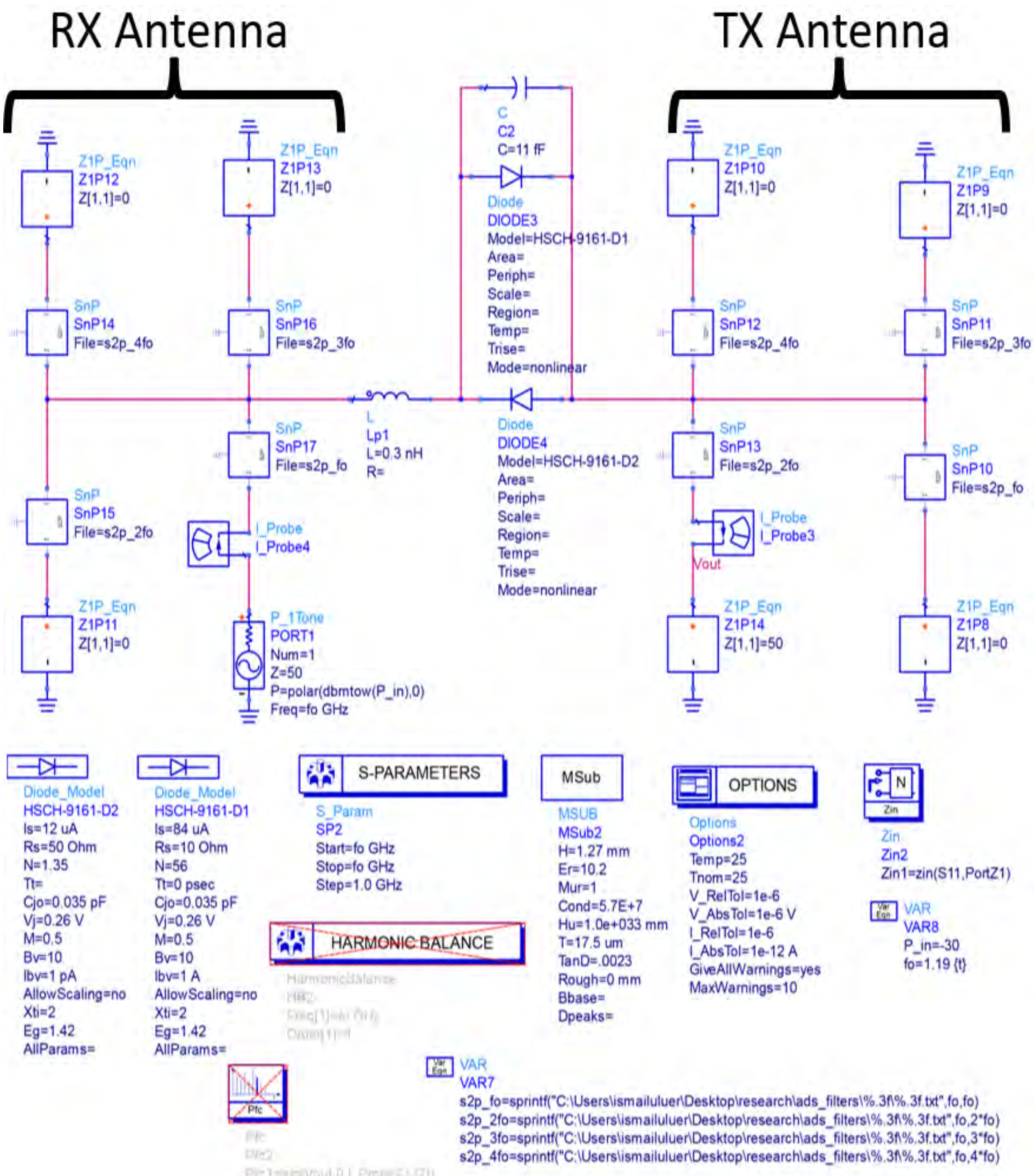

Figure 2.8 Complete schematic to find the input impedance of the diode at f_0 and -30 dBm input power level.

maximum CG. From this schematic, it is determined that the input impedance of the diode at f_0 is 777-j*1150 Ohms.

By doing the same procedure, the output impedance of the diode is found. Again, all impedance parameters are defined as “0” except the impedances at f_0 on the

RX side (777+j*1150 ohms) and $2f_0$ on the TX side (50 ohms), as seen in Fig. 2.9. The impedance is found as 260-j*744 Ohms.

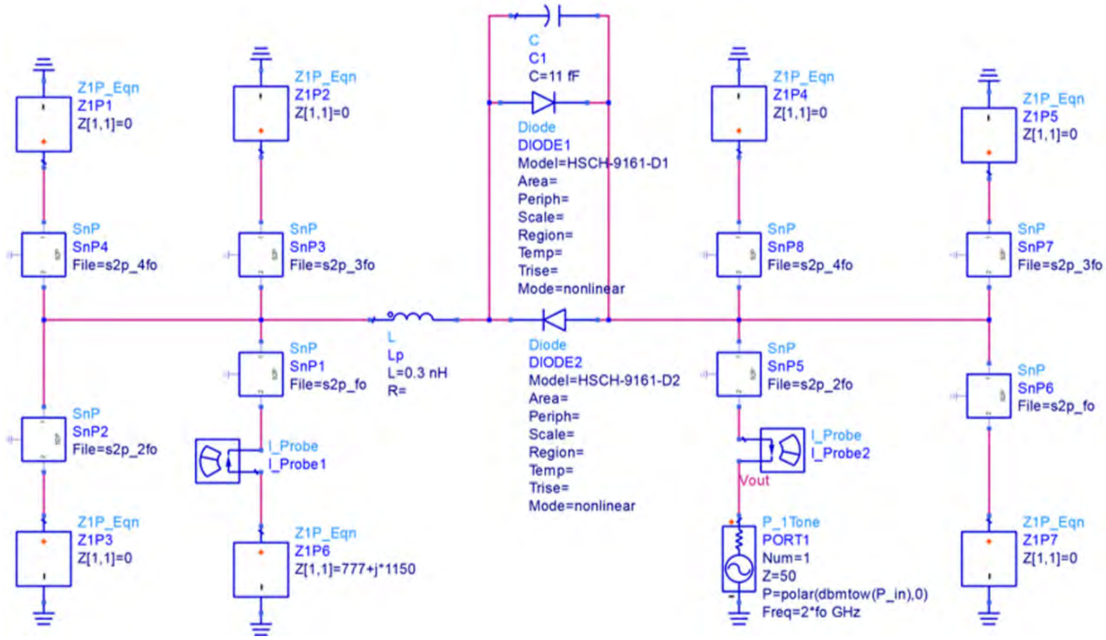

Figure 2.9 Complete schematic to find the output impedance of the diode at $2f_0$.

After defining the input and output impedances, the harmonic balance simulator is used to simulate the CG. The CG can be calculated from the equation (2):

$$\text{Conversion Gain} = (10*\log(Pfc1) + 30) - P\_in \qquad (1.2)$$

where Pfc1, calculated by the data component in the schematic, is the second harmonic signal power level at the output in Watts, which is then converted to dBm. Fig. 2.10 shows the simulated CG vs. input power level. The -16 dB CG at -30 dBm input power is the lowest possible value achieved with this diode at this frequency and input power level. As mentioned above, this is the ideal case, and the actual CG will be lower since it is very hard to obtain the exact impedances found here for the fabricated RX & TX antennas.

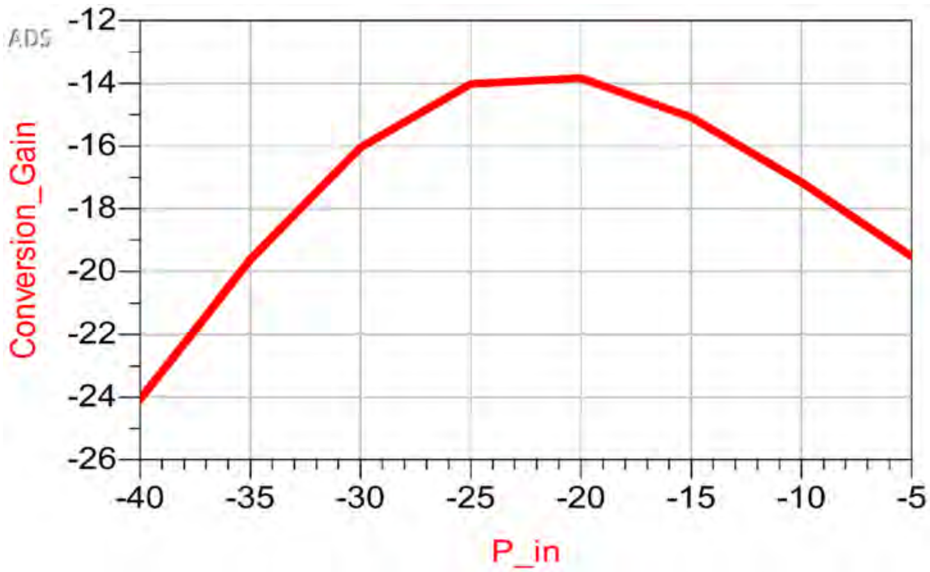

Figure 2.10 Simulated CG vs. input power level.

2.3. FDR Design with Keysight HSCH-9161 Diode (First Iteration)

2.3.1. Design and Methodology

The receiver and transmitter antennas of the FDR are expected to be small in size and omnidirectional, provide high radiation efficiency and have narrow bandwidth to be used in environmental sensing. At the same time, their input impedances should conjugately match the input and output impedances of the diode to obtain the best conversion efficiency. The miniaturized dipole antennas have shown promise in meeting these requirements [14,35]. As explained in [36], if the maximum dimension of the antenna is reduced, the radiation efficiency can still be maintained by using the available volume effectively. Therefore, the 3D structure of the miniaturized dipole elements enables us to realize that.

The design process of the FDR is given in a diagram in Fig. 2.11. It starts with finding the input and output impedances of the diode, as explained in Section 2.2, and continues with designing the RX and TX antennas individually that have input impedances nearly conjugately matched to them. The simulated receiver and transmitter antennas operating at 1.19 GHz (f_0) and 2.38 GHz ($2f_0$) and their design parameters are given in Fig. 2.12 and 2.13, respectively. The antennas are designed and optimized in Ansys Electronics Desktop 2022 R2. The antennas consist of a half-wave dipole that has the arms terminated with meandered sections and fed by a balun and meandered matching line. The use of meandered line sections and the high permittivity substrate material, 50-mil-thick Rogers 3010 (ε_r=10.2, tanδ= 0.0035), helps to reduce the antenna size. On the other hand, the meandered lines make the antenna impedance more inductive, and the high permittivity material causes higher dielectric loss. However, we benefit from this inductance while designing the input impedance matching network. It can be also recognized that the meandered section on one arm is

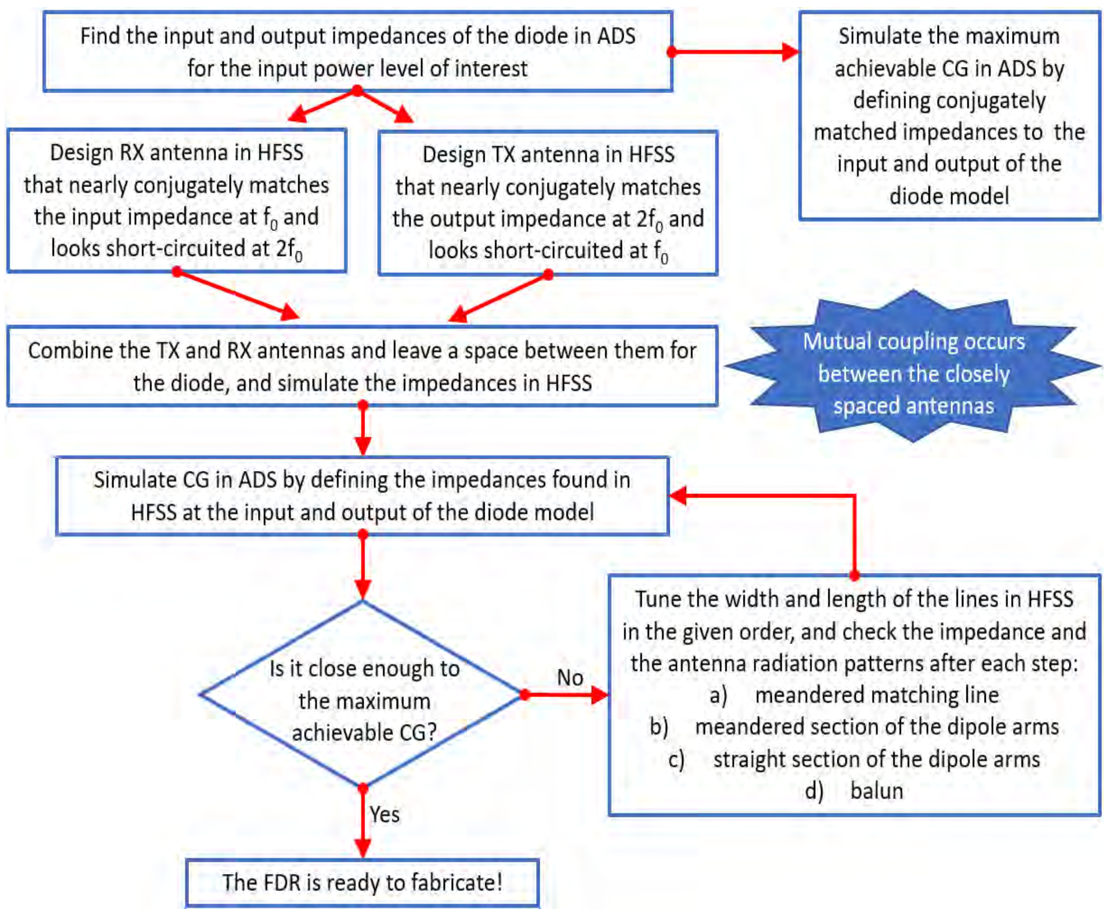

Figure 2.11 FDR design process diagram.

looking upward, and the other one is downward. This arrangement helps to reduce the radiated field cancellations while keeping the current distribution on the arms balanced [14].

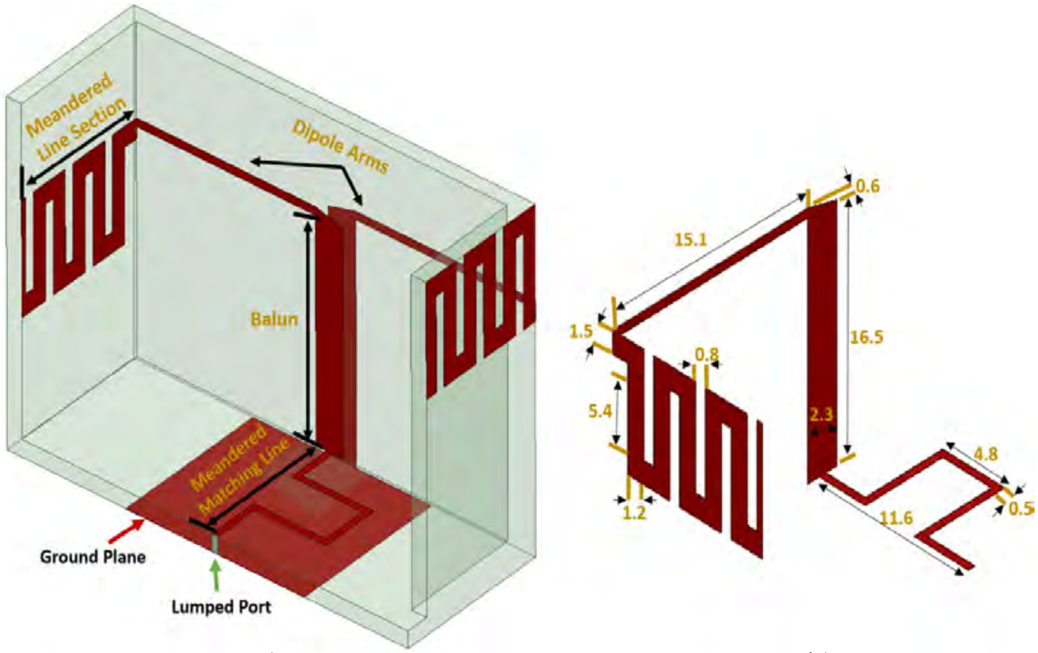

a) b)

Figure 2.12 Simulated a) receiver antenna and b) its dimensions in mm.

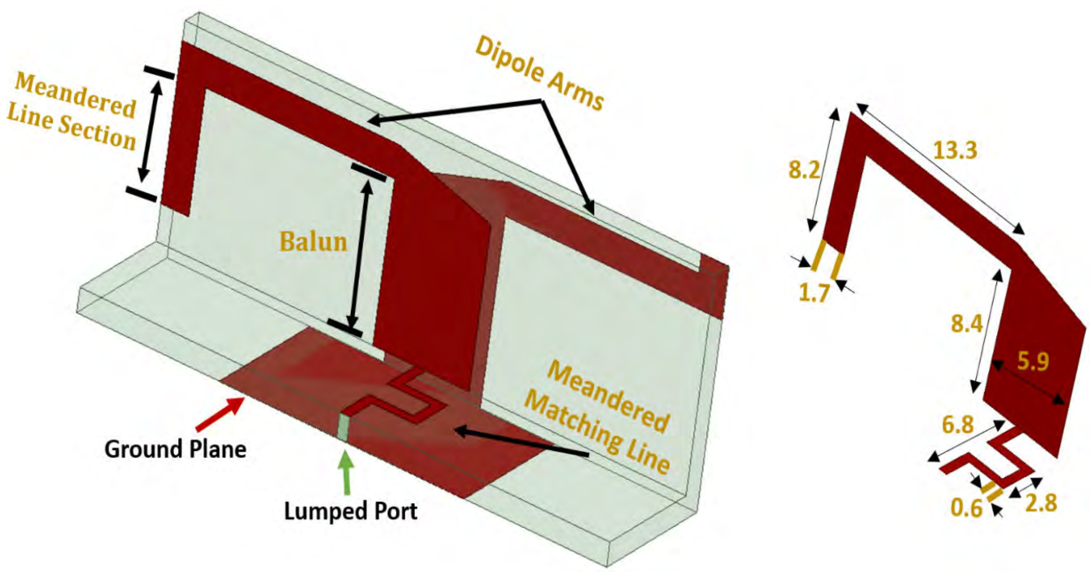

a) b)

Figure 2.13 Simulated a) transmitter antenna and b) its dimensions in mm.

A quarter-wave long balun is employed to create a high impedance between the dipole arms and the ground so that unbalanced currents coming from the ground are choked, and balanced current distribution is seen on the dipole arms. To avoid creating fringing fields and losing power, the balun width should be much larger than the separation between the two parallel balun conductors [37].

The meandered impedance matching lines are added to conjugately match the input and output impedances of the diode found in the previous section. The corresponding input impedances, which are (777+j*1150) for the input and (260+j*744) for the output, are very inductive. Therefore, SMD inductors can be added to the matching network. But, to reduce the number of components and avoid the loss caused by these components, the meandered lines are preferred. These lines also help to reduce the matching line length. As mentioned in the previous section, it is not possible to perfectly short-circuit the harmonics of the signal in the actual design. Therefore, after designing the antenna and importing all the simulated impedance parameters into the ADS, the input and output impedance parameters should be optimized again to obtain the best conversion efficiency. With the optimization, the input impedances of the receive and transmit antennas are found (850+j1000 Ω) and (300+j600 Ω), respectively.

The lumped port used in HFSS simulations excites the antennas since it can replicate the realistic scenario where a small source (diode) is internally located [38]. Fig. 2.14 shows the lumped port impedance that represents the input impedance of the diode for the receiver antenna. Maximum Delta S is selected 0.01, and the minimum converged passes are made 2 for higher simulation accuracy[1].

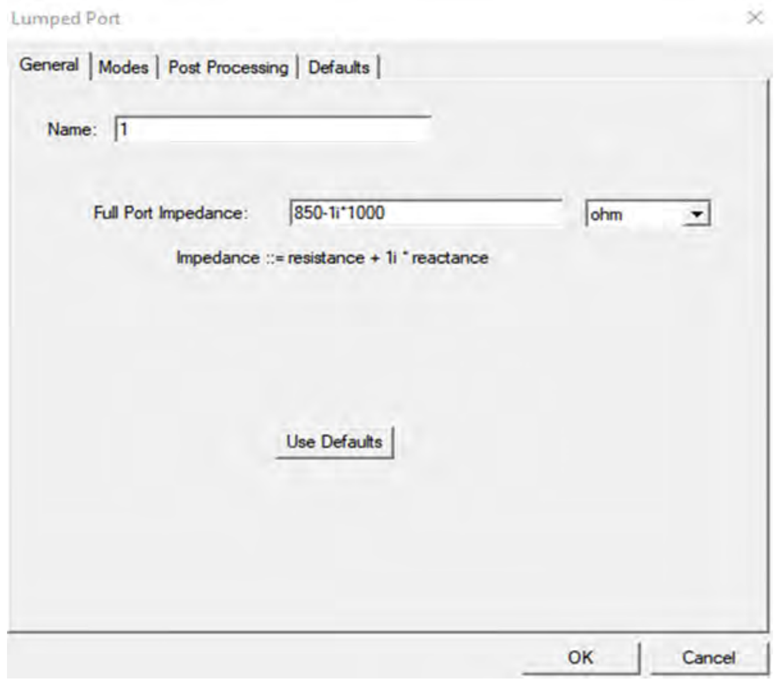

Figure 2.14 Defining the lumped port impedance.

The final receiver and transmitter antenna simulations are made within the complete FDR structure, as shown in Fig. 2.15, for higher accuracy. Because two antennas have close proximity in the FDR, the coupling effect is taken into account by simulating them together. This resulted in a resonant frequency shift in the antenna response and tilted and distorted the radiation pattern. To correct these issues, the width and length of all the lines can be tuned. Since the small dipole antenna impedance is transformed to a high impedance with the quarter-wave balun, a small change in the dipole arms has a big impact on the antenna input impedance. Therefore, it is better to

---

[1] HFSS has an adaptive meshing that helps refine the mesh step-by-step at high-field concentration locations. Each meshing refinement step is called an adaptive pass, and its maximum limit is defined by the user from the maximum number of passes setting. The scattering parameters calculated at each pass are compared with the ones found in the previous pass. If their difference is less than the specified maximum delta s, the adaptive analysis ends. Smaller delta S provides higher accuracy but increases the computational time and complexity. [39]

start the tuning process from the matching line that can slightly tune the impedance and has a small impact on the radiation pattern. If this does not help, then the dipole arms and the balun can be optimized, respectively.

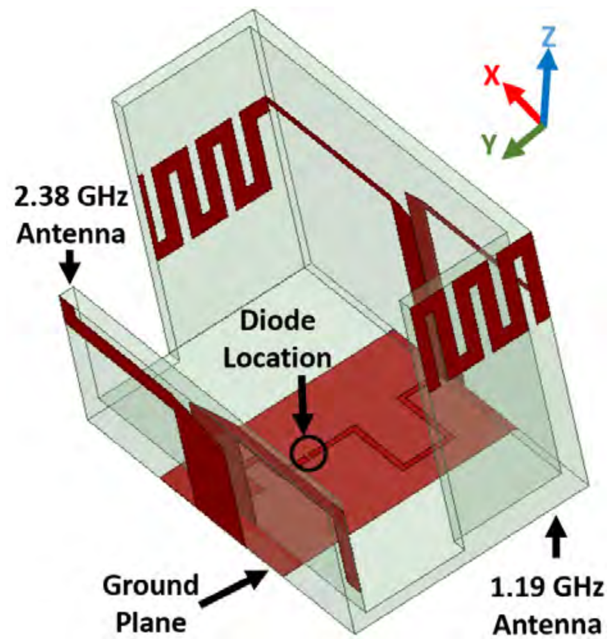

Figure 2.15 Simulated complete FDR.

Fig. 2.16 and 2.17 show the input impedances of the receiver and transmitter antennas. The receiver antenna provides the necessary input impedance at the f_0 frequency while it looks close to the short-circuited at the $2f_0$ frequency. Similarly, the transmitter antenna looks short-circuited at f_0 frequency while it matches very well to the output impedance of the diode at $2f_0$ frequency.

Fig. 2.18 and 2.19 illustrate the simulated E and H plane and 3D radiation patterns. The receive and transmit antennas have maximum gains of 0.9 and 2.1 dBi, respectively. The transmit antenna E-plane pattern is slightly distorted due to its close proximity to the receive antenna and ground plane effects. This also causes different peak gains perpendicular to the non-meandered dipole arms. For instance, the peak gains of the transmitter antenna at $\theta = 0^o$ and $\theta = 180^o$ are 1.2 dBi and 2.1 dBi, respectively. Making one of the dipole arms slightly shorter than the other helped to bend the E-plane pattern and make the maximum radiation on the broadside to the dipole arms. The H-plane patterns are omni-directional.

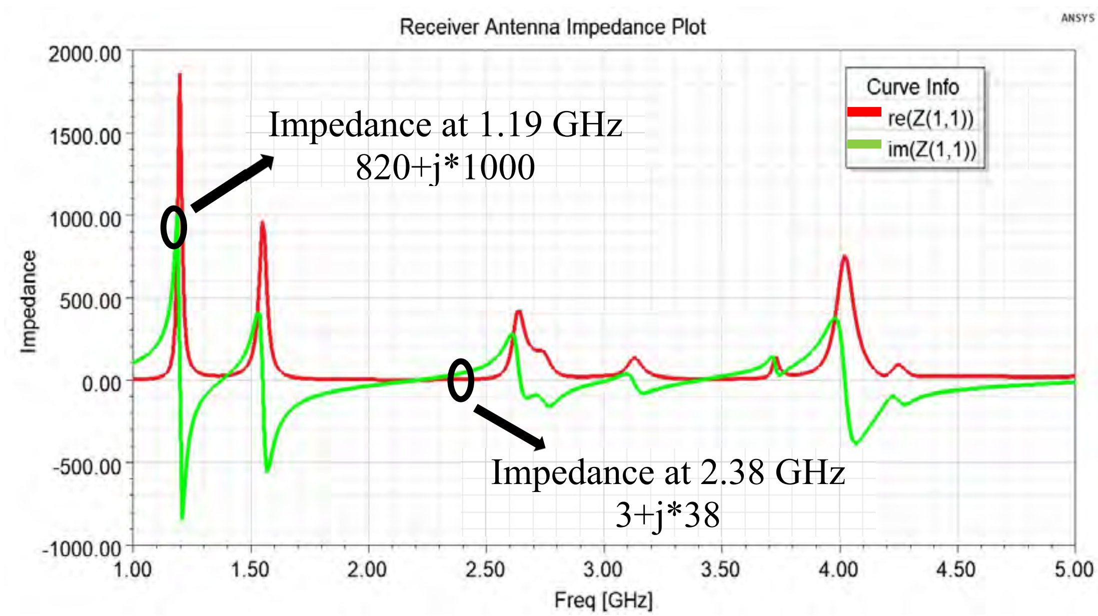

Figure 2.16 Simulated receiver antenna impedance.

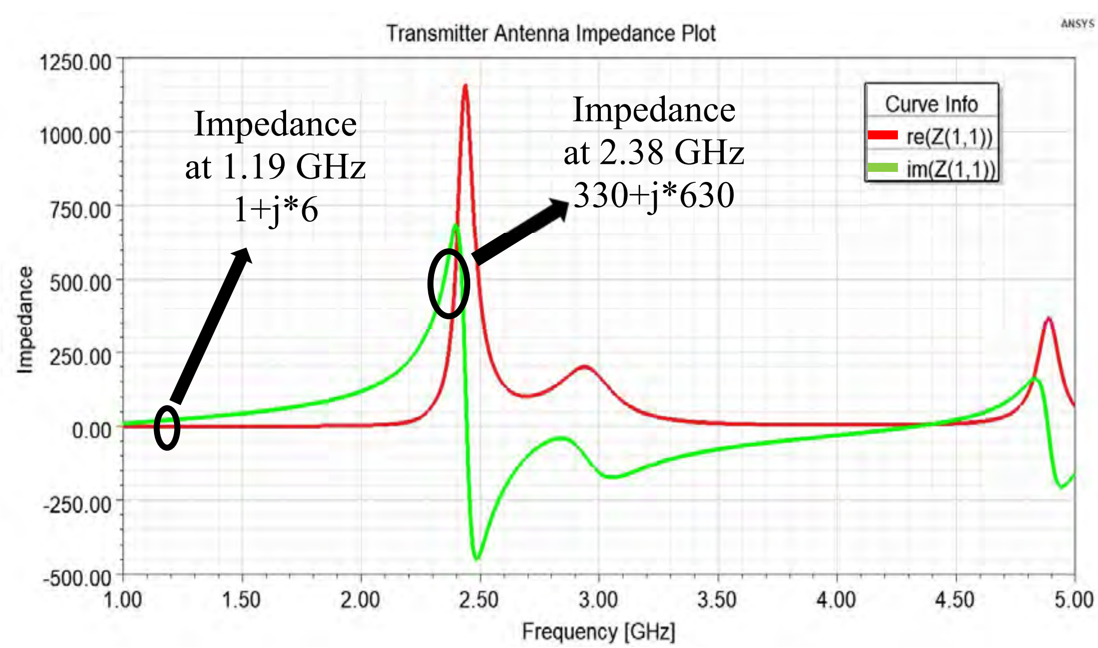

Figure 2.17 Simulated transmitter antenna impedance.

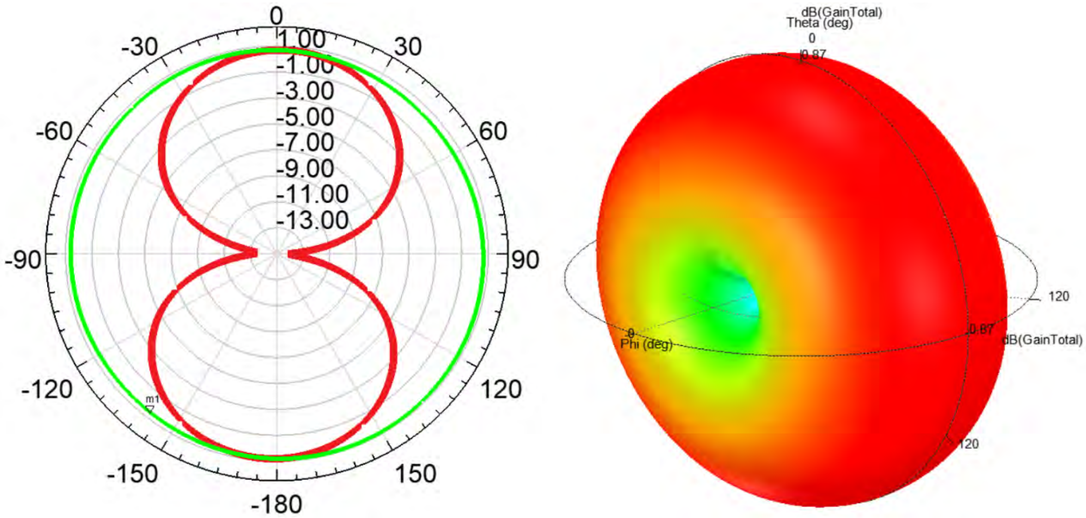

Figure 2.18 Simulated receiver antenna radiation pattern.

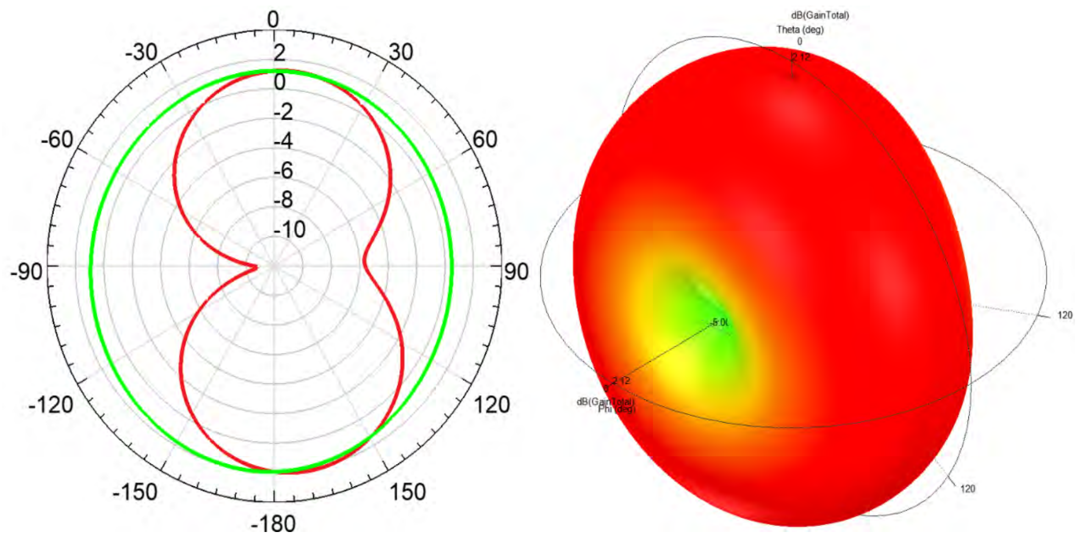

Figure 2.19 Simulated transmitted antenna radiation pattern.

2.3.2. Measurement Setup and Results

Fig. 2.20 shows the fabricated FDR. The fabrication of 2D printed circuit pieces was made with the LPKF S103 milling machine, and the 3D shape was created by combining them with super glue. Small copper tape patches were attached to the joint locations, and all the conductors were combined with soldering.

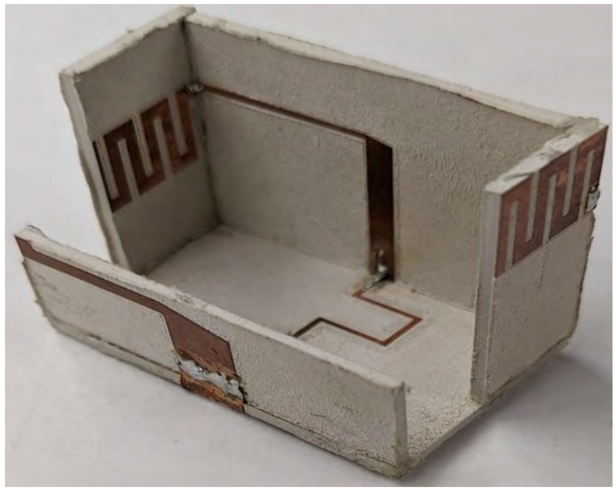

Figure 2.20 Fabricated FDR.

The measurements are made in an anechoic chamber at Portland State University, and the test setup is given in a diagram in Fig. 2.21. The f_0 signal created by the signal generator passes through the bandpass filters to block all the harmonics of it, if any. It is then amplified and passed through the filters again for the same reason. Commercial Yagi antennas, which were separated 1m from each other to lower mutual coupling and located 3m away from the FDR, were used to transmit and receive signals to the FDR. The FDR was measured from the ground plane where RX and TX antennas had the maximum gain. The $2f_0$ signal received from the FDR was again filtered and amplified. The signal level was monitored by a spectrum analyzer.

To calculate the CG of the FDR, all the losses and gains that happened in the test setup were considered. Losses are:

- Insertion loss of bandpass filters,
- Cable losses,
- Path loss, which was calculated by using the Friis transmission equation,

and gains are:

- Amplifier gains,

- TX/RX antenna gains of the commercial Yagi antennas,
- TX/RX antenna gains of the FDR.

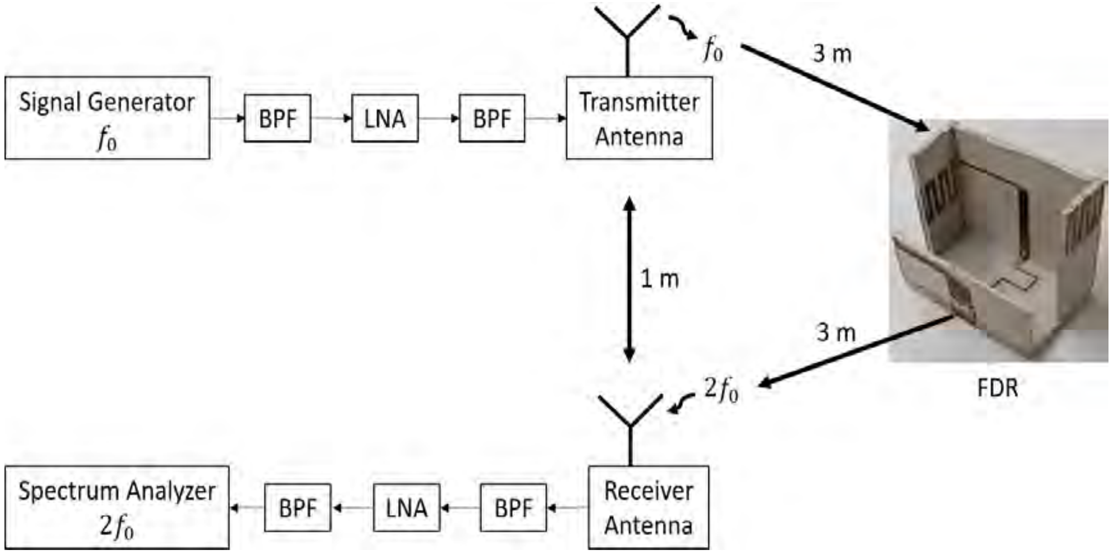

Figure 2.21 Measurement setup.

The measured and simulated CG are compared in Fig. 2.22. It is important to note that the transceiver graph adds the RX and TX antenna gains of the FDR to the CG calculation while the doubler graph does not. A small resonant frequency shift happened, and the maximum CG was obtained at 1.185 GHz. The reason could be because of either error in fabrication or assumed material dielectric properties. According to [40], the dielectric constant of Rogers 3010 has an error factor of +/- 0.3. So, if it is more than the assumed value of 10.2, then the resonant frequency would shift to a lower frequency since the wavelength gets smaller. The simulated and measured CG data show a close agreement and are in the range of -15 dB at the low input power levels of -30 to -20 dBm. The CG of the full transceiver becomes around -13 dB at low power levels. At higher input power levels, the measured CG response increases rather than being in compression, as observed in the simulated data; this discrepancy is attributed to deficiencies in the Schottky diode model and is explained in detail in the next section. A narrowband 3-dB CG bandwidth was measured (1.7%), which is an advantage for the applications it will be used for.

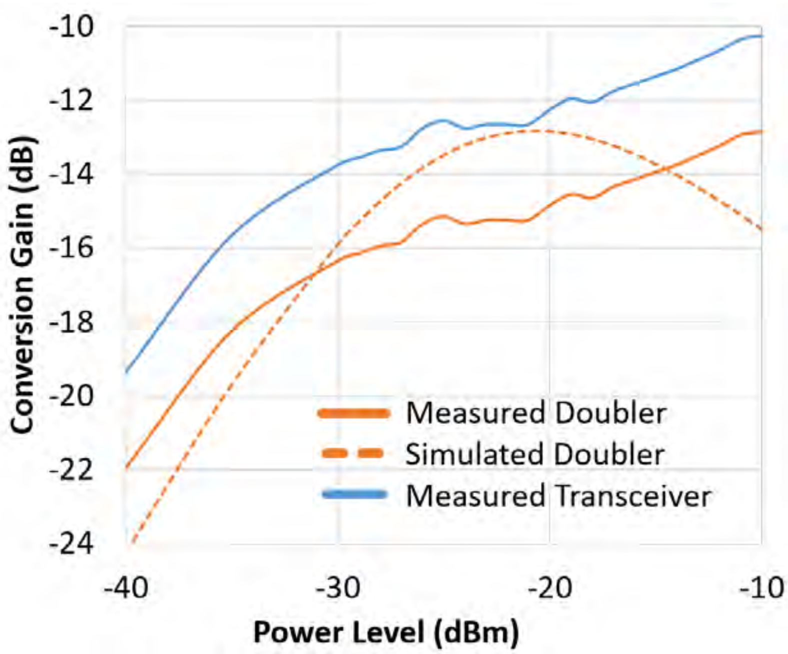

Figure 2.22 Measured vs. simulated CG vs. input power level.

2.3.3. Correction in the Simulated Model

When an f_0 signal hits the multiplier, it creates the harmonics of this signal and a DC component. If there is no DC return path at the output of the multiplier, then this condition can bias the diode, affect its impedance, and impact/worsen the conversion efficiency. In this case, the efficiency can be improved by creating a DC ground return path [41].

Further studies have shown that the main reason for the discrepancy between the measured and simulated CG presented in the previous section is related to the unintentionally defined DC path in the schematic. The data files representing BPFs were unintentionally defined without parameters for the DC response, and the simulation defaulted to allowing DC to pass. In reality, however, the fabricated FDR does not have a DC path. Fig. 2.23 compares the measured CG with the simulated CG responses when the DC component is blocked and not blocked by the BPFs. The simulated data without the DC path shows the same trend as the measurements. Although there is still a small discrepancy which is attributed to the deficiencies in the Schottky diode model, the simulated model gives a very good approximation and can be used in future designs. Another important observation from Fig. 2.23 is that the DC path provides higher conversion efficiency at the lower input power levels. Vias could be employed at the input and output of the multiplier for this purpose.

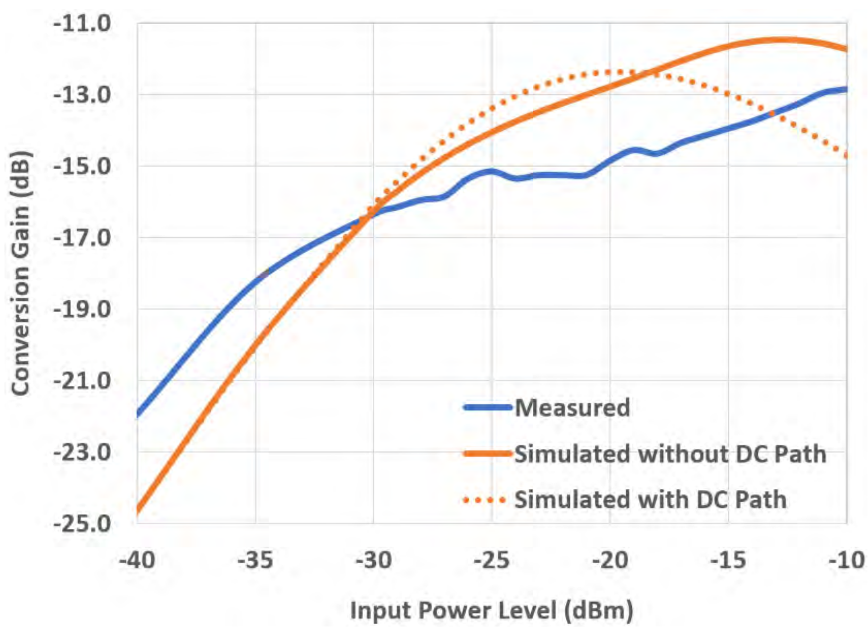

Figure 2.23 Measured vs. simulated CG vs. input power level with and without DC path.

2.4. FDR Design with Keysight HSCH-9161 Diode (Second Iteration)

2.4.1. Design and Methodology

The need of creating a DC path between the input and output of the FDR design is achieved by adding quarter-wave short-circuited stubs attached to the impedance-matching lines, as seen in Fig. 2.24. The stubs look open-circuited at f_0 for the receiver antenna and at $2f_0$ for the transmitter antenna to reduce the impact on their impedances.

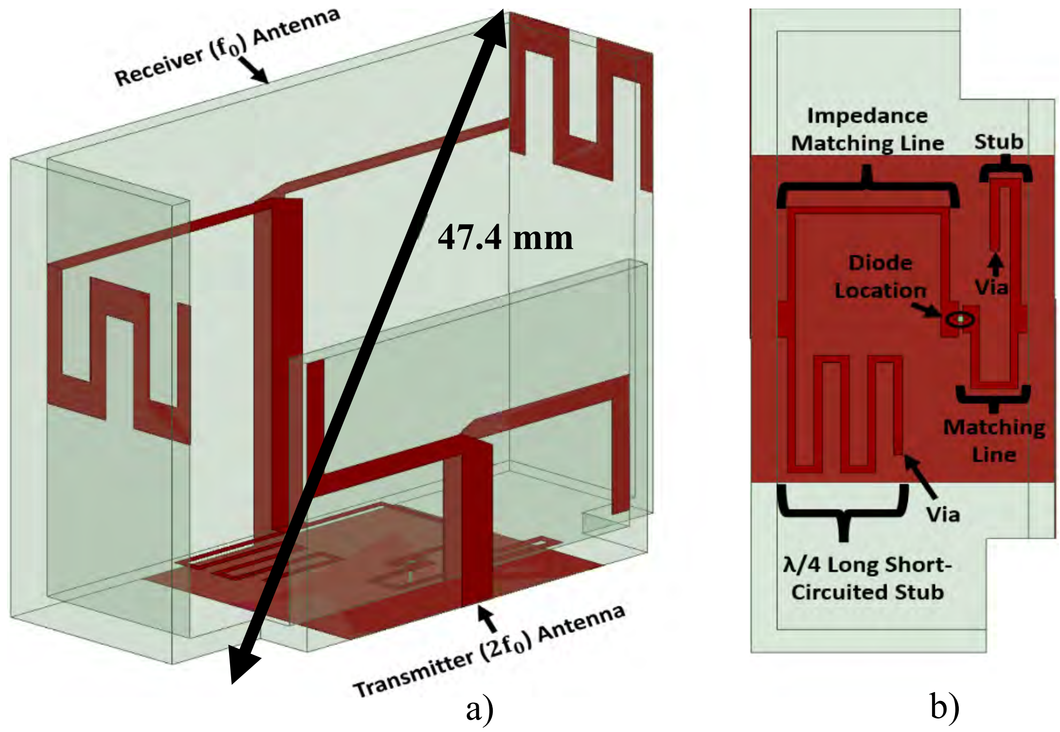

Figure 2.24 a) Isometric view b) top view of the second FDR iteration.

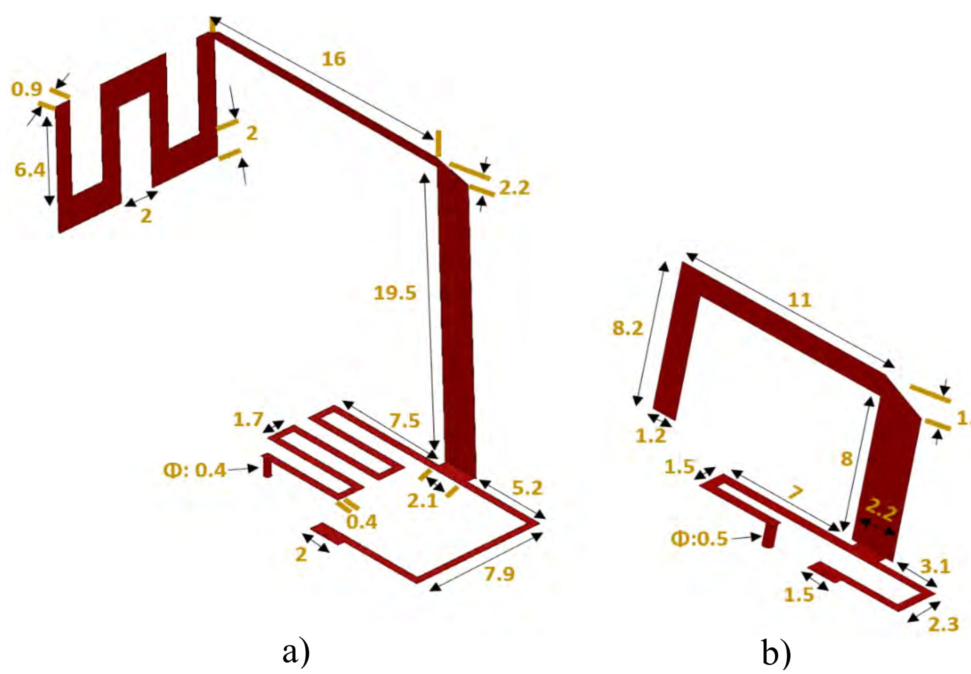

Figure 2.25 a) Receiver and b) transmitter antennas dimensions in mm.

However, their close proximity with the other lines affected the input impedances of the antennas. Thus, the lines widths and lengths are optimized again, and their parameters are shown in Fig. 2.25. The meandered design helps to keep the overall size of the FDR the same. The diagonal length of it is 47.4 mm, which is around 0.19λ at f_0.

The radiation pattern of the receive and transmit antennas, shown in Fig. 2.26, have peak gains of 0.8 and 2.35 dBi. The antennas' E-plane patterns are slightly distorted due to their close proximity with the receive antenna and ground plane effects. An omnidirectional pattern is seen in H-plane.

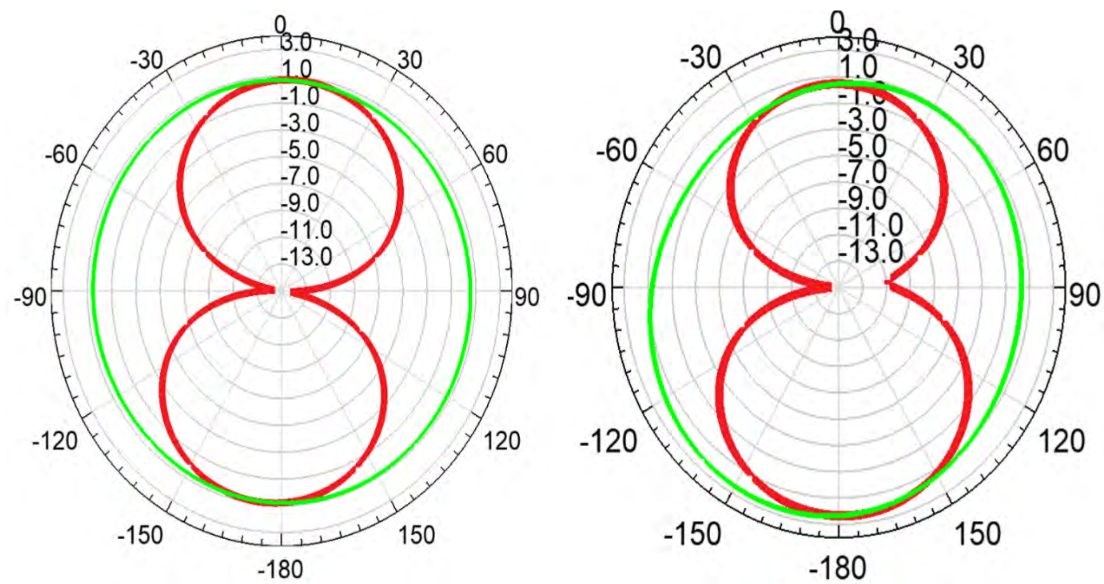

a) b)

Figure 2.26 a) Receiver and b) transmitter antennas radiation patterns.

2.4.2. Measurement Results

The conversion efficiency of the second iteration of the FDR design is improved significantly at the low input power levels. As seen in Fig. 2.27, the maximum CG is achieved at -20 dBm input power level where it measured -12 dB, which is nearly 3 dB higher compared to the first iteration. Since the impedance matching deteriorates at high power levels, the conversion efficiency is reduced. Simulation results that are in very good agreement with the measurements verified the accuracy of the simulation model.

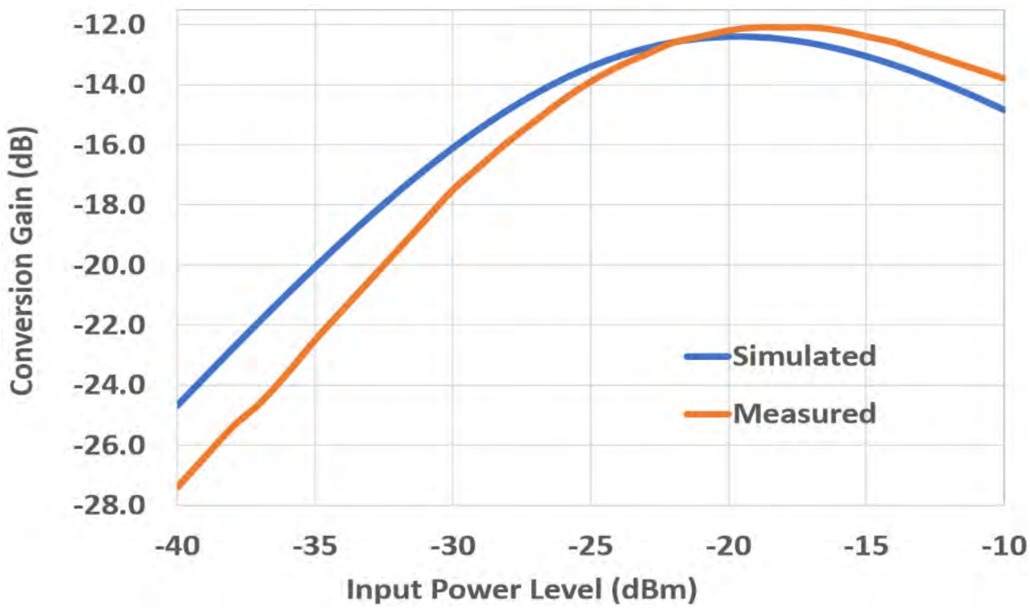

Figure 2.27 Comparison of the simulated vs. measured conversion gain.

2.5. FDR Design with Skyworks SMS7630-079LF Diode

2.5.1. Design and Methodology

Skyworks SMS7630-079LF has many advantages compared with Keysight HSCH-9161 to be used in FDR design, which are:

- Higher conversion efficiency at input low power levels,
- Characterized in detail by Modelithics Inc. (temperature, substrate, frequency scalable model),
- Easier to assemble/solder in FDR (HSCH-9161 has beam-lead packaging),

- Highly durable for environmental conditions (whereas the HSCH-9161 is mechanically fragile),
- Much lower cost,
- Easier to find on the market (HSCH-9161 usually has a longer factory lead time)

The only disadvantage can be said that SMS7630 has a larger packaging size (1.2 mm long) than HSCH-9161 (0.25 mm long), which does not have a big impact on the overall FDR size. Therefore, the FDR is redesigned with the SMS7630.

To find out the input and output impedances of the diode, the SMS7630 diode model seen in Fig. 2.28, created by Modelithics Inc., is simulated in ADS. The simulation mode is selected as a full parasitic model, meaning that it takes all the parasitic and soldering pad effects and substrate parameters that are given in Fig. 2.28 as well [42]. As explained before, the optimum input and output impedances that provide the highest achievable CG are found after making a series of simulations between ADS and HFSS. When the receiver and transmitter antennas are conjugately matched to (70-1i*375) and (30-1i*180), the simulated CG at -30 dBm input power is obtained -13.5 dB, which is around 3 dB higher than HSCH-9161.

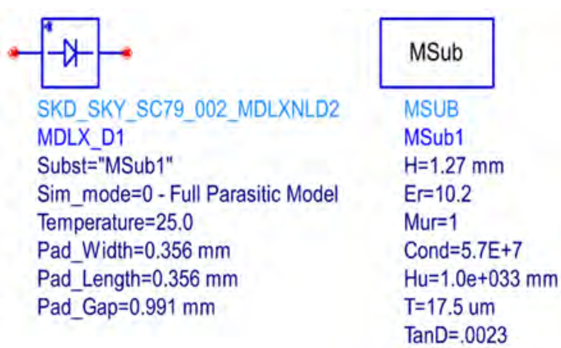

Figure 2.28 Modelithics SMS7630 diode model and the substrate material parameters used in the FDR.

Fig. 2.29 shows the simulated FDR. While holding the main antenna and feeding structures the same, the lines width and length of the previous FDR design for the HSCH-9161 diode are optimized for the input and output impedances SMS7630 diode. The DC path is again created through the vias located at the end of the quarter-wave short-circuited stubs. The receive and transmit antenna design parameters are given in Fig. 2.30 (a) and (b). The diagonal length of the FDR is 48.9 mm, which is around 0.2λ at f_0 frequency.

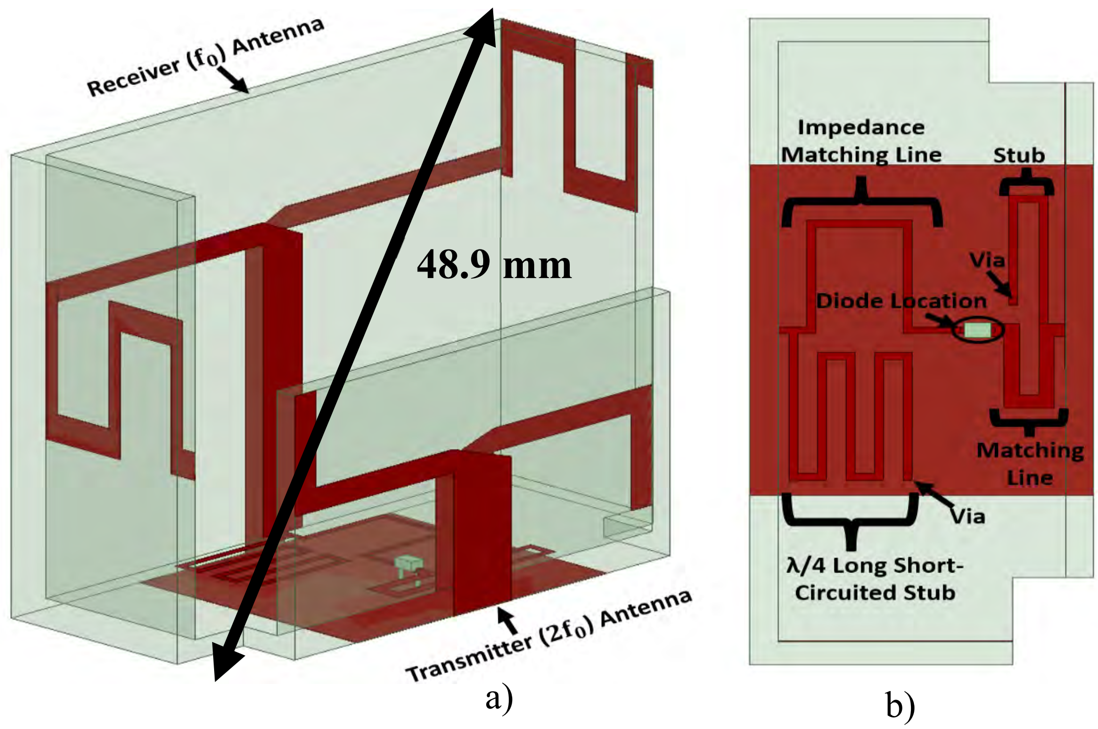

Figure 2.29 a) Isometric view b) top view of the FDR.

The radiation pattern of the receive and transmit antennas, shown in Fig. 2.31, have peak gains of 0.9 and 2.35 dBi with a simulated radiation efficiency of 73% and 85.5%, respectively. The antennas E-plane patterns are slightly distorted due to their close proximity with the receive antenna and ground plane effects. An omnidirectional pattern is seen in H-plane. The 3D radiation pattern of the receiver antenna from the front and side view in Fig. 2.32.

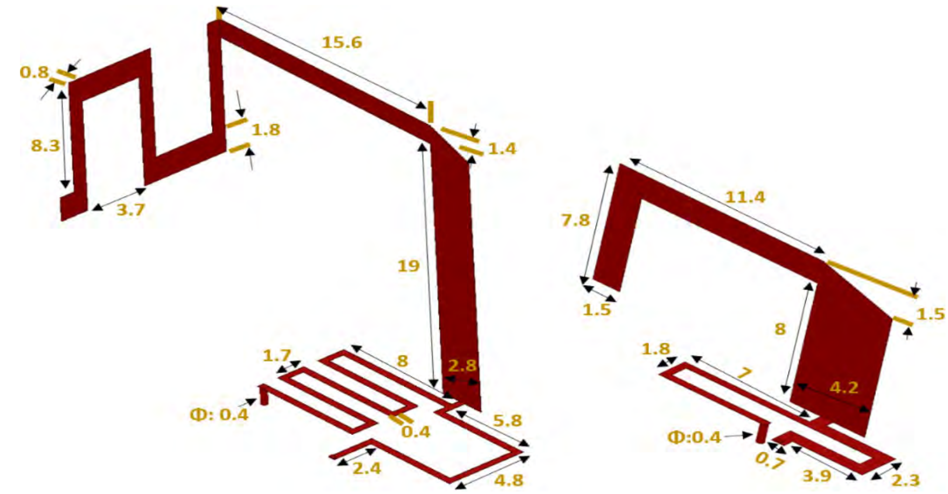

a) b)

Figure 2.30 a) Receiver and b) transmitter FDR dimensions in mm.

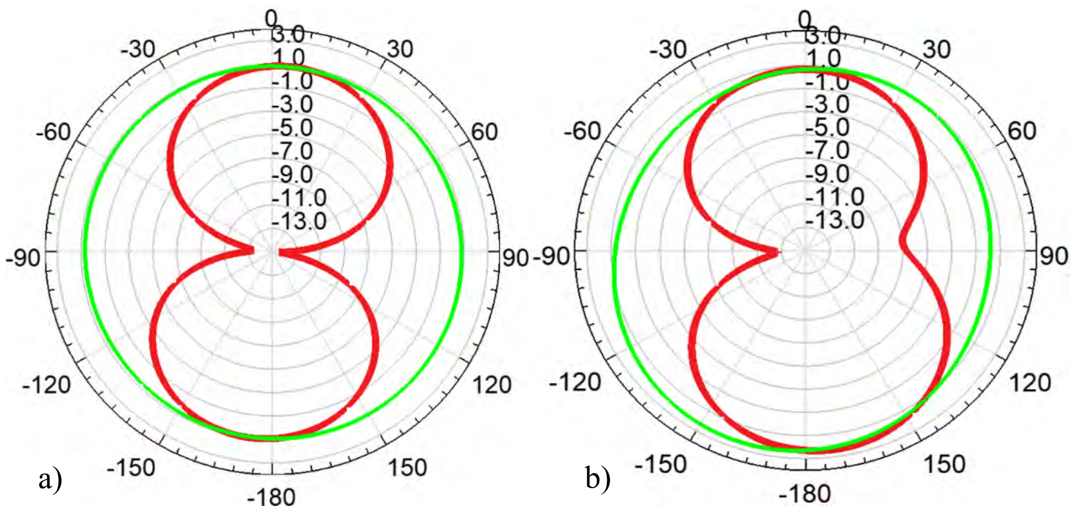

a) b)

Figure 2.31 a) Receiver and b) transmitter antennas radiation patterns.

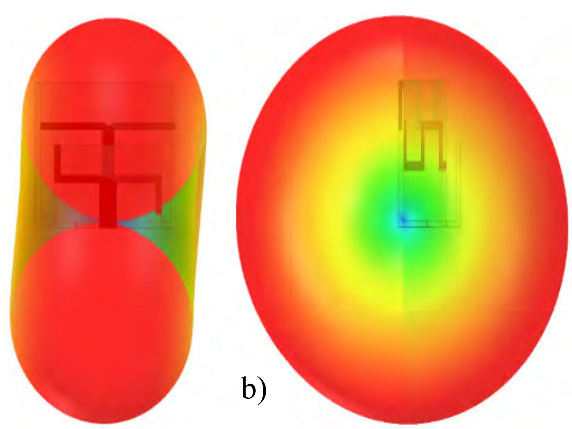

a) b)

Figure 2.32 3D radiation pattern of the receiver antenna a) front and b) side view.

2.5.2. Measurement Results

The fabricated FDR shown in Fig. 2.33 is tested, and the measured CG at f_0 of 1.182 GHz is compared with the simulations from ADS in Fig. 2.34. A small resonant frequency shift is attributed to fabrication errors. The transceiver CG is calculated by adding the receive and transmit antenna gains. The simulated and measured CG data show a close agreement and are in the range of -12 dB at -30 dBm and reach the peak level of -8 dB at -20 dBm. At higher input power levels, the CG is in compression, and similar exponential decay is seen rather than an increase seen in section 2.3. However, there is still a small discrepancy, which is related to the CG being very sensitive to the input and output impedance matching of the diode at f_0 and $2f_0$, respectively. Due to fabrication tolerances, the optimal impedance match frequency f_0 can shift at the input of the doubler, while the output impedance match may not have a corresponding shift. The 3-dB CG bandwidth of the FDR is approximately 1.5% at -30 dBm and 2.9% at -20 dBm. Fig. 2.35 shows the comparison between the simulated CG at 1.19 and at 1.182 GHz. At the design frequency of 1.19 GHz, the CG of the multiplier is expected

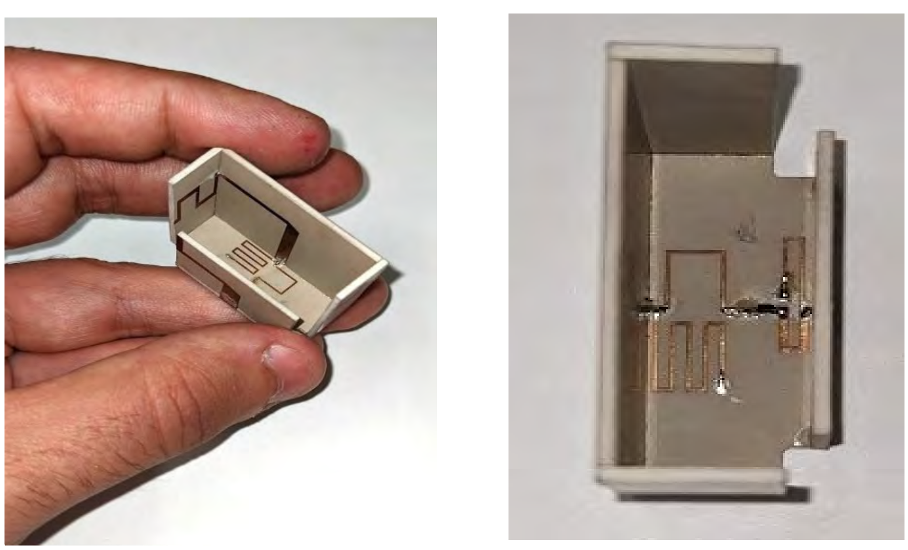

Figure 2.33 Fabricated FDR.

to be -13.5 at -30 dBm and -11 at -20 dBm; however, a lower CG is received due to the resonant frequency shift.

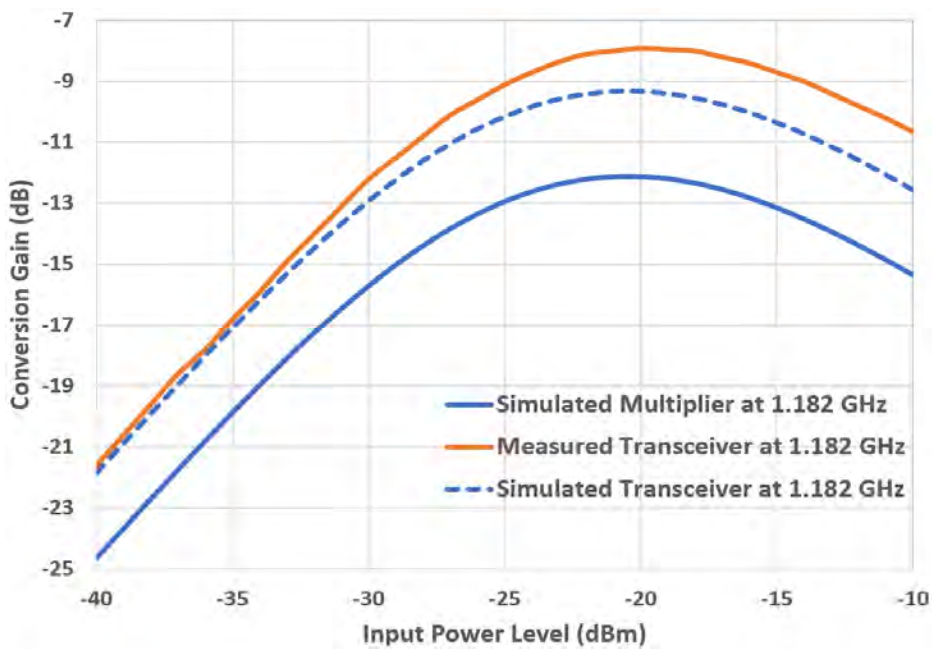

Figure 2.34 Comparison of simulated vs. measured CG at 1.182 GHz.

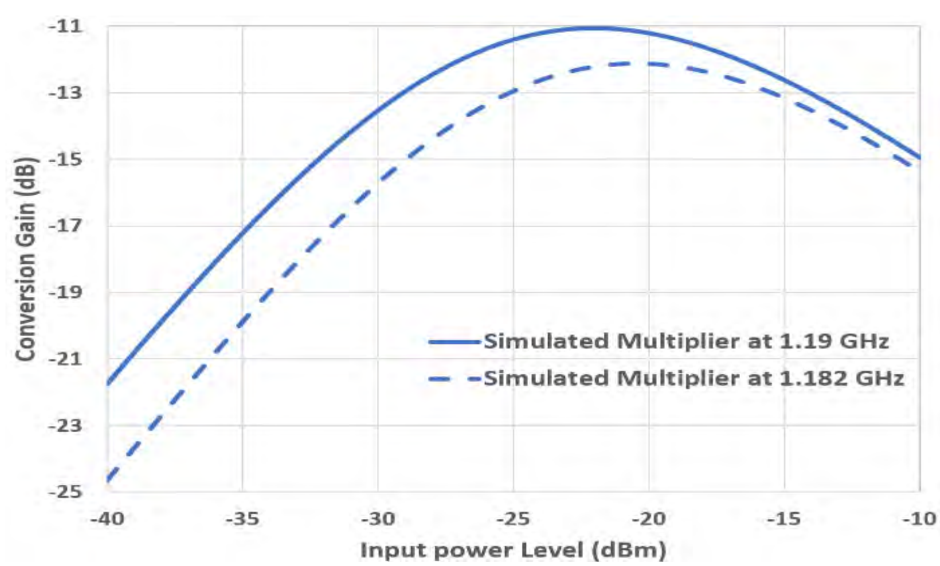

Figure 2.35 Comparison of simulated CG at 1.182 and 1.19 GHz.

The measured vs. simulated received signal variation in the E- and H-planes for the input power level of -20 dBm are given in Fig. 2.36. The parameters are normalized to the maximum signal level measured at θ=180º. Since the receiver antenna gain changes by changing the θ angle, the input power level and so CG is different for each case. Therefore, the calculated parameters take the receive and transmit antenna gains as well as the corresponding simulated CG into account. The results show that the variation in the H-plane is only 2 dB, while it is around 30 dB in E-plane. Thus, making the measurements in the H-plane for the sensing applications would be very stable and so more favorable. Another important measured FDR parameter is the cross-polarization isolation level. It is described as the signal level difference between co- and cross-polarization and is measured around 40 dB.

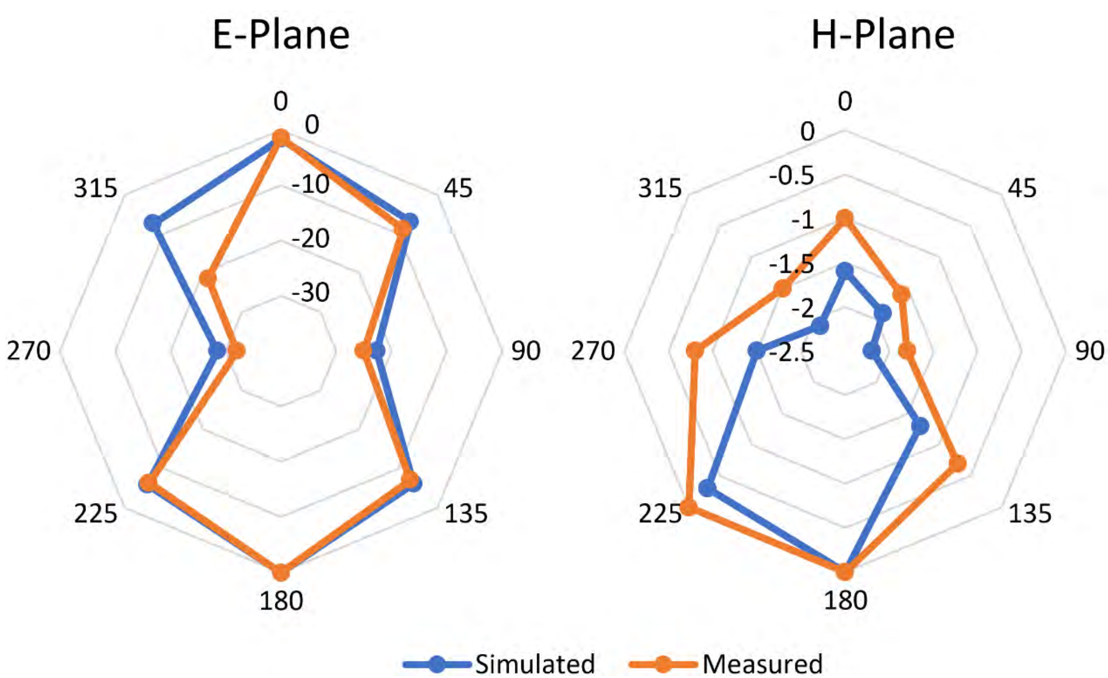

Figure 2.36 Measured vs. Simulated Signal Variation in E and H Planes.

Fig. 2.37 shows the simulated CG vs. frequency along with the 3-dB bandwidth of the FDR for different input power levels. It reveals that the bandwidth increases with the input power level. This is because the input and output impedances of the multiplier change faster by reducing the input power level. The simulated and measured bandwidths for -20 dBm are 2.9% and 2.6%, while they are 1.5% and 1.4% for -30 dBm. The measured bandwidth is narrower than the simulated since the fabricated FDR already has small impedance mismatches, which led to the resonant frequency shift and dropping the conversion efficiency.

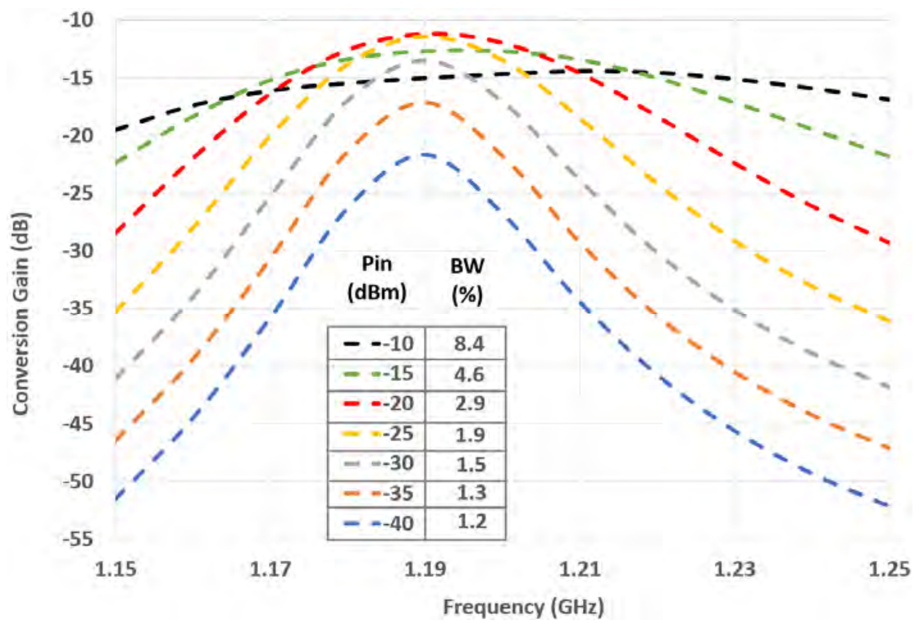

Figure 2.37 Simulated bandwidth of the FDR for different input power levels.

2.6. Mechanical Tunability of the FDR

The CG is very sensitive to the input and output impedance matching of the diode at f_0 and $2f_0$. Due to fabrication tolerances or anticipated packaging effects, the optimal impedance match frequency f_0 can shift at the input of the doubler, while the output impedance match may not have a corresponding shift. To overcome these issues, or simply to change the operational f_0 as needed, a bias voltage can be applied to the input of the receive antenna, as explained in [35]. However, this method requires attaching a battery to the FDR. So, having a design that can be mechanically tunable would allow maintaining the FDR battery-free. Therefore, in this section, two potential fully passive tunability techniques are discussed.

2.6.1. Tuning by Dielectric Loading

The dielectric loading in the form of 3-layer substrate stacks made from the FDR material of Rogers 3010 is used, as seen in Fig. 2.38(a). By mechanically moving the loading in X and Y directions and covering some portion of the meandered line sections at the receive and transmit sides, the matching frequencies at input and output are independently controlled. As shown in Fig. 2.38(b), it is possible to shift f_0 between 1.16 and 1.185 GHz; based on several fabricated FDR units, this range is sufficient to correct for variations observed even with the manual assembly process that has been used. The thickness of the stacks affects the characteristic impedance of the line; increasing the thickness reduces the characteristic impedance. So, it should be optimized in the simulations. As seen in Fig. 2.39, the substrate stacks are held by plastic screws and 3D-printed structures that are attached to the top side of the antennas. In this location, there is minimal effect on the radiation patterns. Additionally, because the stacks are located in between the antennas, they do not impact the overall size of FDR.

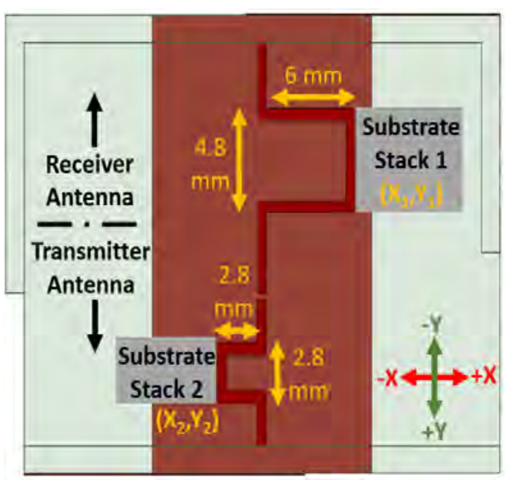

(X_1,Y_1) & (X_2,Y_2) (mm)	f_0 (GHz)
(-0.5,0) & (1,0)	1.185
(-1,0) & (1.3,0)	1.175
(-3.5,0.5) & (1.6,0)	1.165
(-5,1.5) & (1.9,0)	1.16

a) b)

Figure 2.38 a) Top view of FDR that shows the locations of substrate stacks for tuning. b) fundamental frequency change based on location of substrate stacks used as dielectric loading.

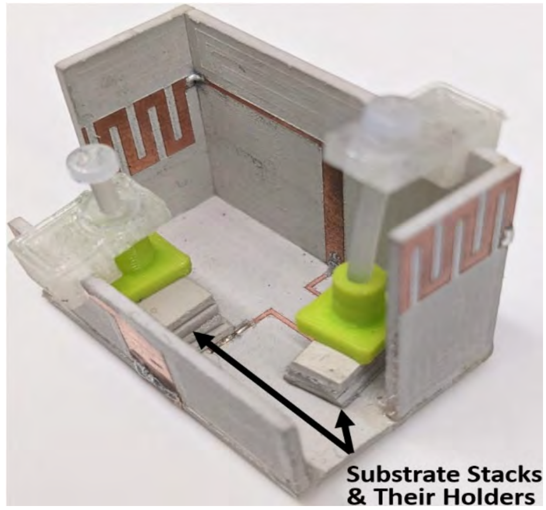

Figure 2.39 Fabricated FDR with substrate stacks for impedance tuning.

2.6.2. Tuning by Attaching Copper Patch

Tunability can also be achieved by adding copper patches to the corner of the meandered sections of the impedance matching lines, as seen in Fig. 2.40 (a). These patches act as an open-circuited stub and make a capacitive effect. Based on the width and length, the capacitive effect increases or decreases and so can help shift the resonance frequency. Fig. 2.40 (b) shows the simulated frequency change based on the size of the patches.

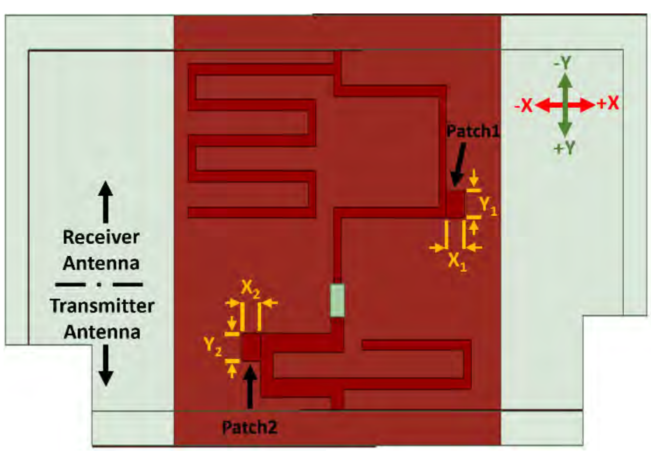

a)

(X_1,Y_1) & (X_2,Y_2) (mm)	f_0 (GHz)
(0.4,1) & (0.3,1)	1.185
(1.2,1) & (0.8,1)	1.175
(2,1) & (1.4,1)	1.165
(2.2,1) & (1.5,1)	1.160

b)

Figure 2.40 a) Top view of FDR that shows the locations and width and length of copper patches for tuning. b) fundamental frequency change based on the size of the patches.

2.7. Temperature Dependence of the FDR

Temperature dependence of the multiplier is another important aspect of the FDR design for environmental sensing. The FDR is expected to be able to continue its operations efficiently at the temperature range of the ambient environment. The diode model provided by Modelithics Inc. allows making simulations with varying junction temperatures (T_j) between 25 and 85 ºC. T_j is defined as the combination of the ambient temperature and the temperature rise due to the power dissipation in the diode while operating. According to [43], the measured CG of SMS7630 at -25 dBm input power level decreases by 2 dB when the ambient temperature rises from 25 to 40 ºC, which matches well with the simulation results in Fig. 2.41. This proves that the temperature rise due to the power dissipation in the diode is very low, and so T_j is heavily dependent on the ambient temperature. Fig. 2.41 also reveals that the CG is still within 3 dB bound when the temperature rises to 55 ºC. On the other hand, the CG increases by 3 dB when the temperature drops to -20 ºC [43]. Therefore, the CG of the multiplier varies +/- 3

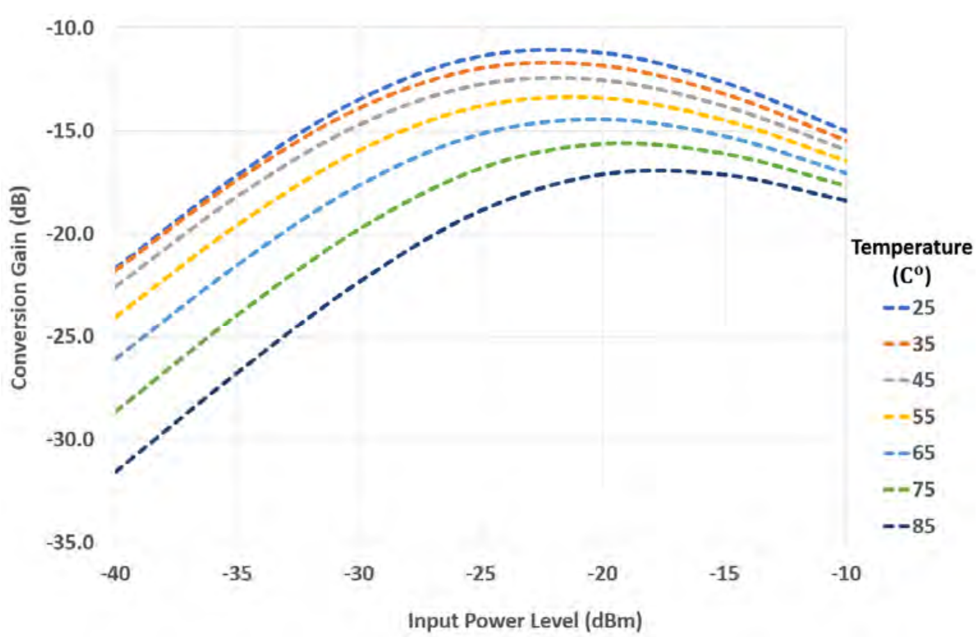

Figure 2.41 CG change with junction temperature varying between 25 to 85 ºC.

dB at ambient temperatures of -20 to 55 ºC, which means it can be used in different weather conditions.

2.8. Conclusions

Battery-free, mechanically tunable, high interrogation range, omnidirectional, and narrowband FDR designs are investigated. A highly accurate FDR model is created in simulations and explained in detail. Two different FDR designs that employ Skyworks SMS7630-079LF and Keysight HSCH-9161 diodes are proposed and compared to each other. Experimental results, which are in very good agreement with the simulated results, reveal that the FDR design with SMS7630 provides better conversion gain to work with an interrogator at low power levels for extending the interrogation range. Two different mechanical tuning capabilities are presented, which provide opportunities to shift the narrowband response to different frequencies, account for parasitic effects from future package designs, and improve overall manufacturing yield and cost. The temperature dependency of the FDR is also investigated to be used in different environmental conditions. The results show that only a 3 dB variation is observed between the ambient temperatures of -20 and 55 ºC, and the colder the temperature leads to the higher CG.

Chapter III :

A Semi-Empirical Model for Predicting the Effects of Moisture on Microwave Signal Attenuation in Fouled Railroad Ballast

3.1. Introduction

Monitoring the moisture content in natural and built infrastructure can provide crucial information about structural integrity. When moisture content exceeds an acceptable limit in such environments, infrastructure failures may occur. An example that motivates the presented research concerns railbed, which can become structurally compromised when the supporting ballast becomes fouled (with dust and/or dirt) and retains water (Fig. 3.1). Above a certain moisture level, the ballast material is loosened, and the railroad track can fail under the load of train traffic. Monitoring moisture level and retention in the ballast on a regular basis can be part of a preventative maintenance and ballast repair process to avoid such failure scenarios.

In this study, we propose that long-term, real-time, and low-cost moisture monitoring of the railbed can be accomplished using a passive embedded harmonic transponder design we refer to as a frequency-doubling reflectenna (FDR). Prior work has shown that one can remotely interrogate FDRs embedded in up to 1 m deep in soil and characterize the soil's moisture [44]. When the passive FDR receives low power signals at the fundamental frequency (f_0), it transmits signals at the second harmonic frequency ($2f_0$) back to the interrogator. By analyzing the difference between transmitted and received signals, the attenuation level in the ballast can be obtained, which could be used as a reference for determining the moisture level. However, these

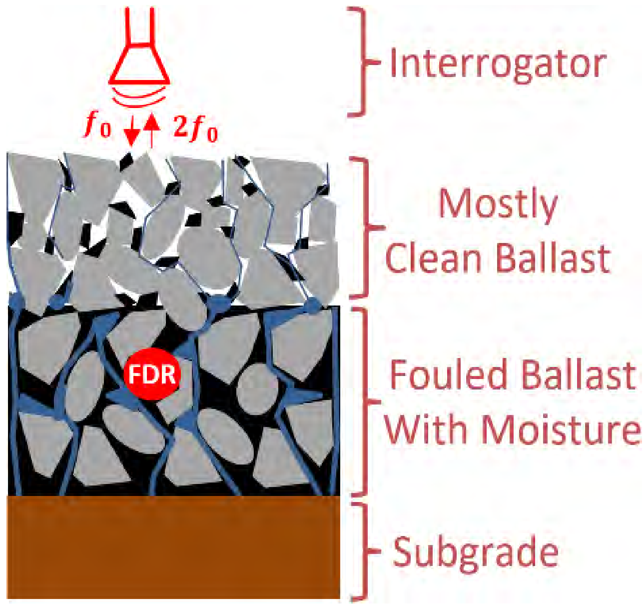

Figure 3.1 Ballast cross-section and the FDR sensor being interrogated with an RF signal in ballast.

results do not directly translate to the railbed application, due to the heterogeneity of railbed structure and materials.

Herein, we present a semi-empirical dielectric mixing model to analyze the moisture level in heterogeneous and multi-dielectric compositions of ballast, fouling (coal dust), moisture (water), and void (air). The model takes the dielectric properties and the volumetric percent composition of the materials in the mixture individually and creates a single complex permittivity of the mixture. The attenuation of microwave signals in the ballast is then calculated from the complex permittivity of the mixture and compared with the measured attenuation. The calculated data are in very good agreement with the measured data, giving evidence that this model is able to accurately correlate the signal attenuation with moisture level.

The measured data with moisture is introduced in Section II, and the dielectric mixing model in Section III. Then, it continues by discussing the validity of measurement results by comparing the data obtained from the mixing model in Section IV and ends with conclusions.

3.2. Measured Data with Moisture

To demonstrate the viability of using the proposed FDR-based passive sensing system, a series of controlled experiments were conducted to ascertain the wireless signal attenuation through a ballast stack under various fouling conditions. The ballast (porosity = 44%) was contained in a ~0.23 m^3 volume and had a height of 0.381 m (15 in). Coal dust was used as the fouling agent (porosity = 40%) and water was added. Fig. 3.2 (a) illustrates the ~5 cm ballast with finer grain fouling. Fig. 3.2 (b) illustrates the 0setup to measure the relative one-way path loss between the transmit antenna located ~0.5 m above the ballast stack and receiving antennas located ~0.1 m below the stack and above anechoic material. The test container held the fouled ballast.

Our tests were conducted under conditions that are considered "fouled ballast" [45], where one-fourth of the ballast (11% of total volume) void space was filled with

(a) (b)

Figure 3.2 (a) Ballast with coal dust fouling, (b) ~0.2 m^3 test container with antennas above and below to measure signal attenuation.

(a)

(b)

Figure 3.3 The percent composition by volume of each material (a) in total volume and (b) in fouling (50% moisture case shown here).

coal dust (Fig. 3.3(a)). Moisture conditions from dry (0%) to saturation (100%) of the coal dust were investigated. Coal dust consists of 60% solid material and 40% void space in dry conditions. When 50% of the void space in coal dust is filled with moisture, the case is called 50% moisture, as seen in Fig. 3.3(b). At saturation, 100% of the void space in coal dust (or 4.4% of the total test volume) was water. For the tested frequencies, the added attenuation was ~0.4 dB/m/% moisture for the frequencies of 900 MHz, 1.2 GHz, and 1.8 GHz and ~0.6 dB/m/% moisture for 2.4 GHz. These data suggest that an interrogation frequency (f_0) of 1.2 GHz satisfies the tradeoff of relatively low loss on the forward link, distinguishable loss on the return link (at $2f_0$), and a compact FDR design that this relatively high frequency enables.

3.3. Simulation Approach

Dielectric mixing models are studied and developed in Ansys High Frequency Structure Simulator (HFSS) for analysis of ballast conditions and signal propagation through the ballast medium and at the boundaries. Floquet ports in HFSS are used to examine infinitely long and planar periodic structures in a single unit cell [46]. Thus, in this study, they are employed to analyze the infinitely long, heterogeneous, and multi-dielectric structure of railroad ballast in an electrically small cubic unit cell as

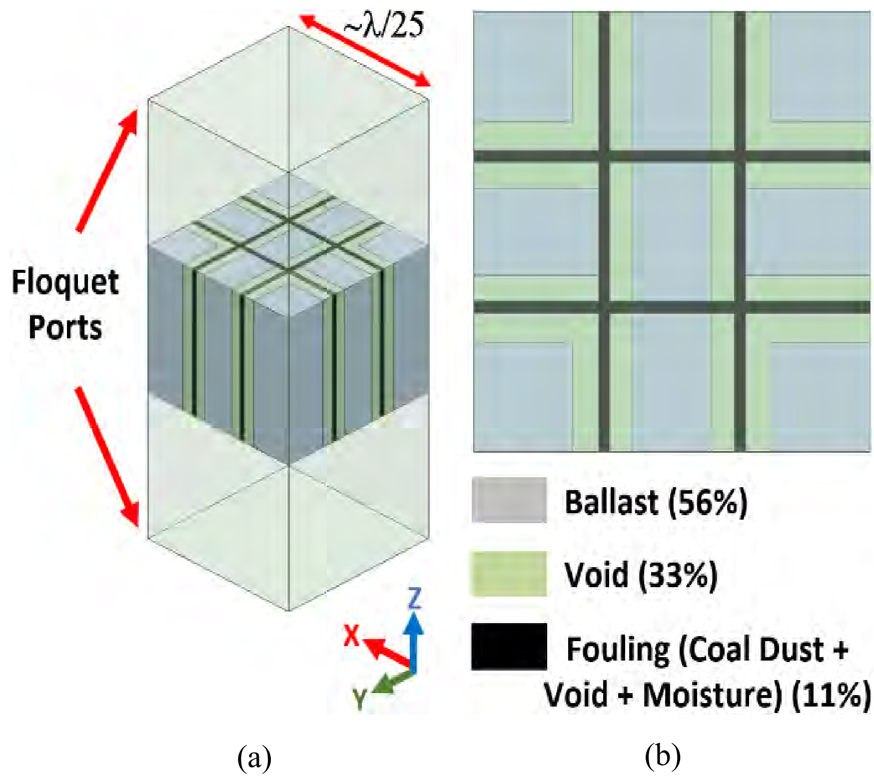

Figure 3.4 (a) Simulated 3D cubic unit cell with Floquet ports, (b) top view of the cell with color map of each element in total volume.

seen in Fig. 3.4(a). Two ports are defined at the top and the bottom of the cell for reflection and transmission coefficient computation. Both sides of the cell are surrounded by primary and secondary boundaries to define infinite periodicity in the x and y directions. The volumetric percentages of each material mentioned in Fig. 3.3(a) are represented by a discrete portion of the unit cell's total volume. As shown in Fig 3.4(b), ballast, void, and fouling (mixture of coal dust, void, and moisture) cover 56%, 33%, and 11% of the total volume, respectively. As described below, measured data for the fouling are used in the simulation model. The measurements are made at 1.2 GHz by using a Keysight N1501A dielectric probe, as shown in Fig. 3.5, and the results are given in Table 3.1.

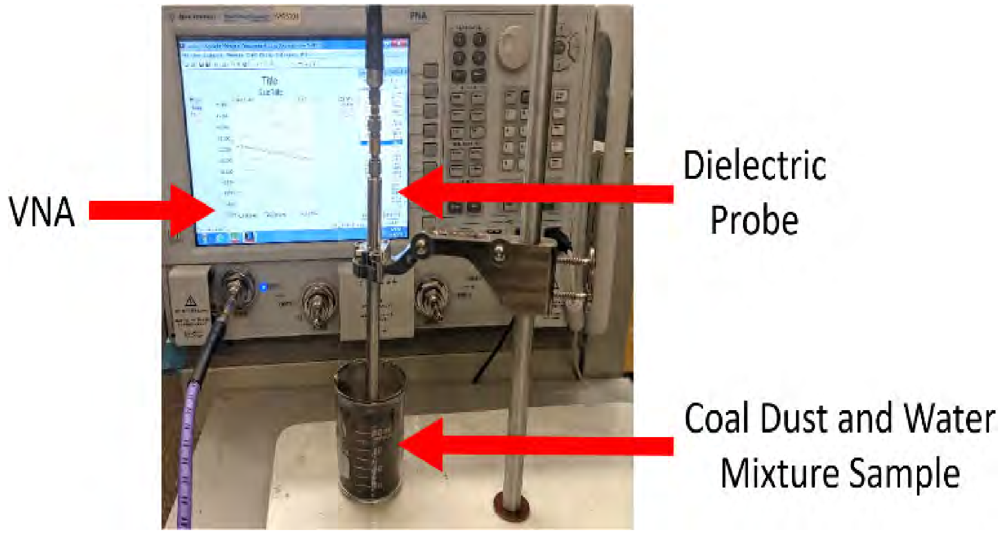

Figure 3.5 Material dielectric characterization test setup.

The propagation of plane waves in the medium created by the Floquet ports is dependent on the geometry of the structure. The uniform distribution of the different materials in the x-y direction across the unit cell results in a good approximation of the propagation of microwave signals in the physical ballast test structure. Furthermore, the symmetry of the geometry provides the benefit of polarization independence.

Table 3.1 Measured Permittivity and Loss Tangent of Materials in Fouled Ballast Conditions

Material	ε_r	$\tan \delta$
Ballast	4.5	0.02
Water (Tap)	79.5	0.065
Void (Air)	1	0
Dry Coal Dust	3.3	0.04
25 % Moisture in Coal Dust	6.8	0.28
50 % Moisture in Coal Dust	12.3	0.3
75 % Moisture in Coal Dust	23	0.35
100 % Moisture in Coal Dust	38	0.33

While some improvements in the model accuracy were observed when dividing the different materials into a greater number of smaller regions, the geometry in Fig. 3.4 is a good compromise between accuracy and computational time and complexity.

The reflection (S(1,1)) and transmission (S(2,1)) coefficients obtained from the Floquet port simulations are converted to permittivity and loss tangent by using Nicholson-Ross-Weir (NRW) method [47]. The method requires to use of a short sample thickness; the optimum edge length of the cubic unit cell was found to be ~λ/25.

An important observation in this work is that neither established mixing models [e.g., 48,49] nor the HFSS simulations will accurately predict the complex permittivity of the composite coal dust–moisture mixture, especially at higher moisture levels. In our experiments, it was found that there is a non-linear relationship between the material composition and the resulting loss tangent that these models do not predict. For example, as seen in Table 3.1, the loss tangent of dry coal dust and water are 0.04 and 0.065, respectively. However, when a small amount of water is introduced to coal dust, the loss tangent of the mixture becomes around 0.3. For this reason, the measured data for the permittivity of the fouling is used.

Table 3.2 Effective and Median Permittivity and Loss Tangent of the Mixture in Fouled Ballast

Material	ε_r	$\tan\delta$
0% Moisture in Total Volume	2.50	0.014
25 % Moisture in Total Volume	2.79	0.057
50 % Moisture in Total Volume	3.15	0.083
75 % Moisture in Total Volume	3.80	0.135
100 % Moisture in Total Volume	4.72	0.165

3.4. Measurement Validation

The effective permittivity and loss tangent of the mixture given in Table 3.2 are calculated by using the NRW method, and they are converted to attenuation by using (3.1). Then, the results are multiplied by the thickness of the container used in the measurements, 0.381 m (15 in), to find the attenuation in dB.

$$\alpha = \omega\sqrt{\frac{\mu_0\varepsilon_0\varepsilon'}{2}\left[\sqrt{1+\tan\delta^2}-1\right]}\ \text{x}\ 8.686\ \ {}^{\text{dB}}\!/_{\text{m}} \tag{3.1}$$

The calculated and measured attenuation values are compared in Fig. 3.6. All attenuation values are normalized to the dry condition. The median values, along with maximum and minimum bars, are given in the figure. Very good agreement in the median results indicates that the dielectric mixing model can accurately predict the

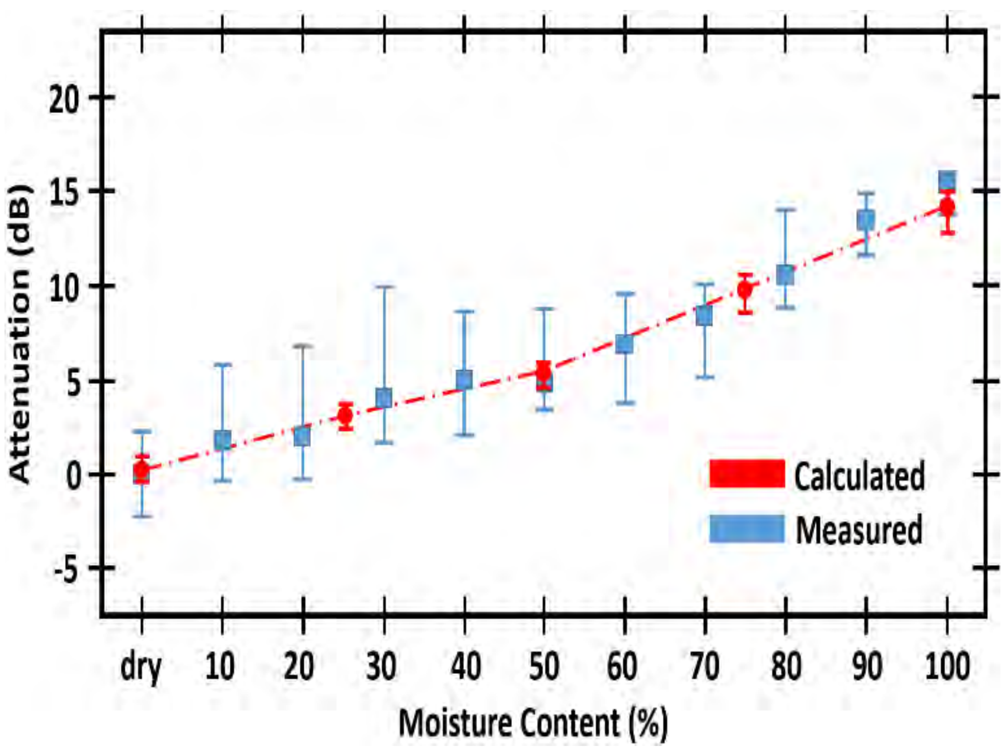

Figure 3.6 Comparison of measured and calculated attenuation in ballast, including median, minimum and maximum values.

attenuation in all moisture cases. The variation in the measured data at each moisture level results from measuring the signal attenuation at multiple locations below the ballast. It can be also observed from the figure that the attenuation does not increase linearly with the moisture content due to the nonlinear increase in dielectric properties.

3.5. Conclusion and Discussion

A semi-empirical dielectric mixing model has been proposed to aid in the prediction of moisture levels for railroad ballast based on microwave signal propagation measurements. The model calculates the dielectric properties of the heterogeneous and multi-dielectric composition of ballast, fouling material, and moisture based on their volumetric percent composition. The calculated attenuation results from the dielectric properties are in good agreement with lab experiments. The results show the potential for real-time and long-term monitoring of moisture content in railbed ballast using embedded wireless sensors.

Chapter IV :

Interferometric Sensing for Localization and Displacement Measurements

4.1. Introduction

Displacement sensing of an environment can give important insight into its structural health condition. The displacement could occur below the ground due to natural or non-natural reasons such as erosion, landslides, freeze-thaw cycling, or excessive loading, and monitoring it continuously can help take the necessary actions before infrastructure failures happen. Current monitoring techniques typically are expensive, time-consuming, and require significant human effort [50]. The proposed energy-efficient, low-cost, and long-term monitoring technique described here has the capability of regularly and autonomously measuring and characterizing the displacement by employing a pair of FDR sensors excited by an interrogator above the ground. A drone-based interrogator is a good candidate for reducing human effort significantly.

It is likely that an important first step in measuring displacement is to accurately localize the position of the FDR sensors. A global positioning system (GPS) sensor has been used for localization purposes, but it is mainly useful for applications that do not require high precision. The highest possible position accuracy of GPS sensors is 30 cm, according to [51], while accuracy down to a few cm is possible using the proposed FDR-based method. An alternative method could be visual, above-ground markers that designate sensor location, but this may not be practical depending on the nature of the surrounding environment. Furthermore, along with displacement measurements, even those applications that involve sensing with a single FDR (such as the ballast fouling system described in Chapter I) will require tight control over the relative location and orientation of the interrogator and the FDR.

The model in Fig. 4.1(a) illustrates how the localization measurements can be accomplished with the interferometric approach. If the interrogator can move between the pair of FDRs, it will receive the maximum signal when positioned at the exact center of the FDRs. The signal level will decrease as it moves off the center, and the lowest signal (a null) will be observed within several cm of the center location, depending on the specific parameters of the FDR arrangement and operating frequency. A single FDR could also be used for localization purposes, but its response will change slower than two FDRs as the interrogator moves off the center. Thus, the FDR pair would allow detecting the location more accurately.

In addition to localization, the use of two FDR sensors can be applied for displacement sensing. There are three types of displacement sensing scenarios considered in this work:

a) A non-fixed sensor (FDR2) and an anchored (fixed) sensor (FDR1) are placed in the same orientation, and the interrogator is positioned above FDR1, as illustrated in Fig 4.1(b). When two FDR sensors are interrogated simultaneously, the combination of the returned signals will vary with FDR spacing. The signal received and transmitted by FDR2 travels through the additional path length of $l * (sec\theta - 1)$ compared to FDR1, resulting in a phase difference of δ. If the signals are in-phase, constructive interference occurs, otherwise destructive interference will be observed.

b) Both sensors are non-fixed, and the interrogator moves and excites them from different angles. From the constructive and destructive interference locations, the spacing between the sensors can be calculated.

c) A non-fixed sensor (FDR2) positioned at the reverse orientation (flipped) compared to an anchored (fixed) sensor (FDR1). The phase response of FDR2 will be 180º different than before flipping it as in scenario (a). Therefore, destructive interference will be observed when interrogating them from the same angle as opposed to the constructive interference seen in scenario (a).

The responses of the FDR1 and FDR2 used in the measurements must be individually characterized to estimate their combined response when interrogated simultaneously. Thus, the first part of this chapter presents the characterization of a single FDR node. The second part shows the localization measurements with a pair of FDRs. The third part discusses the three different scenarios for displacement sensing in detail, followed by conclusions.

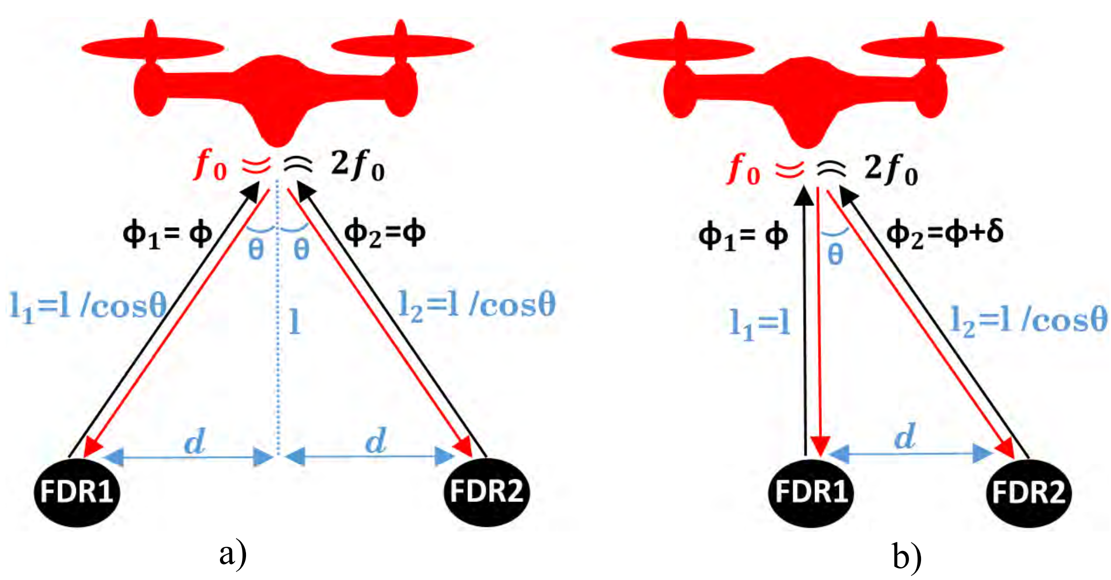

Figure 4.1 Simultaneously interrogating two FDR sensors for a) localization and b) displacement measurements.

4.2. Measurement Setup

The measurement setup given in Section 2.3.2 is modified to use a single antenna (horn antenna) for interrogation to reduce the complexity of signal analysis from single or especially multiple FDRs. A power divider is used to separate the transmitted f_0 signal from the received $2f_0$ signal (a circulator could ideally be used). The isolators are placed at the input and output to minimize the effect of impedance mismatch. The complete diagram is seen in Fig. 4.2.

Fig. 4.4 shows the measurement setup where the FDR is located 30" (76.2 cm) away from the interrogator antenna (IA). The FDR is placed at the center and is able to move +/- 50 cm on the Y axis on a foam board, which has a dielectric constant close to 1.0. The setup is surrounded by RF absorbers. The equipment and components used in the tests that are mentioned in Fig. 4.2 are shown in Fig. 4.3.

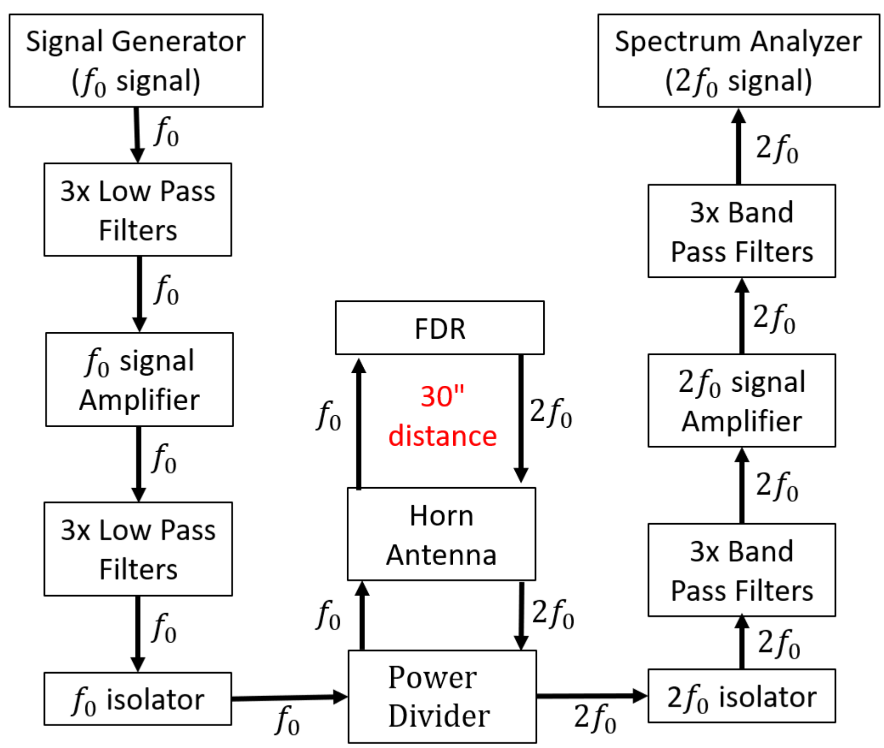

Figure 4.2 FDR testing diagram.

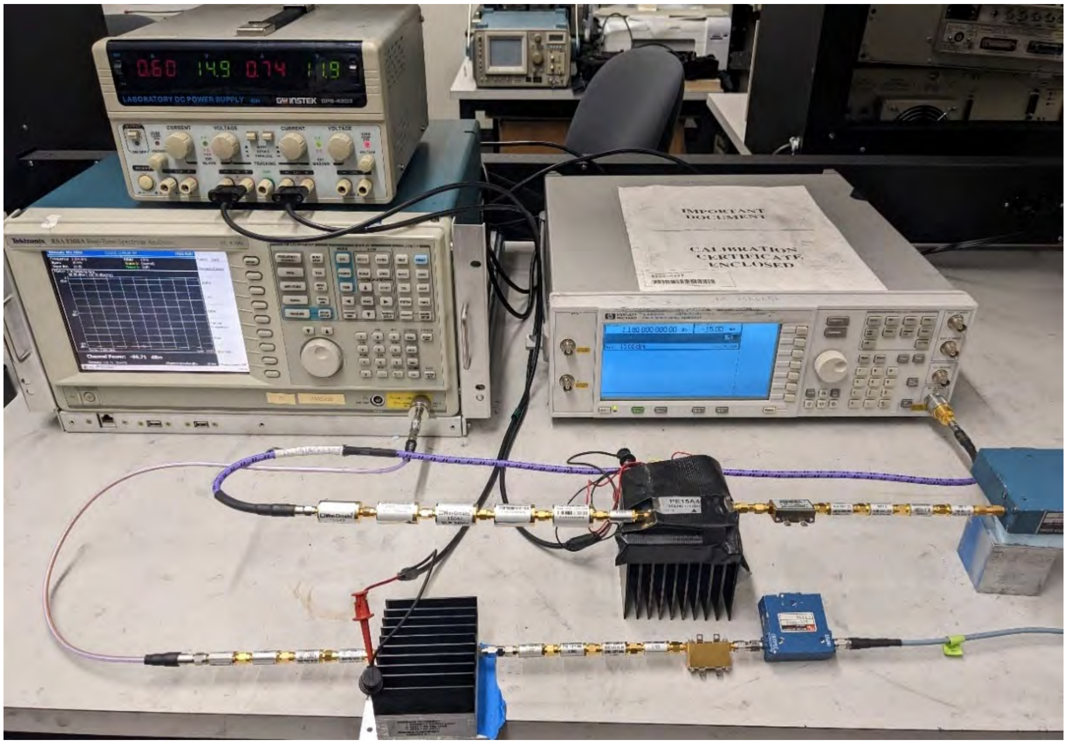

Figure 4.3 Test equipment and components.

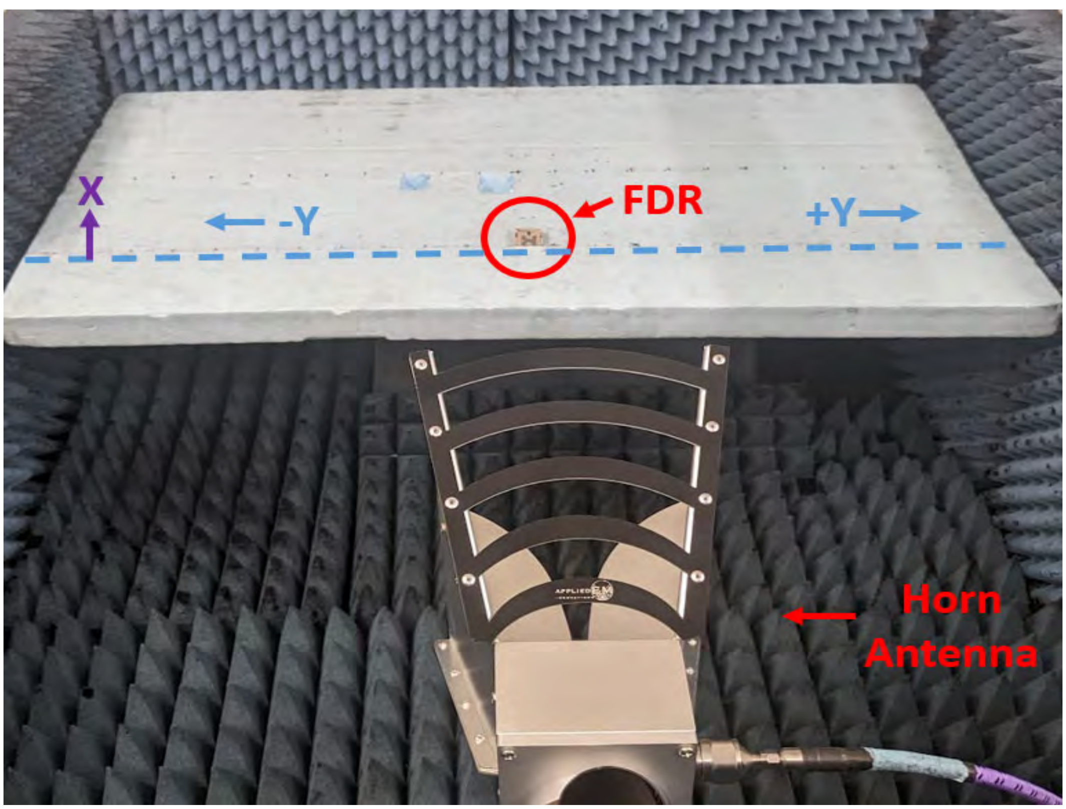

Figure 4.4 Measurement setup.

4.3. Single FDR Measurements

The signals from FDR1 and FDR2 were measured individually by IA along the y-axis. The distance from the IA location to the center of FDR is described as $y_{IA\text{-}FDR}$ as seen in Fig. 4.5. Starting from $y_{IA\text{-}FDR}$= +50 cm location, the IA moved in the -y direction and measured the signal from the FDR at every 5 cm (~0.2λ_0) until $y_{IA\text{-}FDR}$= -50 cm location. Each measurement location ($y_{IA\text{-}FDR}$) can be interpreted with a corresponding interrogation angle (θ) given in Table 4.1. To verify the accuracy of the measurement results, link budget calculations are made based on the formula (4.1). The calculated received powers (P_r) from each location are then normalized to the peak signal level received at y=0 (4.2). Each parameter in the formulas is explained below.

$$P_r(\theta)^{[dBm]} = P_t^{[dBm]} + G_{IA,f_0}(\theta)^{[dBi]} + 20\log\left(\frac{\cos\theta\ x\ c}{4\pi l f_0}\right)^{[dB]} + G_{FDR,f_0}(\theta)^{[dBi]} +$$
$$CG^{[dB]} + G_{FDR,2f_0}(\theta)^{[dBi]} + 20\log\left(\frac{\cos\theta\ x\ c}{4\pi l 2f_0}\right)^{[dB]} + G_{IA,2f_0}(\theta)^{[dBi]} \quad (4.1)$$

$$[P_r(\theta)^{[dB]}]^N = P_r(\theta)^{[dBm]} - P_r(\theta = 0^o)^{[dBm]} \quad (4.2)$$

a) Find the IA gain at f_0 frequency and θ interrogation angle. $(G_{IA,f_0}(\theta)^{[dBi]})$

b) Calculate the path loss at f_0 frequency based on the distance (l/cos θ) between the FDR and the interrogator. ($20\log\left(\frac{\cos\theta\ x\ c}{4\pi l f_0}\right)^{[dB]}$ where c is the speed of light)

c) Find the FDR receive antenna gain at f_0 frequency and θ angle. $(G_{FDR,f_0}(\theta)^{[dBi]})$

d) Combine the gains and losses at parts a, b, and c with the transmitted power (P_t), calculate the input power applied to the doubler. Based on the input power level, calculate the corresponding conversion gain. ($CG^{[dB]}$)

e) Find the FDR transmit antenna gain at $2f_0$ frequency and θ angle. $(G_{FDR,2f_0}(\theta)^{[dBi]})$

f) Calculate the path loss at $2f_0$ frequency based on the distance ($l/\cos\theta$) between the FDR and the interrogator. $(20\log(\frac{\cos\theta \ x \ c}{4\pi l 2f_0})^{[dB]}$ where c is the speed of light)

g) Find the IA gain at $2f_0$ frequency and θ angle. $(G_{IA,2f_0}(\theta)^{[dBi]})$

h) Combine all mentioned above and normalize to the signal level calculated at the $y_{IA\text{-}FDR}$=0 cm location (θ=0°), where the peak signal is received.

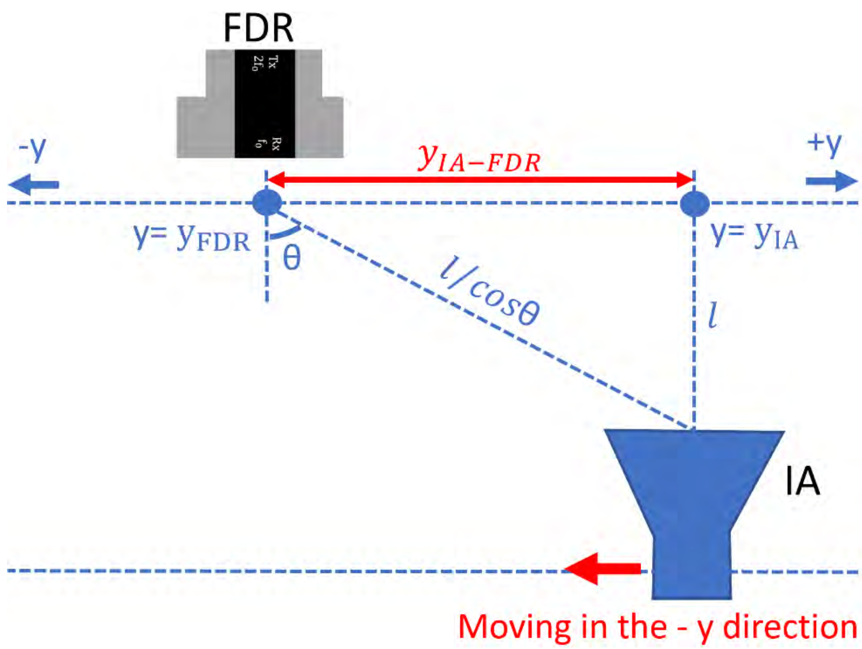

Figure 4.5 Single FDR measurement parameters.

The measured signal level closely matches the calculations, as seen in Fig. 4.6. As expected, the maximum signal level is received at the center location for the FDR since both IA and FDR antennas have peak radiation at this location as well as being the smallest path length. Although the signal level drops gradually on both the (+) and (–)

y-axis, they are not exactly symmetric. This happens due to the tilted radiation pattern of a single FDR mentioned in Chapter II. This change in the antenna gain also leads to a change in the input power level to the doubler, and this changes the conversion gain.

Table 4.1 Distance between IA and the FDR ($y_{IA\text{-}FDR}$) and its corresponding interrogation angle (θ).

$y_{IA\text{-}FDR}$ (cm)	θ (deg)
50 or -50	33
45 or -45	31
40 or -40	28
35 or -35	25
30 or -30	21
25 or -25	18
20 or -20	15
15 or -15	11
10 or -10	7
5 or -5	4
0	0

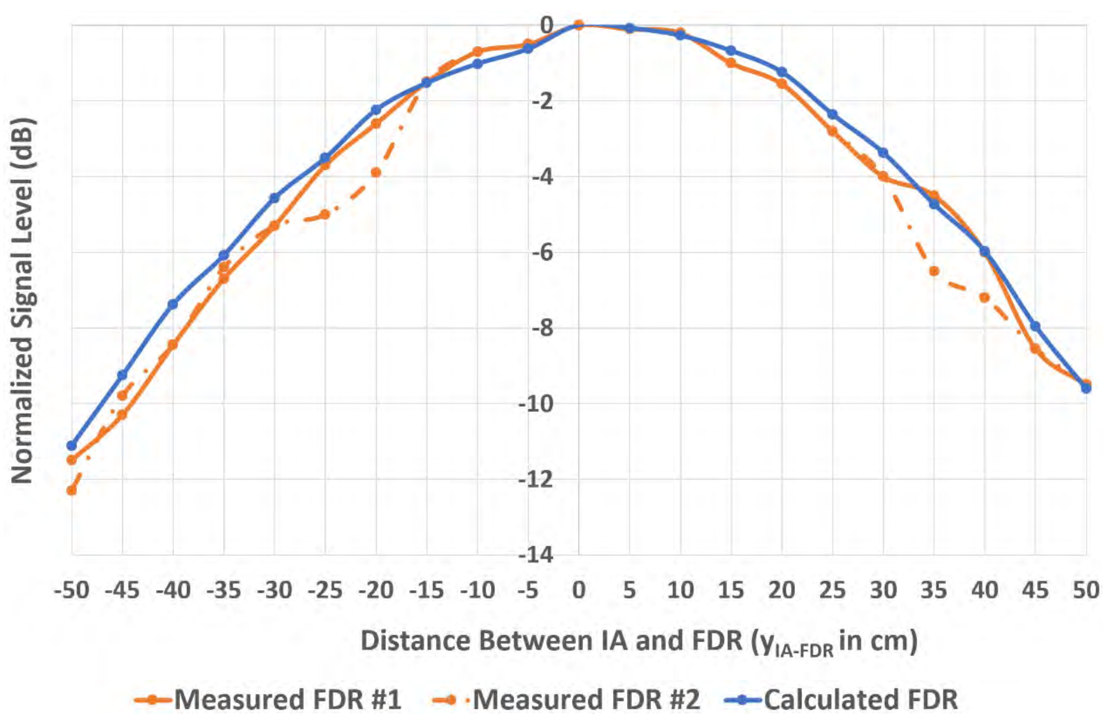

Figure 4.6 Measured vs. Calculated single FDR.

From Fig. 4.6, it can be seen that a single FDR could be used for localization since a peak in the received power occurs at the center and the level reduces monotonically as the FDR moves off center. However, the measurements with two FDRs enables more precise localization, as explained below.

4.4. Localization Measurements with Two FDRs

The localization measurements can be accomplished with the interferometric sensing approach by using a pair of FDR sensors. As seen in the measurement model in Fig. 4.7, FDR1 and 2 are positioned on the y-axis with a separation distance of 25 cm (~λ_0) that is called "d", and their center is called y=0. The IA is positioned l cm away from them, and its distance to the center of FDRs in the y-axis is called y_{IA}. Starting from y_{IA}=37.5 cm, the IA moved in the -y direction and measured the signals from the FDRs at every 5 cm (~0.2λ_0) until y_{IA}= -37.5 cm location. The phase difference between the received signals from FDR1 and 2 at a y_{IA} location can be calculated by using:

$$\Delta\phi\ (y_{IA}) = \phi_{FDR1}(\theta_1) - \phi_{FDR2}(\theta_2) = l\ x\left(\frac{1}{cos\theta_1} - \frac{1}{cos\theta_2}\right) x \left(\frac{360^o x(f_0+2f_0)}{c}\right) \tag{4.3}$$

where f_0 is the operation frequency, c is the speed of light, and θ_1 and θ_2 are the interrogation angle of FDR1 and 2 when IA is positioned at y_{IA} location. In 4.3, $l\ x\left(\frac{1}{cos\theta_1} - \frac{1}{cos\theta_2}\right)$ is the physical path length difference (in meters), and the remaining part is the phase constant (in degrees/meter). The two frequency components (f_0 and $2f_0$) are used in the phase constant due to the frequency change while traveling through the path. The FDR1 and 2 are considered as individual voltage sources, and thus the combination of their signals can be calculated as voltage gain.

If $\theta_1 > \theta_2$, then

$$P_{combined}^{[dB]}(y_{IA}) = 20\log\left(10^{(P_{FDR1}(\theta_1)/20)} + 10^{(P_{FDR2}(\theta_2)/20)} * \cos\left(\Delta\phi\,(y_{IA})\right)\right) \quad (4.4)$$

If $\theta_1 < \theta_2$, then

$$P_{combined}^{[dB]}(y_{IA}) = 20\log\left(10^{(P_{FDR2}(\theta_2)/20)} + 10^{(P_{FDR1}(\theta_1)/20)} * \cos\left(\Delta\phi\,(y_{IA})\right)\right) \quad (4.5)$$

where P_{FDR1} and P_{FDR2} are the individually measured powers from FDR1 and 2 at θ_1 and θ_2 interrogation angles that are given in section 4.3, respectively. If the combined signal level is normalized to the single FDR signal level (P_{FDR1} or P_{FDR2} whichever is higher) by using

$$\text{If } \theta_1 > \theta_2,\ [P_{combined}(y_{IA})^{[dB]}]^N = P_{combined}(y_{IA})^{[dB]} - P_{FDR1}(\theta_1)^{[dB]} \quad (4.6)$$

$$\text{If } \theta_1 < \theta_2,\ [P_{combined}(y_{IA})^{[dB]}]^N = P_{combined}(y_{IA})^{[dB]} - P_{FDR2}(\theta_2)^{[dB]} \quad (4.7)$$

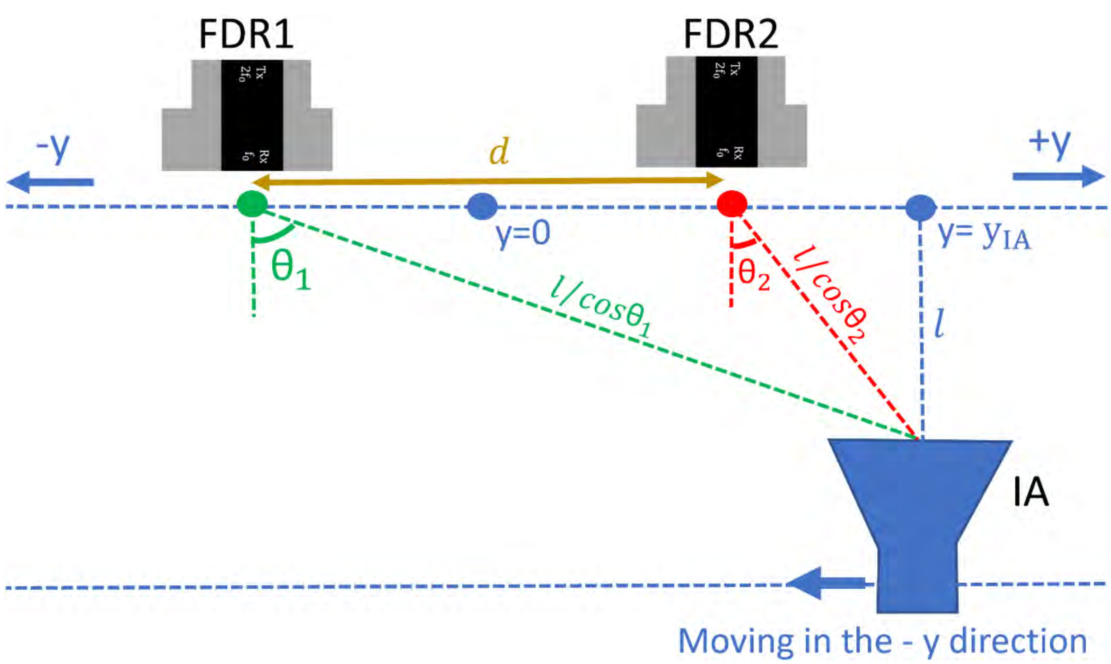

Figure 4.7 Displacement measurement with two FDRs – IA moves along the y-axis.

The interrogation angles, θ_1 and θ_2, are the most important components in the received power calculations. Based on their values, the phase differences in received signals from FDR1 and 2 occur, thus constructive or destructive interferences happen. Fig. 4.8 shows the measured and simulated received signal levels vs. interrogator antenna location. When the IA is positioned at the center of FDRs, the maximum signal (peak) is received. Whenever it moves off the center, a destructive interference started observing and further move resulted in a null in the received signal. These peaks and nulls in the received signal can provide information about the FDRs locations. Additionally, compared to Fig. 4.6, the received signal in this figure degrades more rapidly. Therefore, the sharp difference between the peak and null (around 18 dB) with the pair of FDR measurements can help us to identify the location information with much higher accuracy than with a single FDR.

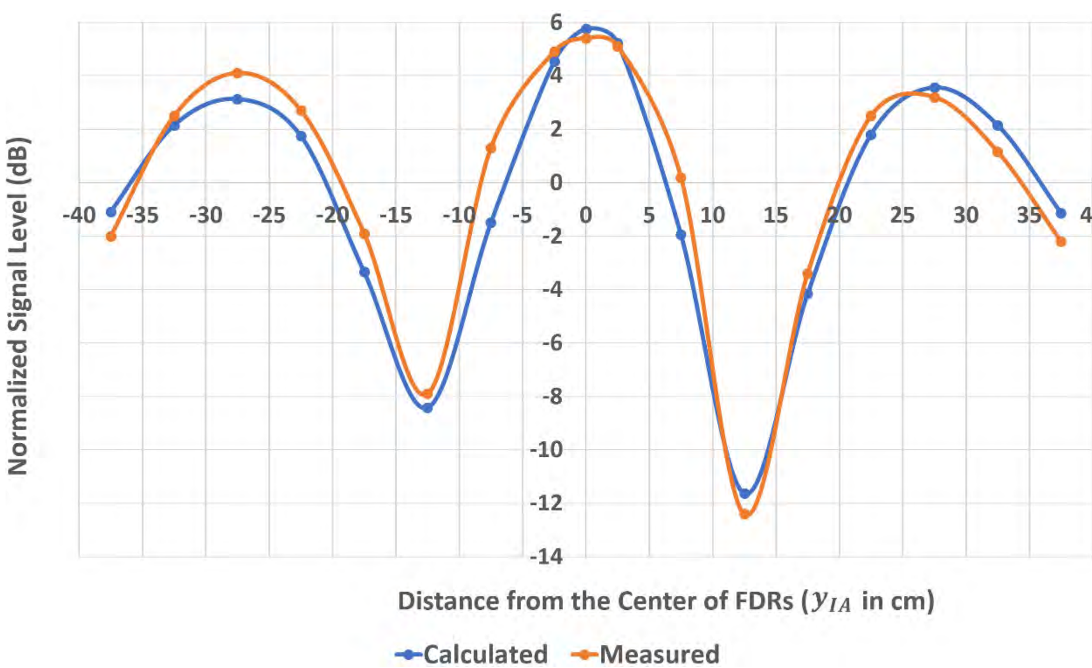

Figure 4.8 Normalized signal level vs. interrogation location.

To investigate how the separation distance between the FDRs effect the received signal level when the IA positioned at the center of the FDRs (y_{IA}=0), the measurements modeled in Fig. 4.9 are made. The signal is measured at every 10-cm from 10 cm separation distance to 100 cm. In this configuration, when they are interrogated simultaneously, the interrogation angles of FDRs are the same ($\theta_1 = \theta_2 = \theta$). So, the received signal ($P_{combined}$) can be calculated as follows:

$$P^{[dB]}_{combined}(y_{IA}) = 20\log\left(10^{(P_{FDR1}(\theta)/20)} + 10^{(P_{FDR2}(\theta)/20)}\right) \tag{4.8}$$

If the combined signal level is normalized to the single FDR signal level at the same interrogation angle (P_{FDR1} or P_{FDR2}) by using

$$[P_{combined}(y_{IA})^{[dB]}]^{N} = P_{combined}(y_{IA})^{[dB]} - P_{FDR1}(\theta)^{[dB]} \tag{4.9}$$

then nearly 6 dB gain will be observed regardless of the separation distance between FDRs. Since FDR1 and 2 responses are not completely identical and small discrepancies in the single FDR measurements are seen in Fig. 4.6, around 5 dB gain is measured in their combined signal level for all separation distances (d), as seen in Fig. 4.10. The discrepancy is also the cause of the ripple seen in this figure. The calculated results that are in very good agreement with measurements show that we are able to accurately predict the signal variation excluding the 10 cm separation case,

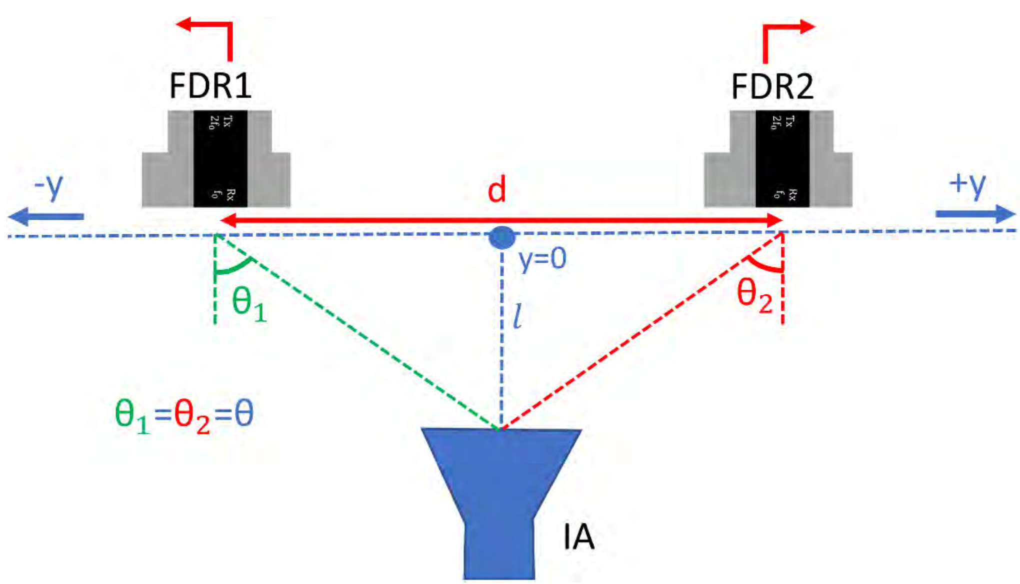

Figure 4.9 Localization measurement with two FDRs.

which is attributed to the coupling between the FDRs due to being very close to each other.

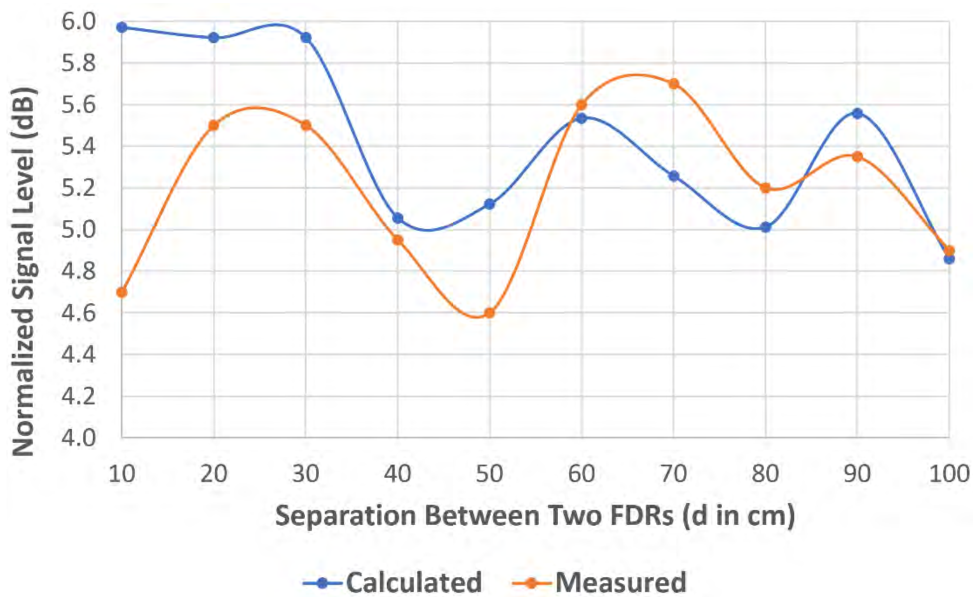

Figure 4.10 Measured vs. calculated normalized signal level vs. separation distance (d)

4.5. Displacement Measurements with Two FDRs

The displacement measurements can be accomplished with mainly three different scenarios employing a pair of FDR sensors. The first scenario is realized with two FDRs, one anchored (immobile) at the center and one moving on the y-axis, as seen in Fig. 4.11. The path length difference between two signals from FDR1 and 2 due to the interrogation angle differences results in amplitude and phase differences in received signals. In this configuration, θ_1 is always 0 while θ_2 changes with the separation distance between the FDRs (d). The amplitude differences are mentioned in the Section 4.3, and the phase differences and normalized received power can be calculated by using the formula 4.3, 4.5 and 4.7 explained in the Section 4.4.

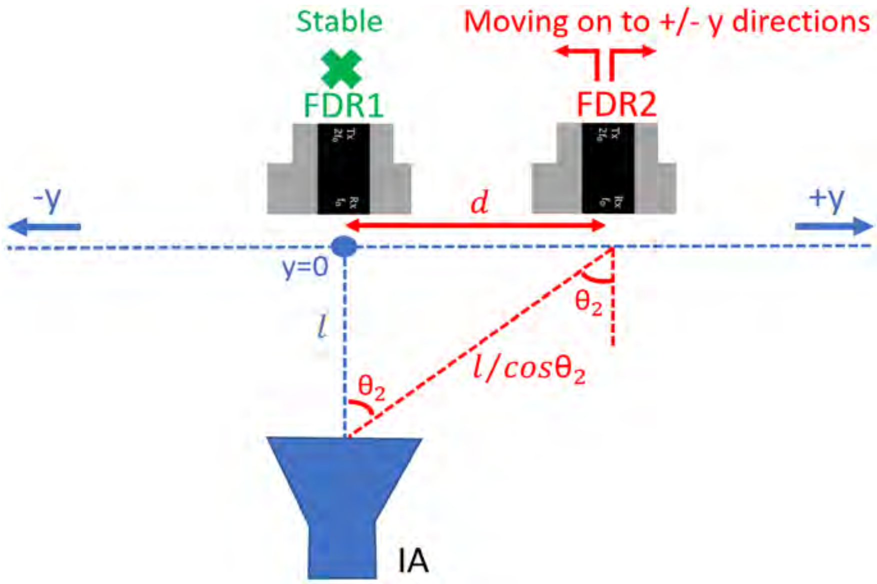

Figure 4.11 Displacement measurements setup with two FDRs – one immobile at the center and one moving on the y-axis.

Table 4.2 shows the parameters given in Fig. 4.11 and how the phase changes based on the separation distance (d). When d=25 and 45 cm, the signals become nearly out-of-phase, and when d=0 and 35 cm, they are in-phase.

Table 4.2 Calculated phase differences between two FDRs based on separation distance (or interrogation angle).

d (cm)	θ (deg)	l (cm)	l / $\cos\theta_2$ (cm)	Δφ (deg)
50 or -50	33	76.2	91.1	635
45 or -45	31	76.2	88.5	522
40 or -40	28	76.2	86.1	419
35 or -35	25	76.2	83.9	325
30 or -30	21	76.2	81.9	242
25 or -25	18	76.2	80.2	170
20 or -20	15	76.2	78.8	110
15 or -15	11	76.2	77.7	62
10 or -10	7	76.2	76.9	28
5 or -5	4	76.2	76.4	7
0	0	76.2	76.2	0

The calculated results are in very good agreement with the measurements, as seen in Fig. 4.12. The small discrepancy at y=+/- 5 cm is attributed to the coupling between the antennas since they are very close to each other at this location. Additionally, since it is not possible to place two antennas at the same location, y=0 data is missing in the measurements. But, if that would be possible and there is no coupling between the antennas (as an ideal case), the maximum signal level would be received at y=0 with a gain of 6 dB as seen in the dotted calculated data. The received signal oscillates with the physical distance (or the interrogation angle θ) due to the phase differences. Two peaks and nulls are observed in Fig. 4.12 at the locations where both signals are in-phase and out-of-phase, on either side of the center. The level differences between the peaks and nulls diminish as the separation distance increases because the signal strength of FDR2 reduces as it moves away from the center, and so has less impact on the combined signal level. From this data, it is evident that the displacement of FDR2 relative to FDR1 can be predicted based on the returned signal level.

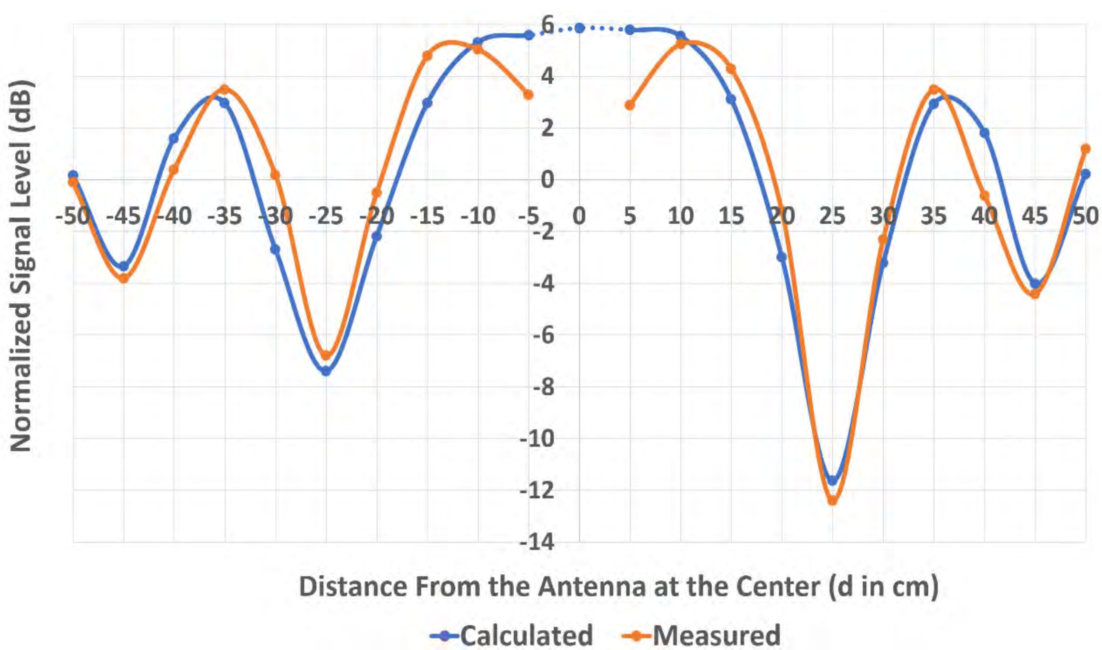

Figure 4.12 Displacement measurement results with two FDRs – one immobile at the center and one moving on the y-axis.

A second form is displacement measurement could be performed using a similar approach as the localization method described in Section 4.4. If the distance between the two FDRs is not fixed, and the interrogator is moved along the axis joining the two sensors, the response will vary depending on the FDR separation distance. The model in Fig. 4.7 represents this scenario, and FDR1 and 2 receive signals from the interrogator at angles of θ_1 and θ_2. These angles are dependent on the position of the interrogator on the y-axis. Fig. 4.8 shows the variation in the received signal based on the interrogator location when the FDRs separation distance (d) is 25 cm. The peak is observed when both FDRs are interrogated from the center (y=0), where $\theta_1 = \theta_2 = \theta$ so returned signals are in-phase. As it moves off the center, the first null is observed at around y_{IA}=12.5 cm. At this location, the IA is located right across an FDR that is 25 cm away from the other FDR, which replicates the first scenario where the null is seen in Fig. 4.12.

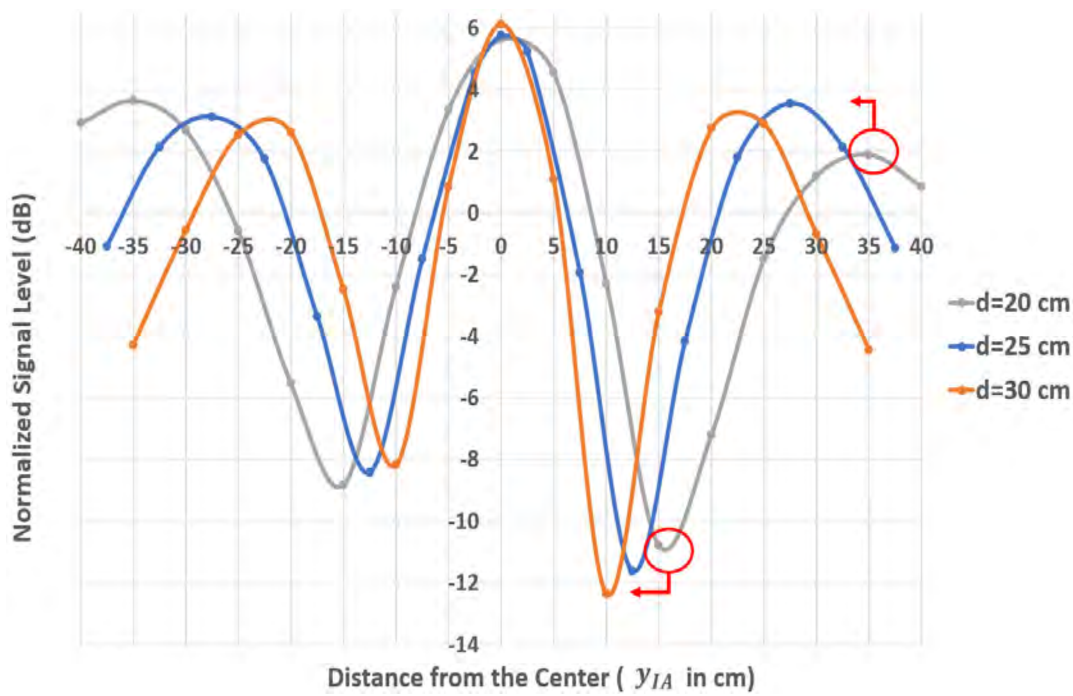

Figure 4.13 The effect of separation distance on received power vs. interrogation location.

The location of the peaks and nulls is determined by the separation distance (d), as seen in Fig. 4.13. The higher the distance causes more rapid phase change which results in a sharper transition from the peak to null and null to peak. For example, the first nulls and the second peaks occur at y_{IA}=16, 12.5, and 10 cm and at y_{IA}=22, 28, and 35 cm for the separation distances 20, 25, and 30 cm, respectively. Therefore, by interrogating the two FDR nodes at two incidence angles, the location of the nulls can be predicted with a high degree of accuracy, and this allows the separation distance (or displacement) to be determined.

A third form of displacement measurements is realized with two FDRs, a non-fixed FDR2 sensor positioned at the reverse orientation (flipped) compared to an anchored (fixed) sensor FDR1 as modeled in Fig. 4.14. Since the sensor antenna feed points are in opposite directions with this configuration, they will receive signals with 180^{o} phase difference. Therefore, interrogating the FDRs from the center will result in complete field cancellation, and a null will be observed as oppose to a peak seen in the previous configuration. When the interrogator moves off the center, the fields will become in-phase, and a peak will be observed at the same location where a null is observed in the previous configuration. Fig. 4.15 compares simulated and measured signal level with this configuration. When the separation distance closes to 0, a high level of null (~-15 dB) is measured, and the first peak is measured in the order of 5 dB when they are separated 25 cm. Compared to the behavior in Fig. 4.12, this arrangement may provide higher resolution displacement measurements when the sensors are close to one another given the high rate of change in the signal level for small displacements.

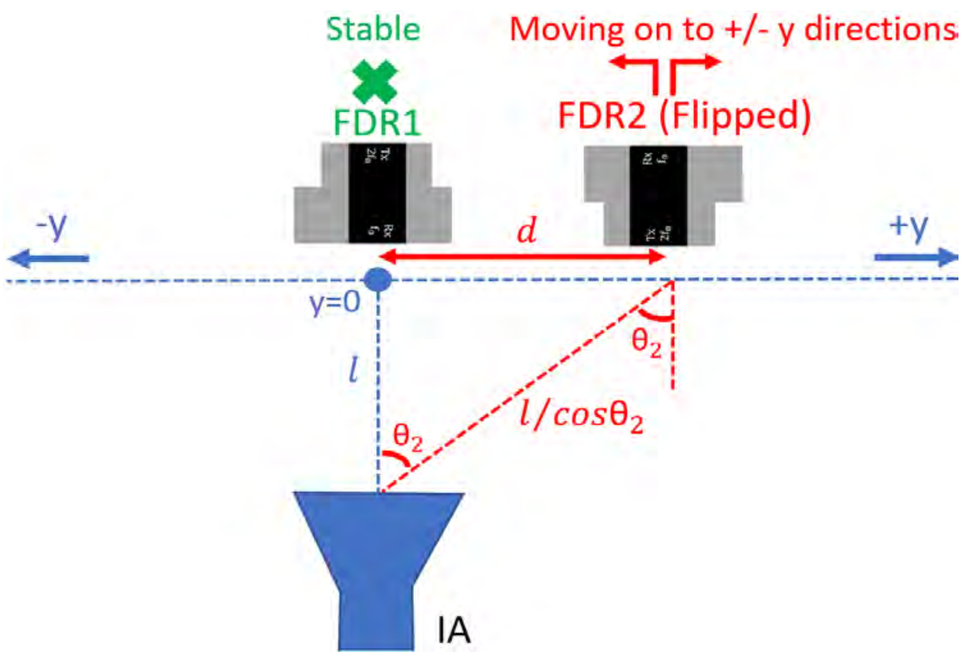

Figure 4.14 Displacement measurements setup with two FDRs – one immobile at the center and the other flipped vertically and moving on the y-axis.

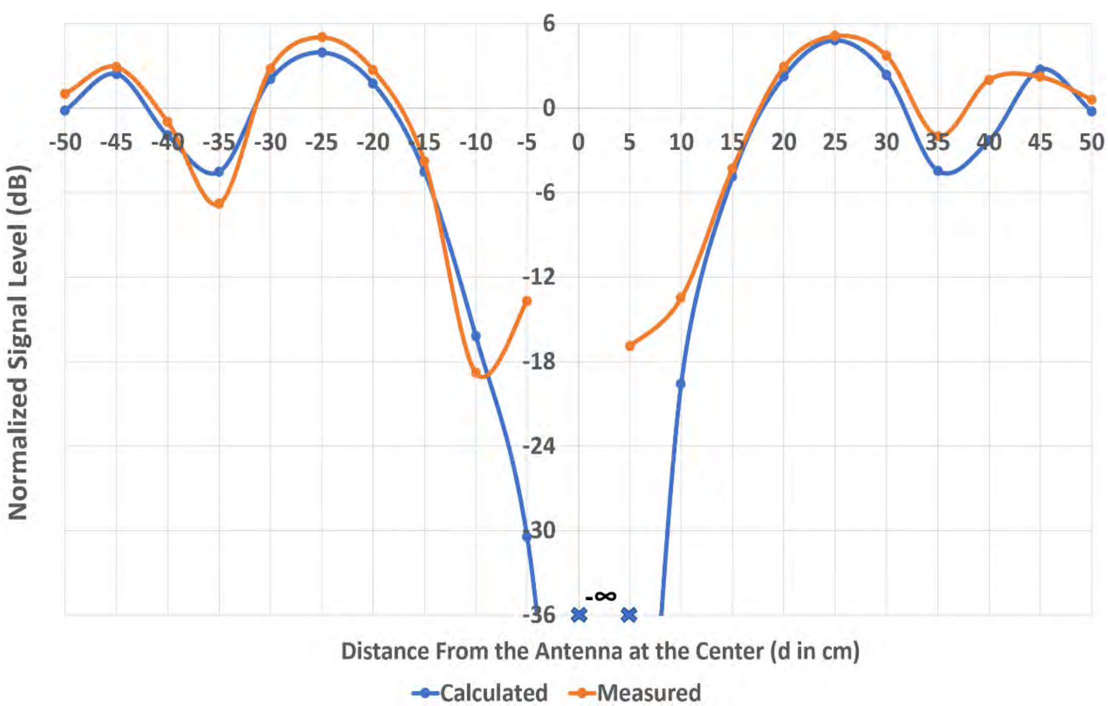

Figure 4.15 Measured vs. Calculated displacement with two FDRs – one immobile at the center and the other flipped vertically and moving on the y-axis.

4.6. Conclusions

A novel interferometric approach to measure the displacement and localization with a pair of FDR sensors excited by an interrogator is presented. Based on the interrogation angle, phase differences between the signals from the sensors occur, and the returned signal magnitude varies due to constructive/deconstructive interference. The location and displacement information are extracted from the peaks and nulls locations. As the distance between the sensors are increasing, a sharper transition is observed from peak to null.

The displacement can be done while the pair of FDR sensors are in the same or opposite orientations. When they are in the same orientation, a peak and a null are seen at the center and out of the center respectively in contrast with the opposite orientation which shows a null at the center. Both cases show nearly 20 dB level differences between the first peak and null, which helps significantly to distinguish the FDR positions.

All the measured signal levels are verified with the calculations with a very good agreement excluding when the sensors are very close (+/- 5cm or $0.2\lambda_0$) to each other. Due to the close proximity between the sensors, mutual coupling occurs at these locations.

The measurements made in free-space have demonstrated great potential of proposed displacement and localization sensing technique to be used in real environment. These initial tests are made in controlled environment, and several assumptions have been made. For example, the distance between IA and the FDRs or the sensor orientations are known. When these sensors are embedded in the real environment, the positions, distances or the orientations may be altered. Additionally, the radiation pattern, the impedance, and the resonant frequency of the antennas may change based on the surrounding environment conditions.

Chapter V :

An X-Band Dielectric Rod Antenna for Subdermal Tumor Heating to Assist Electroporation-Mediated DNA Delivery

5.1. Introduction

Gene therapy is not yet a practical reality, but significant progress has recently been made due to research and development efforts that began more than 20 years ago. The primary component of any gene therapy is, of course, a sequence of deoxyribonucleic acid (DNA) that encodes a therapeutic molecule. A delivery method is required in all cases to help the large and highly charged DNA sequence to traverse the cell membrane to reach its intracellular site of action. Cells must then remain alive to process the delivered therapeutic DNA (by processes known as transcription and translation) to produce the encoded therapeutic molecule that can then exert its biological effect. Physical, viral, and chemical methods have been employed for DNA delivery in both preclinical and clinical studies. One delivery method that has shown promise is known as electroporation. It has been accepted as having clinical importance based upon approximately 100 clinical trials that are in various stages of completion (www.clinicaltrials.gov). The majority of the trials have been initiated in the past 10 years following the first [52]. These trials were preceded by initial animal studies [53], [54] in the 1990s that lead to an exponential rise in the number of publications in this field. The method employs locally applied direct current (DC) pulses, using electrodes inserted into tissue or resting on the surface, to temporarily weaken the barrier properties of cell membranes. This ultimately initiates/mediates the entry of exogenous DNA into cells [55]. The method has been used in many tissue types because it is physical in nature and can be tuned to any particular tissue by changing the characteristics of the applied DC pulses. It has been used to treat both normal tissues and many types of tumors [56], [57].

Recent in vivo studies in Guinea pig skin used heat to augment the electroporation process. DNA was first injected into the skin, infrared radiation was applied to heat the skin to 43 °C, and then DC pulses were applied to electroporatively deliver DNA into the cells that comprised the skin [27], [58]. This method resulted in an 8–fold increase in expressed DNA relative to electroporation without heating the tissue. Essentially, this means that roughly an order of magnitude increase in therapeutic molecules may be expected by moderate heating. Furthermore, these same studies demonstrated that the magnitude (voltage) of the applied pulses could be reduced by about 50% when the tissue was heated to achieve that same level of DNA expression. These results were obtained in the skin, which is superficial and on the order 1 mm thick. Infrared light was a good energy source for heating because its penetration depth was limited. However, many potential applications for electroporation are for the treatment of solid tumors of many varieties. These are generally embedded deeper within tissues, and because of that, heating with infrared light is not a practical method due to its lack of penetration depth. However, microwave energy can be used to heat deeper tissues. Thus, this study focused on developing a heat source that could be used in tumors and ultimately integrated with arrays of electrodes that are used to apply electroporation pulses to deliver DNA. The combined device could then be used to develop specific tumor treatment protocols. Such a device will have broad utility to investigate the combined use of heat and electroporation-based DNA delivery because many animal models of specific tumors (such as melanoma, breast liver, etc.) can be established with subcutaneous tumors.

Microwave energy has in fact been used to heat tumors for many years. As a stand-alone therapy, the aim of heating a tumor is to kill tumor cells as a result of heating to temperatures that are about 42-44 °C for times that are on the order of 30 – 60 minutes [59]. Often, microwave heating is used in combination with chemotherapy; the heating component is thought to increase the ability of chemotherapeutic agents to traverse the cell membrane to increase efficacy.

Naturally, the design of the device used to apply the microwave energy – in this case, a microwave antenna – must meet the functional requirements for the application. From a translational perspective, it is important to focus the energy on the tumor, with minimal energy dissipated in surrounding healthy tissues. This requirement relates to the expected size and location of the tumor in the body. Heating time is another parameter that must be considered to make the applicator practical. With regard to these requirements, the operating frequency, directionality of the applicator, impedance matching between the applicator and human body tissues, and the applied input power level all have a significant impact.

A variety of different microwave applicators have been designed and employed for subdermal heat treatment, with trade-offs on the factors mentioned above. For example, open-ended waveguide [28], microstrip patch [29], loop [30], dielectric lens [31], and horn antennas [32] have all been studied. These applicators were designed to treat relatively large tumors that are located farther beneath the surface of the skin than those of interest in this work. Hence, the applicators operate at lower frequencies (915 or 2450 MHz) with relatively low directionality. In contrast, the proposed dielectric rod antenna (DRA) used in this work concentrates the microwave energy into the confined tumor location that is between 3-7 mm below the skin surface, resulting in a high specific absorption rate (SAR) in the region. As a result, only 2.5 W of RF input power and a 4-minute application period are needed to heat the tumor region to the desired temperature.

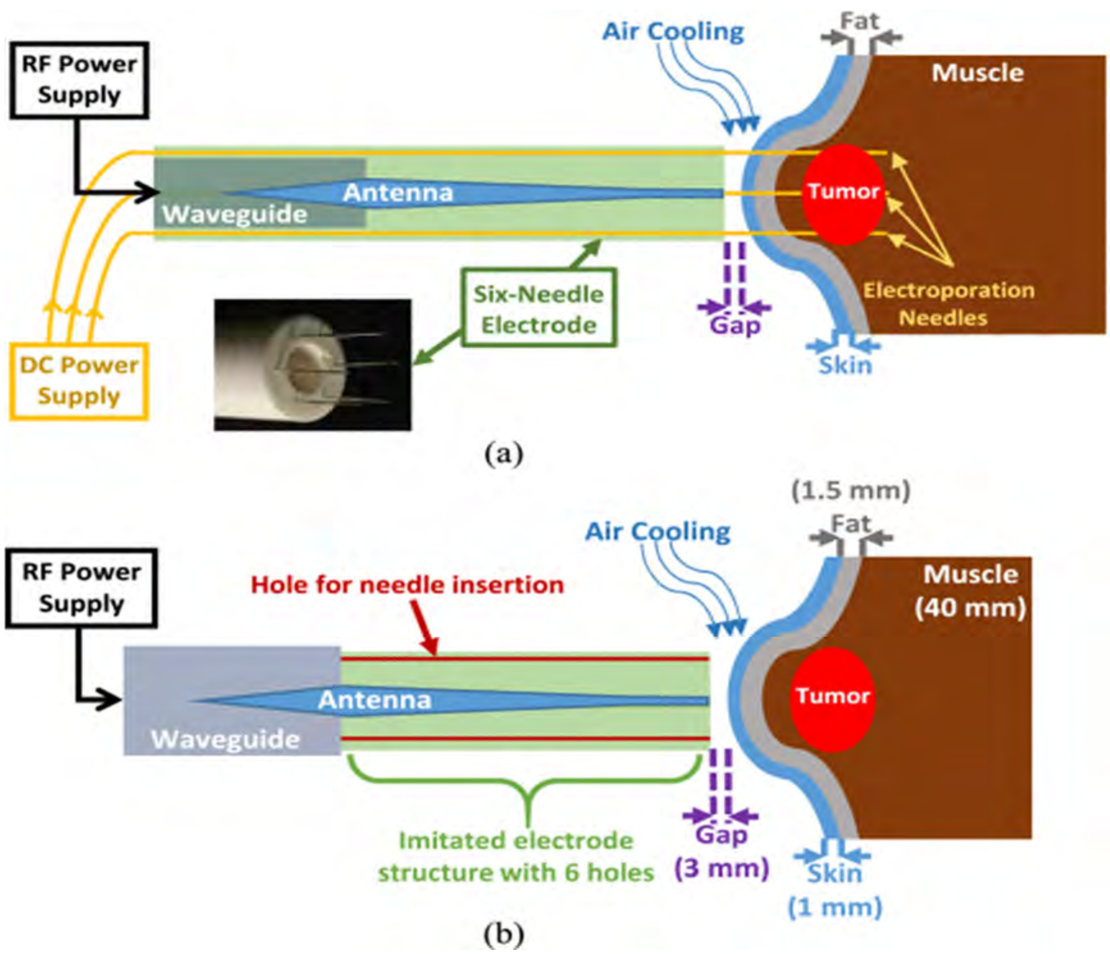

Figure 5.1 (a) Possible future implementation including needles for electroporation and photo of six-needle electrode and (b) experimental model of the microwave heating system and location of the target tumor in the human body.

An end-fire dielectric rod antenna is proposed as a microwave heating device for integration with an array of electroporation electrodes in order to enable efficient delivery of DNA into the cells that comprise subcutaneous tumors. Fig. 5.1 illustrates the proposed model of the microwave heating system and the location of the target tumor in the human body. In practice, microwave heating will be performed, followed by the application of DC pulses to weaken the cell membrane. The DC pulses will be delivered by an array of electrodes, such as the six-needle array around the circumference of the DRA shown in Fig. 5.1(a). The electrode array will be drawn back away from the tissue during the microwave heating phase since a high concentration of microwave electromagnetic field – and thus a high amount of heating – occurs at the needle locations if they are present in the treatment area. Accordingly, the simplified applicator model in Fig. 5.1(b), which includes the holes for the needle locations, is used in this work.

A 5-7 °C temperature elevation of tumors that are located near the fat-muscle boundary and 3-7 mm below the skin surface can be achieved in a short period of time without damaging surrounding tissues. This capability is demonstrated through a combination of a directional antenna applicator operating at 8 GHz, and utilization of forced air cooling of the outer surface (skin layer). The directionality of the antenna is improved by cladding its high permittivity core with 3D printed, low permittivity dielectric material. Experimental data using a pork skin-fat-muscle tissue show that the desired temperature elevation at the tumor location is obtained after 2.5 W RF illumination for 3 minutes, which is in good agreement with electro-thermal simulations. With the addition of realistic human body model parameters to the same simulation setup, the results indicate that tumors can be uniformly heated with 3 minutes of illumination at 2.5 W input power while keeping the surrounding healthy tissues at a safe temperature.

In the first part of this chapter, the design, fabrication, and characterization of the proposed antenna and the dielectric characterization of tri-layer (skin, fat, muscle) pork tissues are explained. The second part of it describes simulated and experimental results and thermal analysis on these well-characterized tri-layer pork tissue (TPT). The simulated performance of the applicator with a realistic human body model (HBM) is given in part three. And it ends with conclusions.

5.2. Microwave Heating System Design and Methodology

5.2.1. Design of the Microwave Heating Applicator

The dielectric rod antenna (DRA) used as the microwave applicator is illustrated in Fig. 5.2. The high permittivity core material of the antenna is made of Rogers 3010 ($\varepsilon_r = 10.2$ and $\tan\delta = 0.0035$) and consists of three sections: the feed taper, the body gradient, and the constant height sections. In this design, the 30 mm long feed taper (L1) is placed inside an X-band rectangular waveguide feed and used for impedance matching between the waveguide and the dielectric rod. In the 76 mm long body gradient section (L2), radiation from the surface of the dielectric rod occurs and combines with the radiation from the waveguide aperture. The 4.3 mm long constant height section (L3) is used to achieve the proper phase alignment between the aperture-emitted and surface wave fields in order to maximize the directionality of the antenna. The body gradient section can also help to reduce the sidelobe level, as described in [60]. The total length of the antenna plays a key role in determining the half-power beam width.

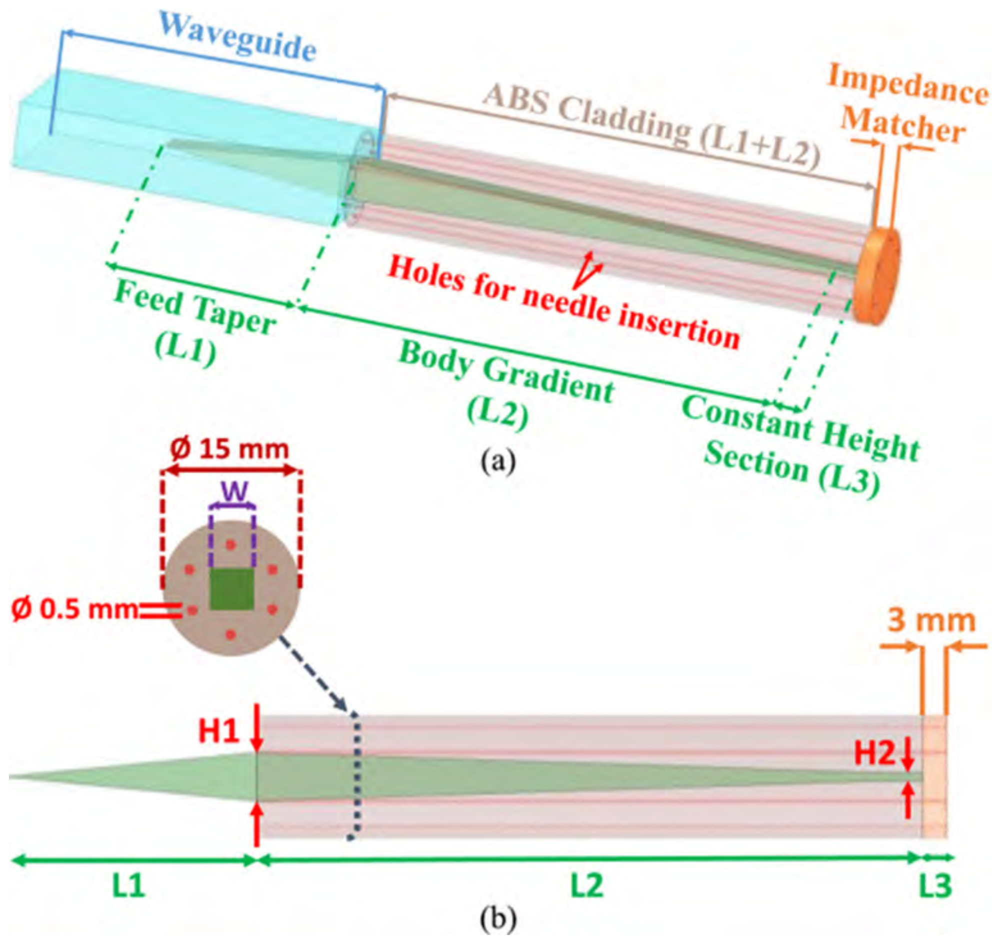

Figure 5.2 Proposed dielectric rod antenna microwave applicator a) isometric view, b) front view.

In addition to determining the fundamental antenna dimensions, the process used here includes the design of a cladding layer and an impedance-matching layer, along with final optimization using numerical electromagnetic simulations. The antenna is encased by a 3D printed acrylonitrile butadiene styrene (ABS) plastic in 15 mm diameter to increase the antenna directivity and reduce sidelobe radiation in addition to imitating the electrode probe shown in Fig. 5.1(a). Cladding the core with this low permittivity material ($\varepsilon_r = 2.6$ and $\tan\delta = 0.003$) provides a convenient way to achieve high directionality without increasing the total length of the antenna. The reflection coefficient at the antenna input port is improved with the addition of the 3 mm thick impedance matching layer that is positioned between the antenna and HBM. The thickness and dielectric constant of the matching layer are determined by treating it as a quarter-wavelength impedance transformer that is terminated by the HBM, assuming the skin, fat, and muscle layers are of 1-, 1.5-, and 40-mm thicknesses; this design approach was validated with full-wave numerical electromagnetic simulations using Ansys HFSS version 19.2. In this case, the material selected for the matching layer is the same as that used for the DRA core. The design parameters were optimized to obtain the best end-fire performance, taking into account the impact of the holes for the 6-needle electrode array and the polyester layer that encapsulates the array. By using the optimization tool, in addition to given L1, L2, and L3 parameters, the optimum width (W) and heights (H1 and H2) were found to be 4.6, 5.9, and 1 mm, respectively. Based on these parameters, the antenna core was cut precisely by using a LPKF MicroLine 2820p laser cutter.

5.2.2. Characterization of Human Body Mimicking Phantoms

The experimental validation of the microwave applicator was conducted using the stacked, tri-layer (skin, fat, muscle) composite human body phantom shown in Fig. 5.3. A phantom is used in this work since the electrical and thermal properties of the materials can be readily characterized using a commercially-available dielectric probe and a steady-state ASTM D5470 Fourier's Law extrapolation technique, making a rigorous comparison to electro-thermal simulation results possible. Among the several phantom recipes that are available in the literature, those described in [61] were selected for this work since they provide the desired dielectric properties through the 7-9 GHz frequency range. The phantoms are comprised of the following non-toxic

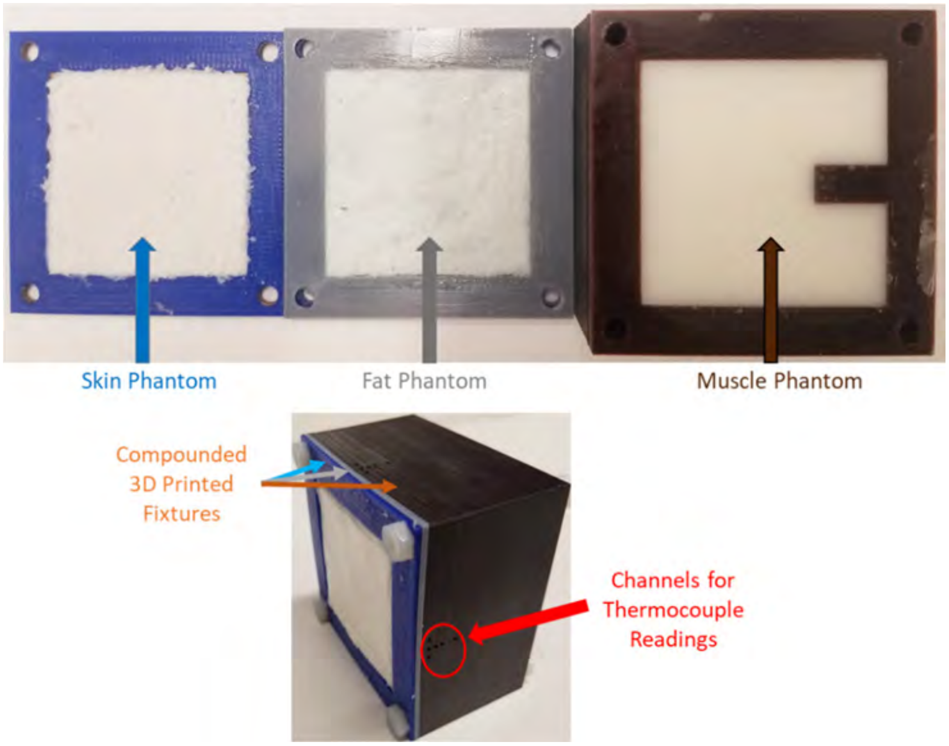

Figure 5.3 3D printed test fixture and human body mimicking tissue phantoms.

materials: de-ionized water, gelatin, salt, vegetable oil, and dishwasher detergent. Compared to the previously published recipes, a modification of the detergent and oil concentrations was found to be necessary to fine-tune the dielectric properties; these differences might be the result of using different brands of these items compared to those used in [61]. Increasing the oil concentration and decreasing the detergent proportion in the mixture decreases the dielectric constant and increases the loss tangent. Table 5.1 shows the ingredients of the fabricated tissue phantoms. Skin and muscle phantoms are made with “Ultra Ivory” brand liquid dishwasher detergent (εr=46.22 and $\tan\delta$=0.62). But, “Dawn Ultra” brand detergent is used for the fat phantom since its dielectric constant and loss tangent values are the lowest comparing with the other available ones in the market (εr=27.1 and $\tan\delta$=0.53). Additionally, water and oil refer to de-ionized water and pure vegetable oil, respectively.

Table 5.1 Ingredients of the Tissue-Mimicking Phantoms [61]

Phantom Name	Water (g)	Gelatin (g)	NaCl (g)	Oil (g)	Detergent (g)
Skin	35	4	0.12	10.33	6.67
Fat	14.35	2	0	82.4	2.5
Muscle	105	12	0.25	13.67	20

The dielectric properties of these phantoms are measured with an Agilent 85070E open-ended high-temperature dielectric probe, and the results are given in Fig. 5.4. The phantom properties have a close agreement with corresponding human tissue dielectric properties given in [62].

One of the important thermal characteristics of these phantoms was their melting temperature of 35 ºC. This allowed up to a 15 ºC temperature elevation to be

Table 5.2 Measured Tissue Phantom Thermal Properties Compared with Human Tissues [63,64,65]

Tissue Name	Thermal Conductivity (W/mK)	Heat Capacity (J/kg K)	Density (kg/m^3)
Skin	0.37	3391	1109
Skin Phantom	5.5	3400	1100
Fat	0.21	2348	911
Fat Phantom	4.5	2100	950
Muscle	0.42	3421	1090
Muscle Phantom	6	3600	1200

observed, assuming an ambient room temperature of 20 ºC. At and beyond the melting temperature, the dielectric and thermal properties of the TPs are significantly altered. Therefore, it is not possible to make any measurements with these phantoms at the human body temperature levels. Additionally, the high discrepancy in thermal conductivity values, shown in Table 5.2, between human body tissues and the phantoms prevented us from making good thermal comparisons. Therefore, pork tissues, which have a similar dielectric and thermal conductivity to human tissues and do not alter human body temperature, were preferred to use in antenna testing.

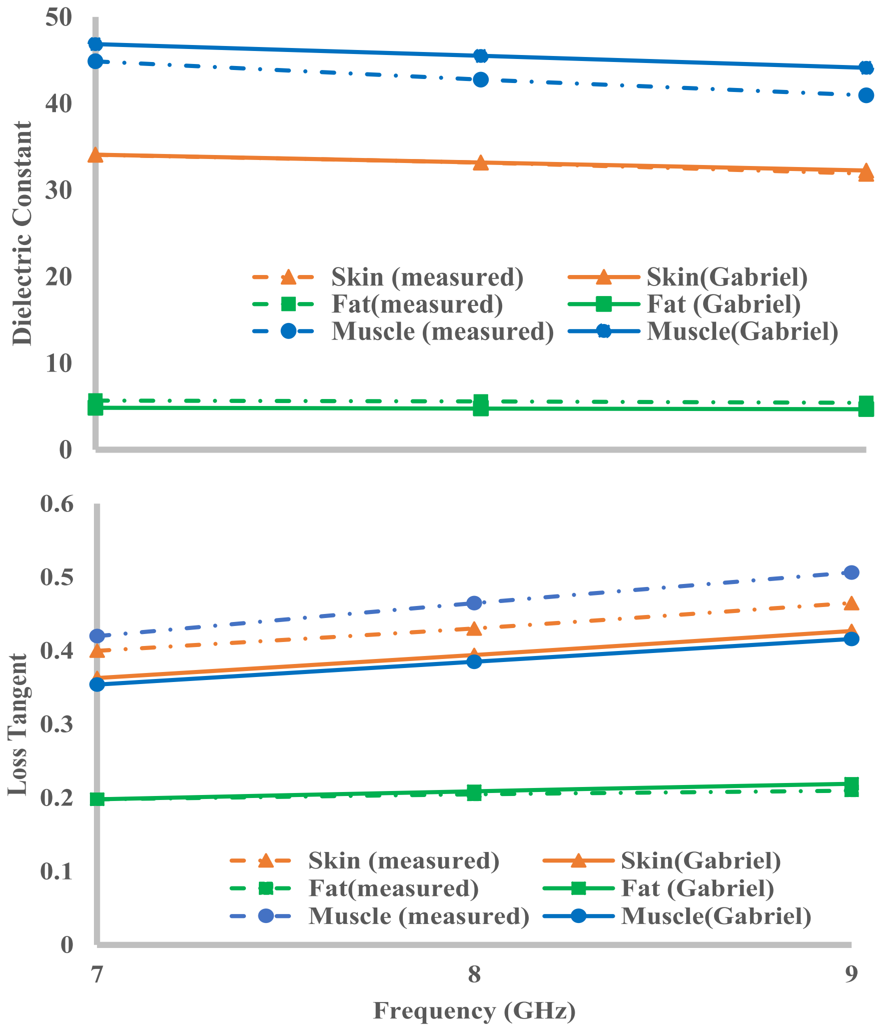

Figure 5.4 Comparison of measured (a) dielectric constant and (b) loss tangent of skin, fat and muscle tissue phantoms compared with data from [62].

5.2.3. Characterization of Pork Tissues

The experimental validation of the microwave applicator was conducted using the stacked TPT, shown in Fig. 5.5. The pork tissues are used in this work since they have biological similarities to the human body [66], and their electrical properties can be characterized using a commercially-available dielectric probe, and the thermal properties can be found in the literature [63], [64], [65], making a rigorous comparison to electro-thermal simulation results possible. The dielectric properties of these pork tissues are measured at 37°C with an Agilent 85070E open-ended performance dielectric probe.

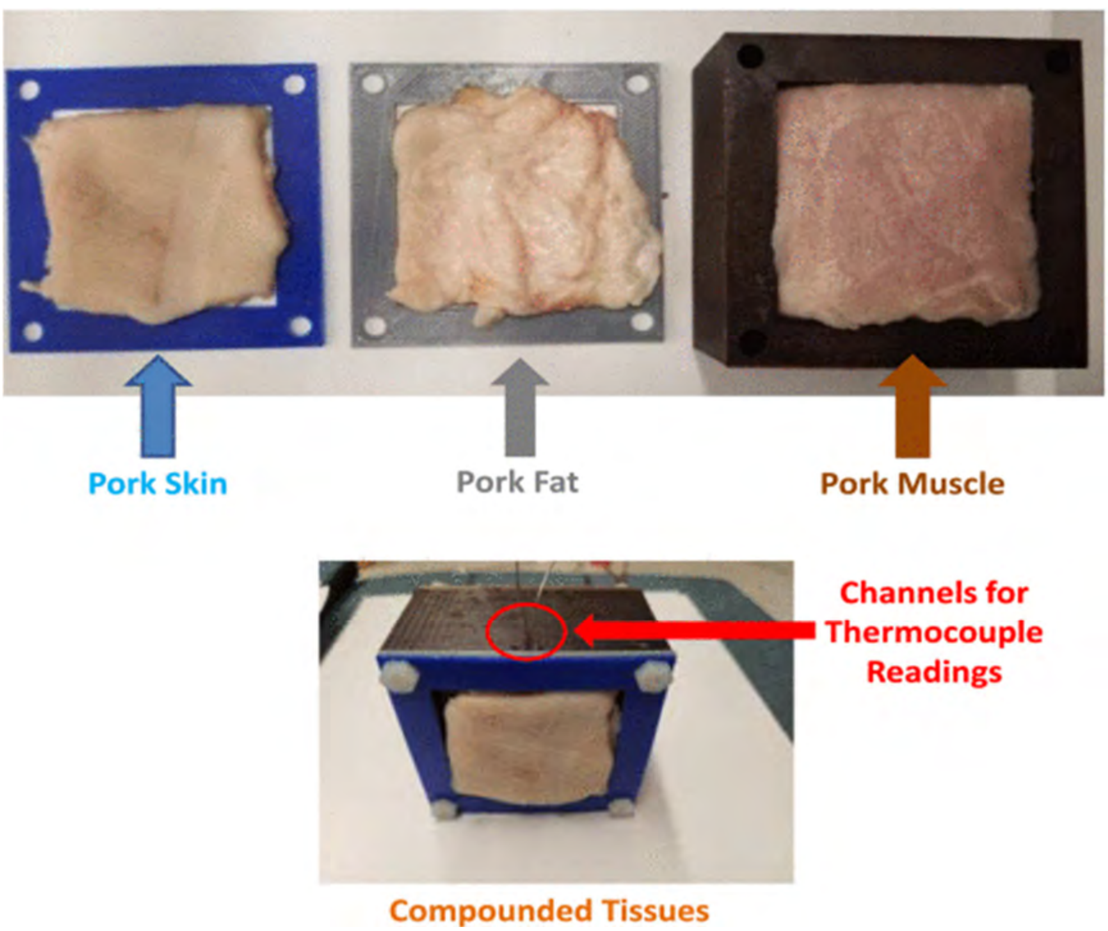

Figure 5.5 3D printed test fixture and compounded TPT.

The data, compared with corresponding human tissue properties given in [62], is close enough to approximate the microwave absorption by human tissues. The dielectric properties shown here will be relatively stable over the temperature range of interest (37-44°C) in the TPT and HBM [67].

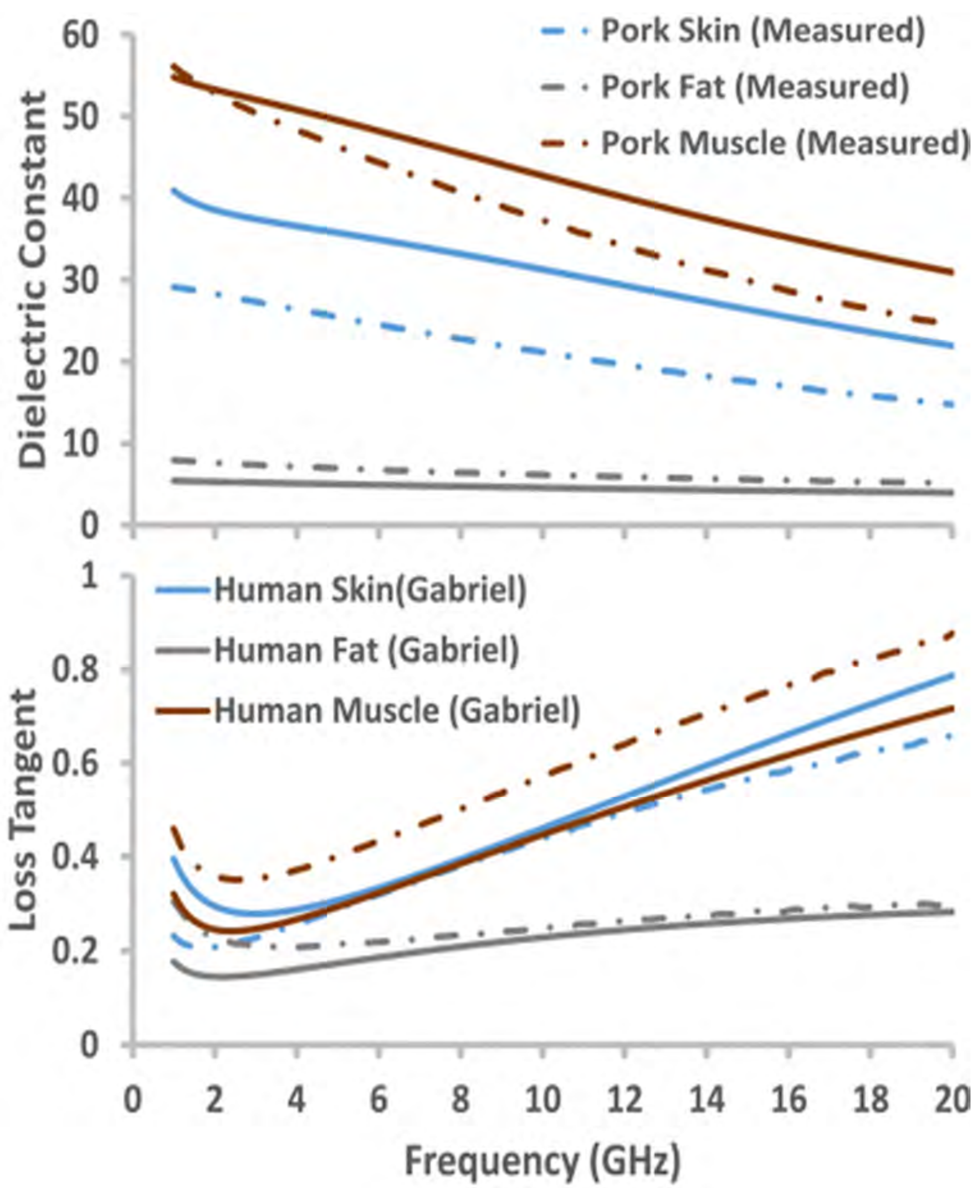

Figure 5.6 Comparison of measured dielectric constant and loss tangent of pork skin, fat, and muscle tissues compared with human tissues in [62].

5.2.4. Antenna Reflection Coefficient

The antenna reflection coefficient (S11) is useful in determining the amount of power transmitted into the HBM. Therefore, the measured and simulated reflection coefficient values in the 7-9 GHz band are discussed in this section. In Fig. 5.7, the measured antenna reflection coefficient (S11) data are compared with the simulated data from Ansys HFSS, with the antenna terminated with the TPT. The graph also includes the simulated data obtained with the antenna terminated with the HBM. The measurements were performed using an Agilent N5227A PNA Microwave Network Analyzer. Measurement uncertainty was determined from four independent data sets using separate calibrations. These data indicate that more than 95% of the available source power can be transmitted at 7 and 8 GHz, and more than 91% is transmitted at 8.7 GHz. The S11 measurement uncertainty at 8 GHz is in the range of 0.3 dB, which

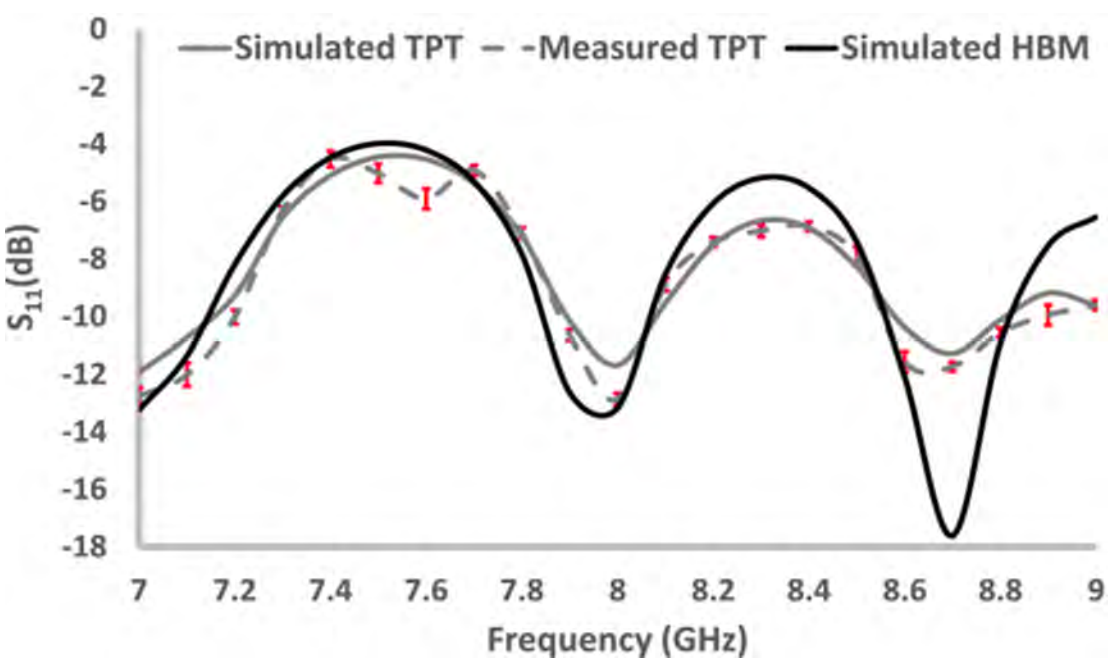

Figure 5.7 Simulated and measured reflection coefficient (S11) of the proposed antenna applicator terminated with TPT and simulated results using a human body model (HBM) in place of the TPT. Errors bars represent S11 measurement uncertainty.

corresponds to 0.4% uncertainty in transmitted power. Additionally, the -10 dB bandwidth around these frequencies is nearly 200 MHz. The reflection coefficient across the entire band can be improved by reducing the gap between the antenna and TPT or HBM; however, the 3 mm air gap allows for surface cooling to limit the temperature rise of the skin and fat layers.

5.3. Simulation and Measurement of Temperature Distribution in the TPT

The temperature change induced in the TPT by the microwave applicator was simulated and measured using the apparatus shown in Fig. 5.1(b). The thicknesses of skin, fat, and muscle tissues were chosen as 1, 1.5, and 40 mm, respectively. The tumor is presumed to have a 4 mm height, and 7.5 mm diameter, and to be located 3 mm deep inside the TPT. Since the dielectric properties of a tumor at 8 GHz can be very similar to those of muscle (e.g., $\varepsilon_r = 44$ and $\tan \delta = 0.4$ according to [68]) a distinct region of

Table 5.3 Measured Pork Tissues Thermal Properties Compared With Human Tissues [63,64,65]

Tissue Name	Thermal Conductivity (W/mK)	Heat Capacity (J/kg K)	Density (kg/m^3)
Human Skin	0.37	3391	1109
Pork Skin	0.32	3300	1100
Human Fat	0.21	2348	911
Pork Fat	0.215	2170	922
Human Muscle	0.42	3421	1090
Pork Muscle	0.453	3590	1050

tumor-mimicking material was not used in TPT; rather, the tumor was assumed to be a region within the muscle layer. The specific absorption rate (SAR) distribution was simulated using Ansys HFSS 19.2 with the measured dielectric properties in Fig. 5.6 and the density parameters listed in Table 5.3.

The average SAR distribution[2] with a 2.5 W, 8 GHz input power level is characterized in Fig. 5.8. The figure shows that the fields penetrate into the muscle tissue up to 8 mm and then rapidly diminish. These outcomes demonstrate that the fields penetrate to and are concentrated within the tumor region, with low field values in areas adjacent to and beneath the tumor region. Additionally, the SAR distribution on the tumor's front surface location illustrates that the maximum absorption occurs across the 7.5 mm diameter tip of the antenna.

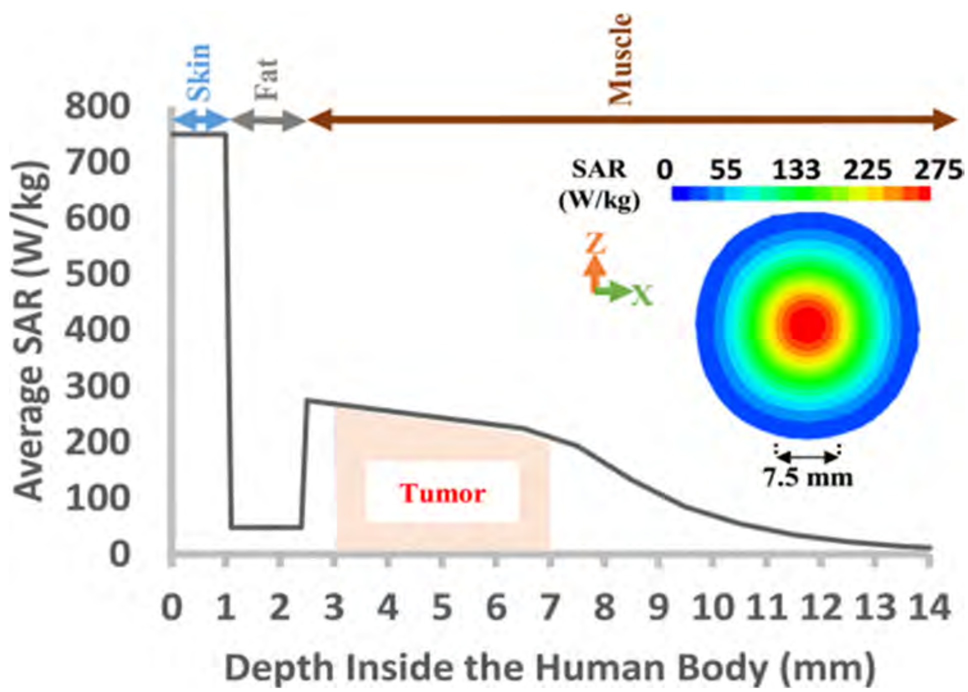

Figure 5.8 Simulated SAR value along the center of TPT and SAR distribution on the tumor's front surface location.

[2] HFSS calculates the average SAR by subdividing the model into a grid of voxels, mapping density and local SAR values over the voxel grid and applying a two-pass average SAR algorithm to the voxels. The average SAR values are then distributed back to the FEM mesh [69].

The broadband nature of the DRA applicator allows it to be operated over a range of frequencies, and, thus, to vary the depth of the heating zone. According to (5.1), the attenuation constant (αtissue) is proportional to the loss tangent ($\tan \delta$) of the tissue and operation frequency (f), and inversely proportional to the phase velocity ($c/\sqrt{\varepsilon_r}$) of the propagating wave in the tissue, where c is the speed of light and ε_r is the relative permittivity.

$$\alpha_{tissue} = \frac{\pi \cdot f \cdot \sqrt{\varepsilon_r}}{c} \tan \delta \quad (Np/m) \tag{5.1}$$

Since the penetration depth is inversely proportional to the attenuation constant, the heating zone can be moved farther into the tissue by lowering the operating frequency. For example, full-wave simulations using the TPT model predict a steep decrease in SAR at 8.8, 8, and 7 mm beneath the skin surface for frequencies of 7, 8, and 8.7 GHz, respectively.

The experimental validation of the heating efficacy of the DRA applicator was performed, as shown in Fig. 5.9, by employing multiple measurement points and a thermal control process intended to limit the heating of presumed healthy tissue regions. In order to track heating versus depth, thermocouples were positioned at 1 mm deep in the fat tissue in addition to 1 and 3 mm deep in the muscle tissue. The outer skin surface temperature was also monitored using a thermal imaging camera. To limit heating of the skin and fat layers, 5 °C air was blown at 15 m/s over the surface of the skin through the 3 mm gap between the antenna and TPT during testing. The frequency and time-dependent thermal simulations were performed in Comsol Multiphysics 5.4. While Ansys HFSS is convenient for the antenna reflection coefficient and SAR

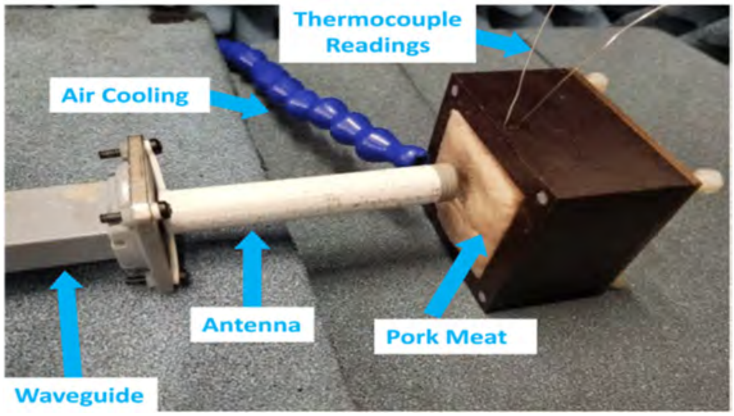

Figure 5.9 Fabricated dielectric rod antenna tested using the TPT.

simulations, the Comsol Heat Transfer module was preferred for transient thermal computations. Inputs for these simulations included the convective heat transfer coefficient of forced-air cooling, the thermal coupling effect between the tissues, and the dielectric and thermal characteristics of the tissues. In addition, biological factors such as blood flow and metabolic heat production can be specified; these are used in Section IV in conjunction with the HBM.

The transient thermal simulation and the measurements are performed using 2.5 W RF input power. The dielectric and thermal parameters given in the previous sections were used for the simulations. Fig. 5.10(a) illustrates the FLIR thermal camera picture of the skin surface after 240 seconds of RF illumination, along with the simulated temperature distribution; the peak measured and simulated temperatures are 32.6 °C and 32.4 °C, respectively. The graphs in Fig. 5.10(b) show that the simulated and measured temperature elevations at different locations in TPT are in close agreement. In the linear regions, the temperature elevation is on the order of 4.5 °C/minute at 1 mm deep in the muscle layer and drops to 3.9 °C/minute at the deepest tumor location. The slope in the linear regions is directly proportional to the input RF power level and convective heat transfer coefficient of the cold air. Fig. 5.10(c) shows the temperature

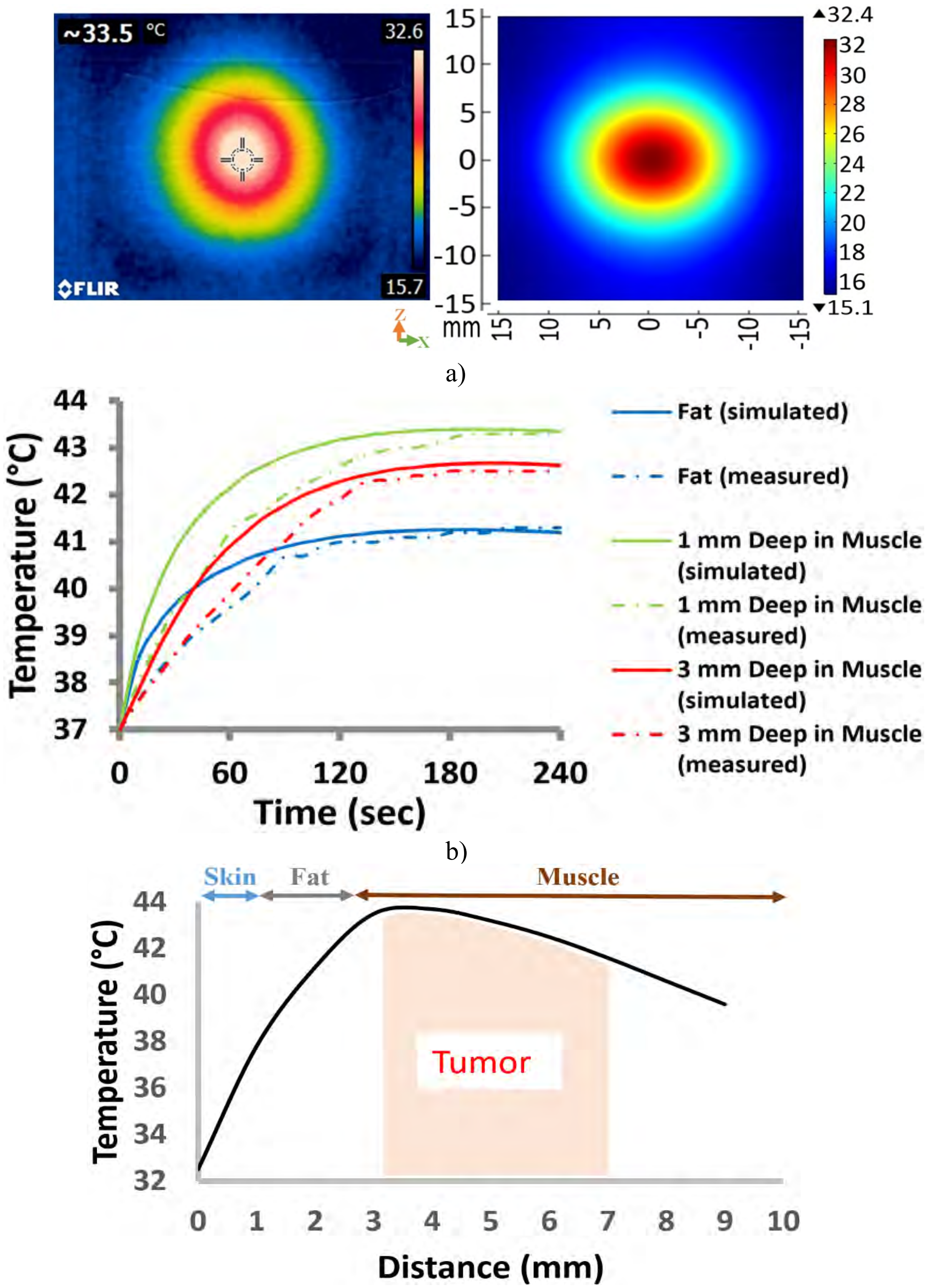

Figure 5.10 (a) Measured and simulated temperature distribution on the skin surface after 240 seconds of RF illumination. (b) Measured and simulated temperature change versus time at the center location of 1 mm deep in fat tissue, 1 mm and 3 mm inside muscle tissue. (c) Temperature variations in all tissues after 4 minutes testing.

variation inside the TPT versus depth after 4 minutes of heating. The desired temperature elevation is achieved in the tumor location while the maximum temperature in the skin and fat layers is lower than 42 °C.

5.4. Temperature Distribution Analysis on a Realistic Human Body Model

In addition to the TPT, the performance of the microwave heating system has been simulated using an electrically- and thermally-realistic HBM in Comsol. This model includes biological factors, such as blood flow and metabolic heat production, and their impact on the temperature elevation in the tissue layers. The simulation uses the Pennes' bio-heat equation expressed by

$$\rho \cdot c \cdot \frac{dT}{dt} - \nabla \cdot (k \nabla T) = B_0 \cdot \left(T_b - T\right) + \rho \cdot SAR + A_0 \tag{5.2}$$

where ρ, c, and k are the density, specific heat, and thermal conductivity of the tissue; B_0, A_0, and T_b are the heat exchange mechanism due to capillary blood perfusion, metabolic heat production and blood temperature (37 °C) [70]. ρ, c, and k parameters of the tissues are given in Table 5.3, and the remaining parameters are listed in Table 5.4.

Table 5.4 Biological Parameters in Pennes' Bio-Heat Equation [71]

Tissue Name	A_0 (W/m^3)	B_0 (W/m^3 °C)
Skin	1620	9100
Fat	300	1700
Muscle	480	2700

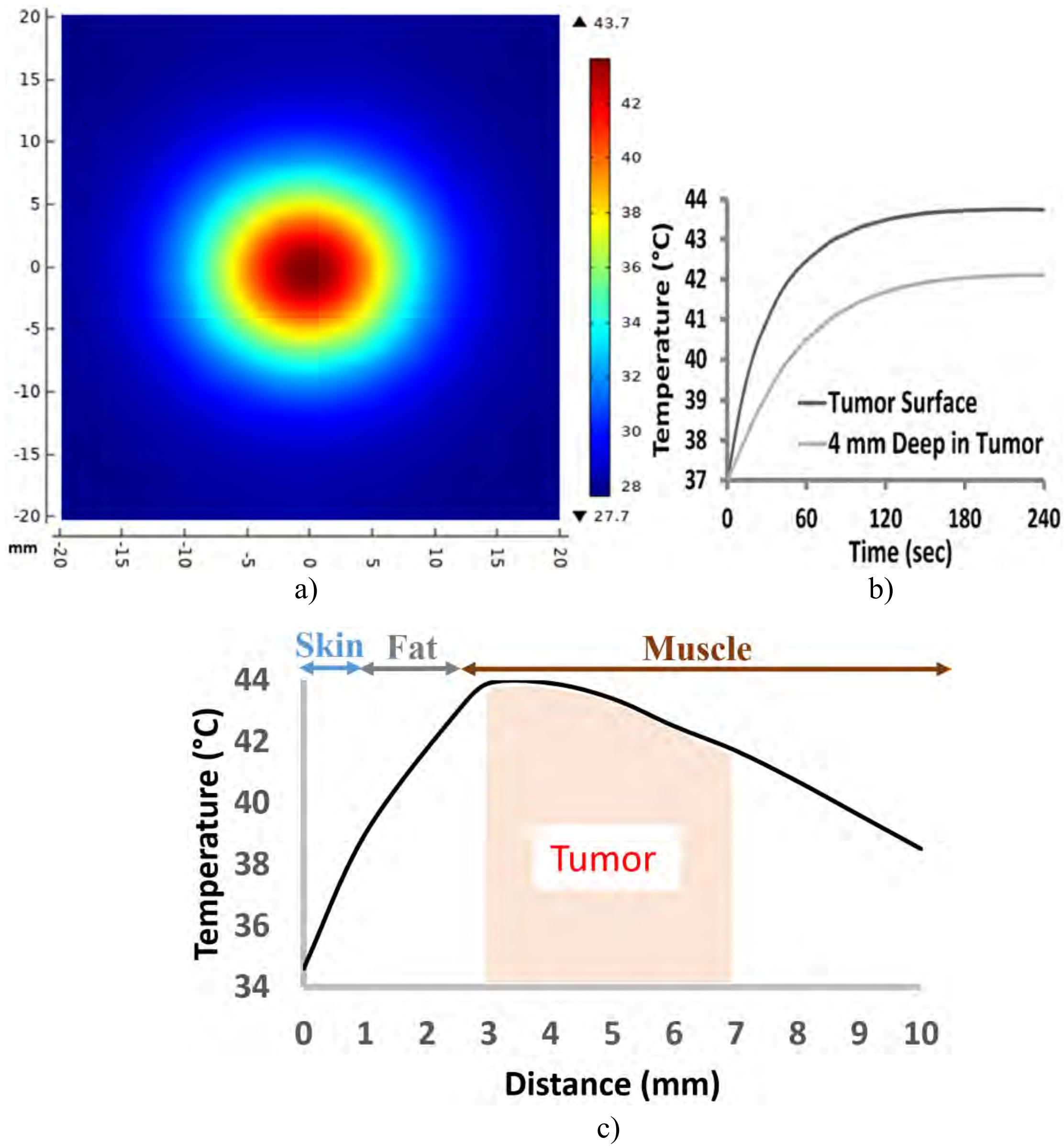

Figure 5.11 (a) Simulated temperature distribution on the location of the tumor surface, (b) is the simulated temperature change versus time at the upper surface and 4 mm deep in the tumor, and (c) temperature variations in the realistic HBM after 4 minutes testing.

The simulations were performed using 2.5 W RF input power, dielectric properties provided in [62] due to the forced air convection used in the previous section; for reasons explained below, the air velocity was set to 20 m/s instead of the 15 m/s used with the TPT. Fig. 5.11(a) illustrates the temperature distribution at the location of the tumor surface after 4 minutes of heating. As shown, the applicator uniformly heats the entire tumor surface to around 43 °C. Fig. 5.11(b) shows temperature change versus time on the tumor surface and 4 mm below the tumor surface. Fig. 5.11(c) shows the temperature variation inside the HBM versus depth after 4 minutes of heating. The maximum temperature in the skin and fat layers is lower than 42 °C. It can be observed that the desired temperature level (42-44 °C) is achieved in 3 minutes and remains in steady-state conditions. The duration can be reduced by applying a higher power level, but then a higher cooling capacity device is needed to keep surrounding healthy tissues lower than 42 °C. Variations in blood perfusion from the assumed model may be accounted for with adjustments in the RF power level, as noted in [71].

Comparing Fig. 5.10 and 11, it can be seen that there are only small differences between the heating characteristics of the TPT pork model and the realistic HBM model. These differences can be explained by variations in the dielectric properties between the two models. As seen in Fig. 11, the highest microwave absorption occurs in the skin layer, and this absorption consequently affects the temperature distribution in the deeper layers. Since the human skin absorbs more microwave energy than the pork skin, a higher air velocity was used for the HBM simulations to best match the TPT simulations, as noted previously. Because low microwave absorption occurs in the fat layer, its temperature is mainly dependent on the temperature of the skin and muscle tissues.

5.5. Conclusion and Discussions

There are several benefits to employing a dielectric rod antenna as part of an RF heating device for electroporation-based DNA delivery to subcutaneous tumors. From a mechanical perspective, the size and geometry of the antenna facilitate the integration of the needle electrode array that delivers the DC pulses to deliver DNA to the tumor cells. The relatively high directivity of the antenna, which is further enhanced with the addition of a low permittivity cladding, efficiently focuses electromagnetic energy on the targeted area to minimize the impact on surrounding tissue. By choosing the operating frequency correctly, the depth of the heat treatment can also be controlled. Since the DRA applicator works well at the frequencies of 7, 8 and 8.7 GHz frequencies, the penetration depth can be varied by several millimeters as needed. The simulation data and experimental results obtained by testing TPT indicate the accuracy of the simulation setup. By using the same simulation setup along with the biological factors of the human body, the system is shown to be capable of increasing the temperature of a tumor that is 3-7 mm below the skin surface in approximately 3 minutes, assuming an input 8 GHz power level of 2.5 W. The external factors of applied input power level, convective heat flux value, and operation frequency have a significant impact on the temperature elevation and required heating time.

Chapter VI :

Dielectric Lens Designs for Beam Shaping to Use in a Subdermal Tumor Treatment Technique

6.1. Introduction

The electroporation technique has shown promise in cancerous tumor treatment. The technique utilizes an electrode to apply direct current (DC) pulses to a tumor to temporarily weaken the cell membrane barrier, which enables the entry of DNA into the cell [56]. A recent study in skin tumor treatment revealed that heating the skin surface with infrared radiation to 43 °C before applying the DC pulses improved the DNA delivery by 8-fold [58]. This temperature rise could also help to reduce the required DC voltage level by about 50%. The study is limited only to skin tumor treatments due to infrared light's lack of penetration into deeper tissues. However, microwave radiation can penetrate into deeper tissues inversely proportional to its frequency. Thus, an end-fire dielectric rod antenna (DRA), which has a straightforward integration capability into a cylindrical electrode structure as shown in Fig. 6.1, can be used as a microwave energy source. Since it is important to limit heating outside of the tumor area, the antenna design is optimized for tumors in a narrow range of physical sizes. In order to treat tumors of different sizes, a new design of the antenna would generally be required.

However, an alternative approach to redesigning the antenna is to add a lens to modify the shape of the heated area. As shown herein, a planar diverging lens can be attached to the front-end of the DRA and used to control the heating zone. It is demonstrated that by only using different lenses, 8 to 16 mm diameter tumor sizes can

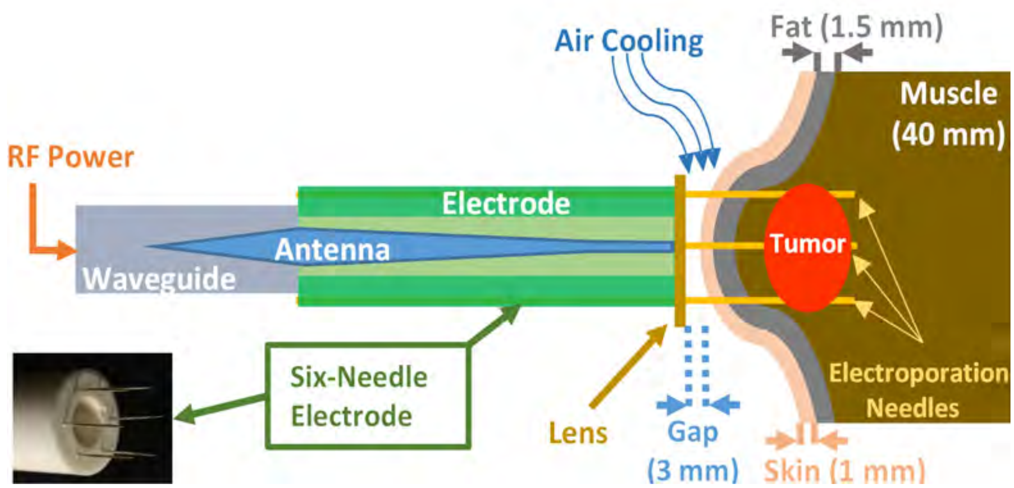

Figure 6.1 Model of the microwave heating system and location of the target tumor in the human body and photo of six-needle electrode.

be uniformly heated. Additionally, the designed lenses are thin (2.5 to 5 mm thick) and easy to fabricate as only one dielectric material is needed.

A variety of different lenses have been designed and employed for beam shaping and steering [72,73,74]. These applicators are usually designed to focus and shape the beam in the far field. On the contrary, the proposed dielectric rod antenna with the attached dielectric lens is used in this work to modify the beam shape in the near field.

6.2. Microwave Heating System Design, Fabrication, and Performance

The microwave heat applicator consists of a WR90 waveguide, a high permittivity DRA core encased in low permittivity 3D printed acrylonitrile butadiene styrene (ABS) plastic, and a planar dielectric lens. The DRA core is made of Rogers 3010 (ε_r=10.2 and tanδ=0.0035) and has a unique shape that is the combination of the feed taper, the body gradient, and the constant height sections. A 24 mm long feed taper

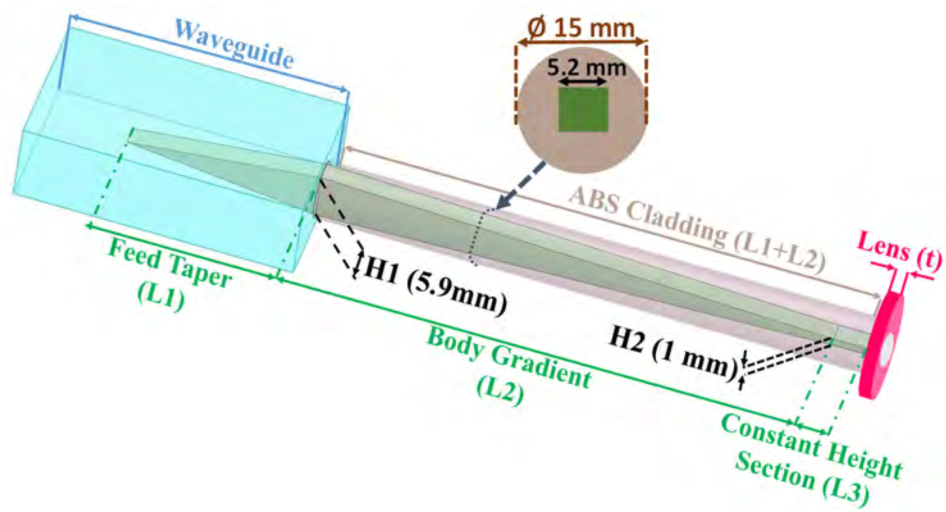

Figure 6.2 Proposed dielectric rod antenna microwave applicator.

(L1) is inserted into the metal waveguide feed and helps to align the impedance between the waveguide and DRA. A 73 mm long body gradient section (L2) reduces the sidelobe level, as described in [60]. The directionality of the DRA is maximized by the phase alignment between the aperture-emitted and surface wave fields with a 4.5 mm long constant height section (L3). The total DRA length has a significant effect on the half-power beam width. Additional directivity improvement and sidelobe radiation reduction are achieved by cladding the body gradient and constant height sections of the DRA core with ABS plastic (ε_r=2.6 and tanδ=0.003). The electroporation needles seen in Fig. 6.1, which are used to apply the DC pulses during DNA delivery, are not present during the heating cycle and are thus not accounted for in the antenna design due to the reasons explained in [75].

In order to use the same applicator for treating tumors of different sizes, the planar diverging dielectric lenses are attached to the front-end of the DRA. High permittivity Rogers 3010 (ε_r=10.2) is preferred for the lens material, while air (ε_r=1) is used for the central low permittivity region. The lenses shape the beam size because

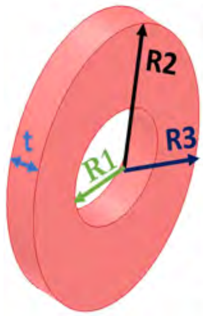

a)

	R1 (mm)	R2 (mm)	R3 (mm)	t (mm)
Lens 1	5	15	11.5	2.5
Lens 2	5	12.5	9.6	3.2
Lens 3	5	10	7.7	4.8
Lens 4	3	8	6.2	5.1

b)

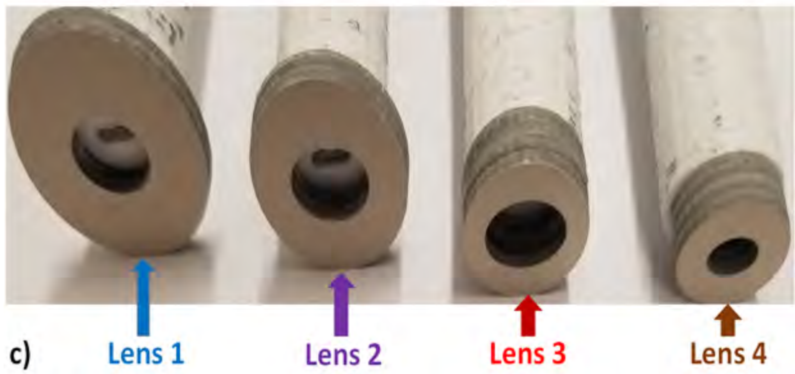

Figure 6.3 a) Model, b) design parameters of the lenses, and c) fabricated lenses.

the portion of the wave in the central low permittivity (air) section travels faster than the portion in the high permittivity region, causing the beam to diverge away from the central axis of the lens. Increasing the size of the high permittivity region increases the outward spreading of the energy. Additionally, because of the rectangular structure of the antenna's constant height section, a circular beam, which is desired for tumor treatment, is not achieved. However, using an elliptical shape for the lens allows additional control over the shape of the heating zone, and a circular shape can be achieved. The design parameters were found after optimizing in Ansys HFSS 19.2 and are given in Fig. 6.3.

A pork muscle tissue (PMT) was used to experimentally validate the performance of the applicator. The dielectric properties of PMT were measured using an Agilent 85070E open-ended dielectric probe and are given in Fig. 6.4. The data show

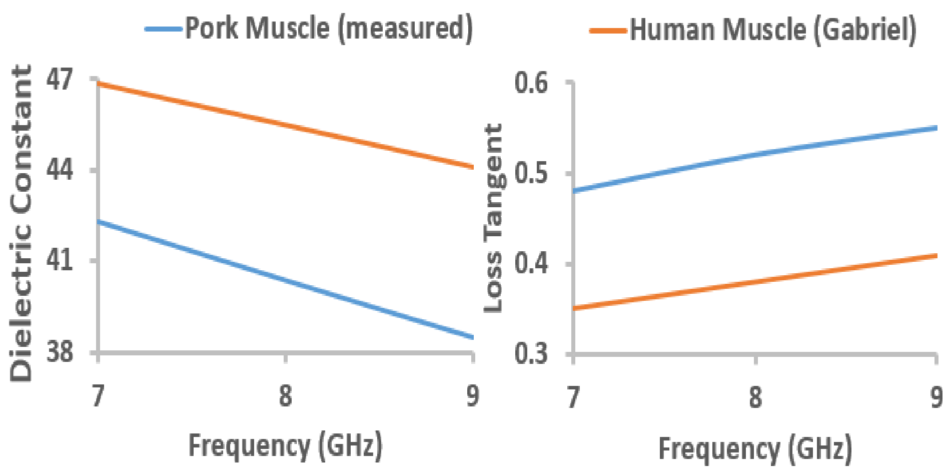

Figure 6.4 Comparison of measured dielectric constant and loss tangent of PMT compared with data from [62].

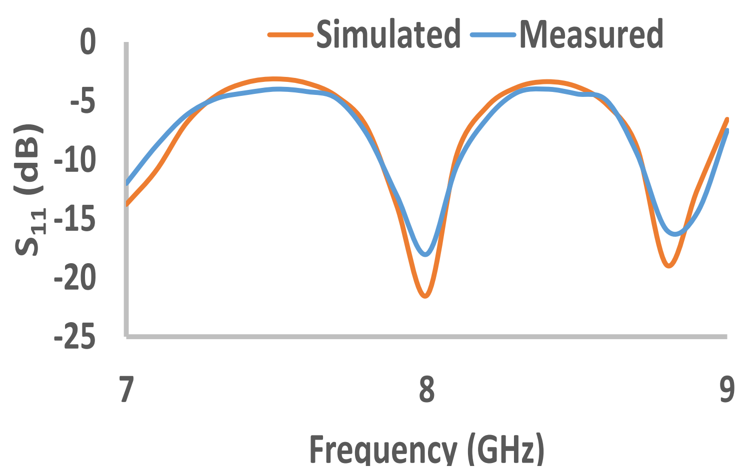

Figure 6.5 Comparison of reflection coefficient of the proposed antenna applicator terminated with PMT.

close enough agreement with the human muscle tissue dielectric properties measured by Gabriel et al. in [62] to approximate the microwave absorption by human tissues. The reflection coefficient at the antenna input port is improved by adjusting the thickness of the lens (t). The thickness and dielectric constant of the lenses are determined by treating them as a quarter-wavelength impedance transformer that is terminated by the muscle tissue. The measured and simulated data for the antenna reflection coefficient (S_{11}) are shown in Fig. 6.5. Since very similar responses are

Table 6.1 Measured PMT Thermal Properties Compared with Human Tissues [63,65]

Tissue Name	Thermal Conductivity (W/mK)	Heat Capacity (J/kg K)	Density (kg/m^3)
Human Muscle	0.42	3421	1090
Pork Muscle	0.453	3590	1050

obtained for all of the lens designs, only one measured data set is illustrated. The data indicate that more than 94% of the available source power can be transmitted at the 7 and 8.8 GHz frequencies, and more than 98% is transmitted at the operation frequency of 8 GHz. Thus, the penetration depth, which is inversely proportional to frequency, can be adjusted by a few millimeters if needed.

6.3. Simulation And Measurement of Temperature Distribution in the Pork Muscle Tissue

The temperature distribution on the surface of the PMT induced by the microwave applicator was measured with the test setup shown in Fig. 6.6. The measurement results are obtained by employing a FLIR E6 infrared camera and are compared with the simulation results of the Ansys Transient Thermal simulation in Fig.

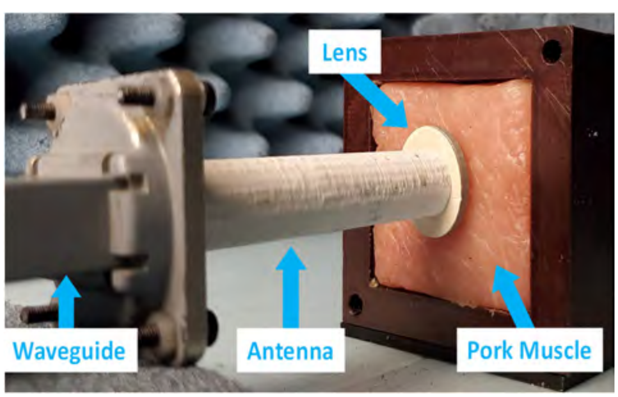

Figure 6.6 Fabricated DRA tested on PMT.

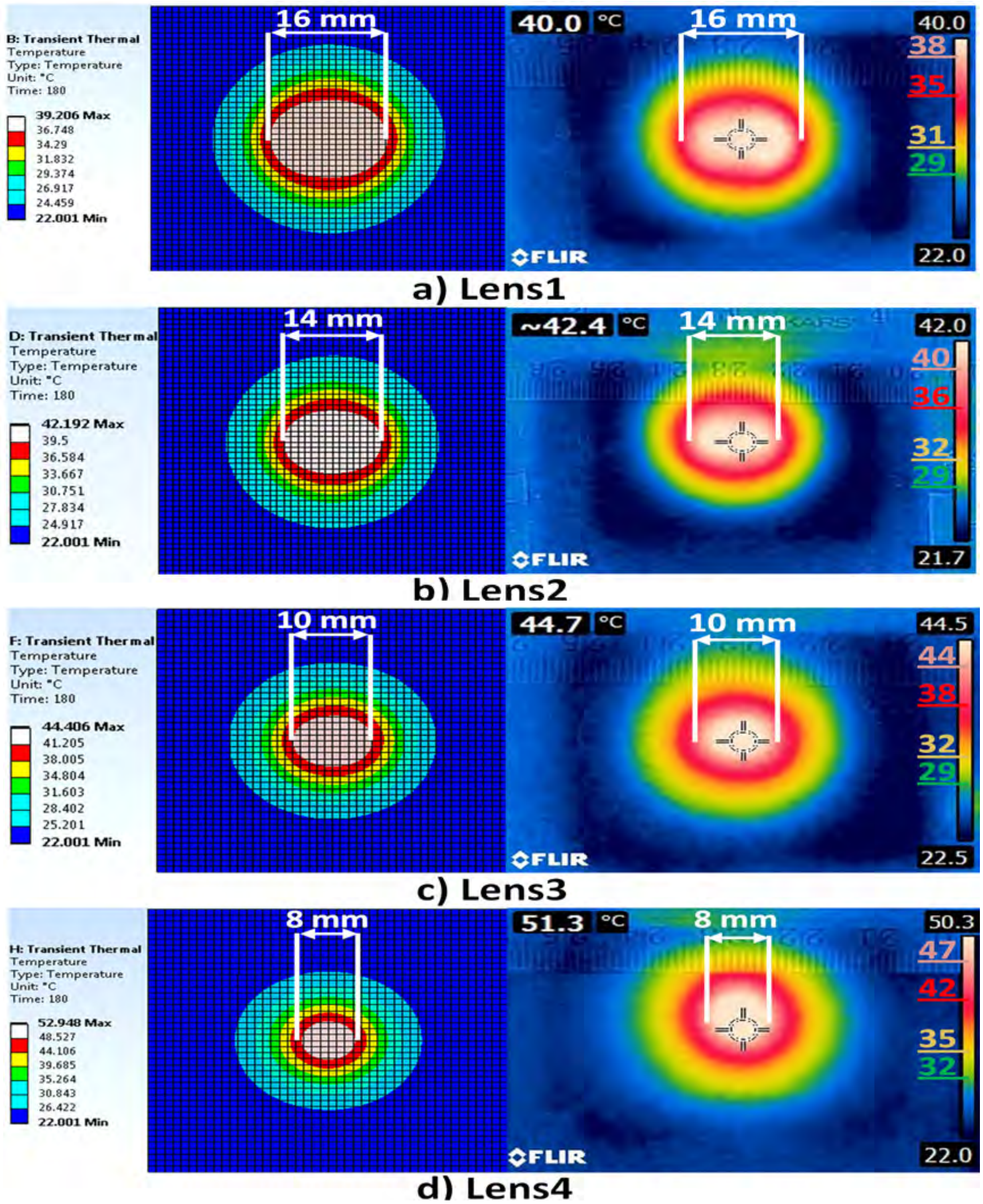

Figure 6.7 (a)-(d) Measured and simulated temperature distribution on PMT surface after 180 seconds of RF illumination.

6.7. The simulation setup is created by importing specific absorption rate (SAR) data, which is the measure of RF energy absorbed by tissues, from Ansys HFSS 19.2. The dielectric and thermal parameters of the PMT given in Fig. 6.5 and Table 6.1 were used for the simulations. Both simulated and measured figures were obtained after 180 seconds of 2.5 W and 8 GHz RF illumination. The thermal camera results were validated with thermocouples, and ± 0.8 °C difference was observed. Fig. 6.7 (a)-(d) illustrates that the measured temperature level and distribution are in good agreement with the simulations, and the desired beam shaping is achieved by the lenses. Each square on the simulated figure represents a 1x1 mm2 region, and a ruler is attached to the measurements in order to compare the distributions. The size of the hottest region on the thermal camera picture matches well with the thermal simulations as 16, 14, 10, and 8 mm in diameter, respectively. Additionally, while the peak measured temperatures were 40, 42.4, 44.7, and 51.3 °C for four different lens designs, these values for the simulations were 39.2, 42, 44.4, and 52.9 °C, respectively. The coldest regions in all figures were 22 °C which was the initial temperature of the PMT. As expected, greater beam divergence results in a lower temperature value since the applied power is distributed over a larger region. In order to equalize the temperature value differences of the lenses, the input power level can be adjusted.

6.4. Temperature Distribution Analysis on a Realistic Human Body Model

Based on the model of the microwave heating system given in Fig. 6.1, simulations were made using a realistic human body model (HBM) in Ansys Transient Thermal. The dielectric and thermal properties of the tissues were obtained from [62,63,65]. The tumor is presumed to have a 3-4 mm height and be located 3 mm deep inside of the skin surface. To limit the temperature elevation in the skin and fat tissues, 5 °C cold air was assumed to be blown across the skin surface through the 3 mm gap

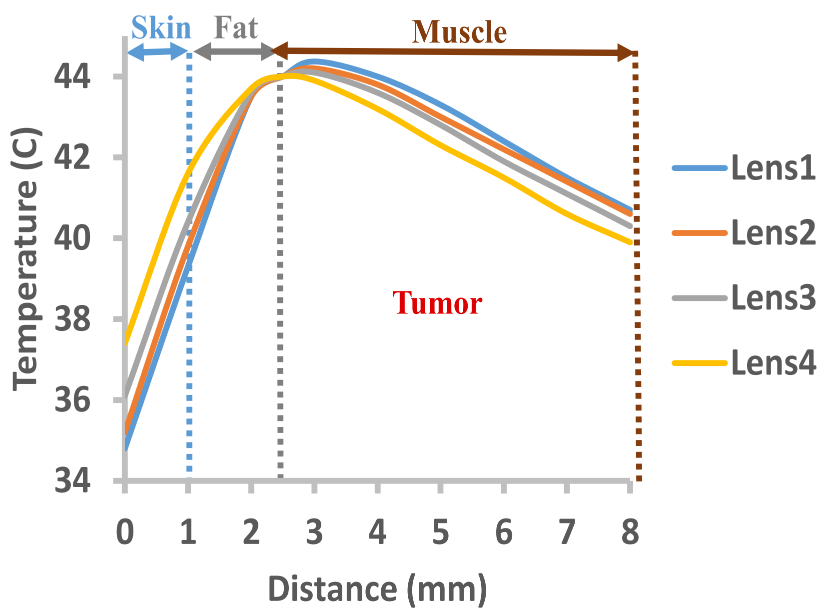

Figure 6.8 Temperature variations in the realistic HBM after 3 minutes testing.

between the applicator and human body model while testing. The average forced convection heat transfer coefficient caused by the forced air cooling was taken 90 W/ (m^2 K). Increasing this value would result in lowering the temperature values in the heated regions.

Fig. 6.8 shows the temperature variation inside the HBM versus depth after 3 minutes of RF illumination. In order to achieve the desired temperature level of 42-44 °C in the tumor location for each case, 3.6 W, 2.9 W, 2.7 W, and 2.1 W RF input power levels needed to be applied to the applicators with Lens 1, 2, 3, and 4, respectively. The observed temperature distribution at the tumor location is very similar to Fig. 6.7, where the 42-44 °C region sizes have nearly circular shapes and can vary from 8 mm to 16 mm in diameter. Additionally, the maximum temperature in all tissues was lower than 42 °C except for the presumed tumor location. The data demonstrated that different sizes of tumors could be heated to the desired temperature level while surrounding tissues were minimally impacted. The temperature variation in the tumor and heating duration can be controlled by changing the power level and cooling capacity, while deeper tumors can be treated by lowering the frequency.

6.5. Conclusions

In this work, planar dielectric lens designs that can be attached to the front-end of a relatively high directivity dielectric rod antenna are introduced. The size and geometry of the antenna and lenses allow easy and straightforward integration into the electrode structure. The lenses are able to adjust the beam size and can be used to treat tumors in size of 8-16 mm diameter while surrounding tissues are prevented from excessive heating. The proposed applicators only require a 2.1-3.6 W input power level and 3 minutes of testing to achieve desired temperature level of 42-44 °C in the tumor region. The input power level and the convective heat transfer coefficient value caused by the forced air cooling played a key role in the temperature elevation and required heating time. Additionally, since the applicator operates at the 7, 8, and 9 GHz bands, the penetration depth can be increased or decreased by a few millimeters if needed.

Chapter VII :

Conclusions and Future Work

This dissertation has shown the potential of FDRs to be used in lossy environments for moisture and displacement sensing. Current technical challenges with the FDR design to be used in environmental sensing applications are addressed, and the following improvements are made: (a) significant read range extension, (b) mechanical tunability, (c) narrow bandwidth, (d) small size, and (e) low-cost. The temperature dependency of the FDR is also investigated to be used in different environmental conditions, and a small variation is observed between the ambient temperatures of -20 and 55 ºC.

Tracking the attenuation in the signal, traveling between an embedded FDR and the interrogator, can provide a very good sign about its moisture content. To create the relationship between attenuation and moisture content, the dielectric properties of the environment need to be known. The environment of interest in the dissertation is railroad track ballast which has a heterogeneous and multi-dielectric structure. It is comprised of ballast, fouling (coal dust), moisture (water), and void (air). Since the complex permittivity does not increase linearly with the moisture content, a dielectric mixing model is proposed in this dissertation to characterize the permittivity. The simulation-based model takes the measured coal dust and moisture mixture, ballast, and air dielectric properties individually, and creates a complex permittivity based on the materials' volumetric percentages in the mixture. The calculated attenuation from the complex permittivity was in good agreement with lab experiments, which verified the accuracy of the model. The model has overcome the issues with the methods in the literature that are underestimating the dielectric properties. The proposed dielectric mixing model can be used to analyze the dielectric properties of other environments. An important observation in this work is that neither established mixing models nor the simulations will accurately predict the complex permittivity of the composite coal dust–moisture mixture, especially at higher moisture levels. In our experiments, it was found that there is a non-linear relationship between the material composition and the resulting loss tangent that these models do not predict. For example, the loss tangent of dry coal dust and water are 0.04 and 0.065, respectively. However, when a small amount of water is introduced to coal dust, the loss tangent of the mixture becomes around 0.3. For this reason, the measured data for the permittivity of the coal dust and water mixture is used in the model. The physical or chemical reactions between the coal dust and water that causes the non-linear change in the loss tangent need to be studied.

Novel interferometric localization and displacement measurement techniques are proposed by using a pair of FDRs. The basic principle of this technique relies on the received constructive and destructive interferences when two FDRs are interrogated from different angles. The peak and null locations in the received signal can help predict the separation distance of the FDRs and so the displacement. The same approach can also be applied to find the sensor locations with sufficient accuracy. The measurement results made in free space that are in very good agreement with the calculations give an important sign of the viability of the technique in the real environment.

Both moisture, displacement, and localization sensing approaches have not been tested when the FDRs are embedded in the railroad environment. The FDRs are designed to radiate in free space, so embedding them in an environment that does not have a free-space impedance anymore can cause resonant frequency shifts, which degrades the conversion efficiency. Radiation patterns may also alter slightly. To address these issues, the FDR antennas can be either redesigned based on the wave impedance of the environment, or the resonant frequency of the antenna can be adjusted and optimized with mechanical tunability. Additionally, instead of using two antennas for receive and transmit signals, the FDR design that is using only one antenna along with a diplexer can be considered as mentioned in [33]. This can reduce the redesign or tunability mechanism complexity as well as overcome the coupling issues between two closely spaced antennas. The multi-path effects can also be observed, especially in high moisture content environments. For the displacement and localization measurements, there are a few presumptions made, i.e. the FDRs are positioned on the same axis (y-axis). Due to the natural conditions, the FDRs level may misalign or may roll over. For all these conditions, a near-isotropic FDR antenna design should be considered. This can be achieved by adding orthogonally oriented dipole elements to the proposed FDR antennas and creating crossed dipole antennas as explained in [76]. Or a pair of FDRs may simply be positioned orthogonally and combined to each other.

A microwave applicator that can integrate into a six-electrode is designed and characterized to assist the gene therapy technique used in cancerous tumor treatment. The lab testing on pork tissues showed that the designed end-fire dielectric rod antenna (DRA) is able to concentrate the microwave energy into the confined tumor location, that is between 3-7 mm below the skin surface, and heat the tumor 5 to 7 ºC in a short period of time without damaging surrounding tissues. Very thin layer dielectric lenses that can be attachable front-end of the DRA and shape its beam size are designed to be able to treat different sizes of tumors. The simulated data obtained from the multi-physics simulation model was in very good agreement with the measurement results. Therefore, the same simulation setup is applied to human body tissues by taking some of the human body's physiological effects into account (i.e. blood perfusion rate). The simulation results reveal that the same applicator can be used in human tissues by just adjusting the input power level. However, the simulated model is not taking all of the living tissue properties into account, thus more studies on living tissues need to be done. Additionally, while heating the tissues with the applicator, a thermocouple is used to measure the temperature rise, which is not a practical method while testing in living tissues. A microwave radiometer approach can be used to overcome this issue, and the microwave applicator used in the tumor heating can do the temperature measurements as well.

Bibliography

1. Lynch, J.P.; Farrar, C.R.; Michaels, J.E. Structural health monitoring: Technological advances to practical implementations. Proc. IEEE 2016, 104, 1508–1512.

2. Yiming Liu, Yi Bao, Review of electromagnetic waves-based distance measurement technologies for remote monitoring of civil engineering structures, Measurement, Volume 176, 2021, 109193,ISSN 0263-2241.

3. https://arxiv.org/abs/1912.12382

4. J. Wardlaw, I. Karaman, and A. Karsilayan, "Low-power circuits and energy harvesting for structural health monitoring of bridges," IEEE Sensors Journal, , vol. 13, no. 2, pp.709-722, Feb. 2013.

5. T. Weller, J. Wang, J. Frolik, I. Nassar, J. Dewney, R. Davidova, and V. Sakamuri, A wireless interrogator - passive sensor approach for deeply embedded sensing applications, IEEE Int. Symposium on Antennas and Propagation, Spokane, WA, July 4-11, 2011.

6. Zhang, J.; Tian, G.Y.; Marindra, A.M.J.; Sunny, A.I.; Zhao, A.B. A Review of Passive RFID Tag Antenna-Based Sensors and Systems for Structural Health Monitoring Applications. Sensors 2017, 17, 265. https://doi.org/10.3390/s17020265

7. Li, F.; Xiang, D.; Chiang, S.; Tittmann, B.R.; Searfass, C. Wireless Surface Acoustic Wave Radio Frequency Identification (SAW-RFID) Sensor System for Temperature and Strain Measurements. In Proceedings of the IEEE International Ultrasonics Symposium (IUS), Dresden, Germany, 7–10 October 2012.

8. C. Strangfeld, S. Johann, M. Müller and M. Bartholmai, "Embedded passive RFID-based sensors for moisture monitoring in concrete," 2017 IEEE SENSORS, 2017, pp. 1-3, doi: 10.1109/ICSENS.2017.8234166.

9. Yee Jher Chan, Adam R. Carr, Subhanwit Roy, Caden M. Washburn, Nathan M. Neihart, Nigel F. Reuel, Positionally-independent and extended read range resonant sensors applied to deep soil moisture monitoring, Sensors and Actuators A: Physical, Volume 333, 2022, 113227, SSN 0924-4247, https://doi.org/10.1016/j.sna.2021.113227.

10. M. I. M. Ghazali, S. Karuppuswami, and P. Chahal. 3-D Printed Embedded Passive Harmonic Sensor Tag as Markers for Buried Assets Localization. IEEE Sensors Letters, 3(4):1–4, April 2019.

11. Nassar, I.T.; Weller, T.M., "A Compact Dual-Channel Transceiver for Long-Range Passive Embedded Monitoring," Microwave Theory and Techniques, IEEE Transactions on, vol.63, no.1, pp.287,294, Jan. 2015

12. Leng, Z., & Al-Qadi, I. L. (2010). Railroad Ballast Evaluation Using Ground-Penetrating Radar: Laboratory Investigation and Field Validation. Transportation Research Record, 2159(1), 110–117. https://doi.org/10.3141/2159-14

13. Bruzek R, Stark TD, Sussmann T, Tunna J, Thompson H., "Fouled Ballast Waiver Operations and Results" United States Dept. of Transp. Fed. Rail Admin 2022, No. DOT/FRA/ORD-22/01, https://rosap.ntl.bts.gov/view/dot/59915.

14. T. Nassar, T. M. Weller and J. L. Frolik, "A Compact 3-D Harmonic Repeater for Passive Wireless Sensing," in IEEE Transactions on Microwave Theory and Techniques, vol. 60, no. 10, pp. 3309-3316, Oct. 2012, doi: 10.1109/TMTT.2012.2210440.

15. M. C. Dobson, F. T. Ulaby, M. T. Hallikainen and M. A. El-rayes, "Microwave Dielectric Behavior of Wet Soil-Part II: Dielectric Mixing Models," in IEEE Transactions on Geoscience and Remote Sensing, vol. GE-23, no. 1, pp. 35-46, Jan. 1985, doi: 10.1109/TGRS.1985.289498.

16. Beer, Einleitung in die Hohere Optik. Braunschweig, Germany: Druck und Verlag von Friedrich Vieweg und Sohn, 1853, p. 35.

17. J. C. Philip, "Das dielectrische Verhalten flussiger Mischungen, besonders verdunnter Losungen," Zeitschrift fur Physikalische Chemie, vol.24, pp. 18–38, 1897.

18. H. H. Lowry, "The significance of the dielectric constant of a mixture," J. Franklin Inst., vol. 203, pp. 413–439, 1927.

19. J. R. Birchak, C. G. Gardner, J. E. Hipp, and J. M. Victor, "High dielectric constant microwave probes for sensing soil moisture," Proc. IEEE, vol. 62, no. 1, pp. 93–98, Jan. 1974.

20. A. Kraszewski, "Prediction of the dielectric properties of two-phase mixtures," J. Microw. Power, vol. 12, no. 3, pp. 216–222, 1977.

21. P. N. Sen, C. Scala, and M. H. Cohen, "A self-similar model for sedimentary rocks with application to the dielectric constant of fused glass beads," Geophys., vol. 46, no. 5, pp. 781–795, 1981.

22. L. C. Shen, W. C. Savre, M. M. Price, and K. Athavael, "Dielectric properties of reservoir rocks at ultra-high frequencies," Geophys., vol. 50, no. 4, pp. 692–704, 1985.

23. S. O. Nelson, "Density-permittivity relationships for powdered and granular materials," in IEEE Transactions on Instrumentation and Measurement, vol. 54, no. 5, pp. 2033-2040, Oct. 2005, doi: 10.1109/TIM.2005.853346.

24. Im, S.B.; Hurlebaus, S.; Kang, Y.J. Summary Review of GPS Technology for Structural Health Monitoring. J. Struct. Eng. 2013, 139, 1653–1664.

25. Li, C.; Chen, W.; Liu, G.; Yan, R.; Xu, H.; Qi, Y. A Noncontact FMCW Radar Sensor for Displacement Measurement in Structural Health Monitoring. Sensors 2015, 15, 7412-7433. https://doi.org/10.3390/s150407412

26. Mario J. Cazeca, Joey Mead, Julie Chen, Ramaswamy Nagarajan, Passive wireless displacement sensor based on RFID technology, Sensors and Actuators A: Physical, Volume 190, 2013, Pages 197-202, ISSN 0924-4247, https://doi.org/10.1016/j.sna.2012.11.007.

27. Donate, A. Bulysheva, C. Edelblute, D. Jung, M.A. Malik, S. Guo, N. Burcus, K. Schoenbach, and R. Heller, "Thermal Assisted In Vivo Gene Electrotransfer," in Curr Gene Ther., 2016, 16(2):83-9.

28. K. S. Nikita and N. K. Uzunoglu, "Analysis of the power coupling from a waveguide hyperthermia applicator into a three-layered tissue model," in IEEE Transactions on Microwave Theory and Techniques, vol. 37, no. 11, pp. 1794-1801, Nov. 1989.

29. S. Curto, "Antenna development for radio frequency hyperthermia applications," Ph.D. dissertation, Dept. Electron. Commun. Eng., Dublin Inst. Technol., Dublin, Ireland, 2016. [Online]. Available: http://arrow.dit.ie/engdoc/38/

30. S. Curto and M. J. Ammann, "Electromagnetic interaction between resonant loop antenna and simulated biological tissue," in Microwave and Optical Technology Letters, vol. 48, no. 12, pp. 2421-2425, Dec. 2006.

31. Y. Nikawa and F. Okada, "Dielectric-loaded lens applicator for microwave hyperthermia, " in IEEE Transactions on Microwave Theory and Techniques, vol. 39, no. 7, pp. 1178-1178, July 1991.

32. Soni Singh, Bhagirath Sahu and S.P. Singh "Direct-Contact Water-Loaded Metal-Dielectric Wall Diagonal Horn Applicators for Hyperthermia," in IETE Technical Review, 2018, 35:2, 122-131.

33. X. Gu, N. N. Srinaga, L. Guo, S. Hemour and K. Wu, "Diplexer-Based Fully Passive Harmonic Transponder for Sub-6-GHz 5G-Compatible IoT Applications," in IEEE Transactions on Microwave Theory and Techniques, vol. 67, no. 5, pp. 1675-1687, May 2019, doi: 10.1109/TMTT.2018.2883979.

34. S. M. Aguilar and T. M. Weller, "Tunable harmonic re-radiator for sensing applications," 2009 IEEE MTT-S International Microwave Symposium Digest, 2009, pp. 1565-1568, doi: 10.1109/MWSYM.2009.5166009.

35. I. H. Uluer, J. Frolik and T. M. Weller, "Battery-free Mechanically-Tunable Wireless Sensors for Railroad Track Ballast Monitoring," 2022 IEEE International Symposium on Antennas and Propagation and USNC-URSI Radio Science Meeting (AP-S/URSI), 2022, pp. 117-118, doi: 10.1109/AP-S/USNC-URSI47032.2022.9886888.

36. H.A. Wheeler, "The Radiansphere around a Small Antenna," Proceedings of the IRE , vol.47, no.8, pp.1325-1331, Aug. 1959

37. David M. Pozar, ―Microwave Engineering‖, Third Edition, John Wiley & Sons, Inc., new Jersey, PP.98-106, 1998

38. ANSYS Academic Research HFSS, Release 22.2, Help System, Lumped Port, ANSYS, Inc.

39. ANSYS® Academic Research HFSS, Release 22.2, Help System, Setting the Maximum Delta S Per Pass, ANSYS, Inc.

40. https://www.rogerscorp.com/advanced-electronics-solutions/ro3000-series-laminates/ro3010-laminates.

41. Stephen Maas, Nonlinear Microwave and RF Circuits, Second Edition , Artech, 2003.

42. Modelithics Library

43. X. Gu, W. Lin, S. Hemour and K. Wu, "Readout Distance Enhancement of Battery-Free Harmonic Transponder," in IEEE Transactions on Microwave Theory and Techniques, vol. 69, no. 7, pp. 3413-3424, July 2021, doi: 10.1109/TMTT.2021.3068291.

44. J. Frolik, J. E. Lens, M. M. Dewoolkar and T. M. Weller, "Effects of Soil Characteristics on Passive Wireless Sensor Interrogation," in IEEE Sensors Journal, vol. 18, no. 8, pp. 3454-3460, April 15, 2018, doi: 10.1109/JSEN.2018.2810132.

45. F. De Chiara, S. Fontul and E. Fortunato, "GPR laboratory tests for railways materials dielectric properties assessments," Remote Sensing, Vol. 6, 2014.

46. ANSYS Academic Research HFSS, Release 20.2, Help System, Floquet Ports, ANSYS, Inc.

47. A. M. Nicolson and G. F. Ross, "Measurement of the Intrinsic Properties of Materials by Time-Domain Techniques," in IEEE Transactions on Instrumentation and Measurement, vol. 19, no. 4, pp. 377-382, Nov. 1970, doi: 10.1109/TIM.1970.4313932.

48. S. O. Nelson, "Density-permittivity relationships for powdered and granular materials," in IEEE Transactions on Instrumentation and Measurement, vol. 54, no. 5, pp. 2033-2040, Oct. 2005, doi: 10.1109/TIM.2005.853346.

49. M. J. Akhtar, H. B. Baskey, P. Ghising and N. M. Krishna, "Microwave effective permittivity of the layered dielectrics and composites using the nonlinear mixing model," in IEEE Transactions on Dielectrics and Electrical Insulation, vol. 22, no. 3, pp. 1702-1710, June 2015, doi: 10.1109/TDEI.2015.7116367.

50. FRA Broad Agency Announcement 2019.

51. https://en.wikipedia.org/wiki/Global_Positioning_System

52. A. Daud, R. C. DeConti, S. Andrews, P. Urbas, A. Riker, V. K. Sondak, P. N. Munster, D. M. Sullivan, K. E. Ugen, J. L. Messina, and R. Heller, “Phase I trial of interleukin-12 plasmid electroporation in patients with metastatic melanoma,” in J Clin Oncol., Dec 2008, 26(36):5896-903.

53. A. V. Titomirov, S. Sukharev, and E. Kistanova, “In vivo electroporation and stable transformation of skin cells of newborn mice by plasmid DNA,” in Biochim Biophys Acta., Jan 1991, 1088(1):131-4.

54. R. Heller, M. Jaroszeski, A. Atkin, D. Moradpour, R. Gilbert, J. Wands, and C. Nicolau, “In vivo gene electroinjection and expression in rat liver,” in FEBS Lett., Jul 1996, 389(3):225-8.

55. M. Golzio, J. Teissie, and M.P. Rols, “Direct visualization at the single-cell level of electrically mediated gene delivery,” in Proceedings of the National Academy of Sciences, Feb 2002, 99(3):1292-1297.

56. R. Heller, Y. Cruz, L. C. Heller, R. A. Gilbert, and M. J. Jaroszeski, “Electrically mediated delivery of plasmid DNA to the skin, using a multielectrode array,” in Hum Gene Ther., Mar 2010, 21(3):357-62.

57. R. Heller, and L. C. Heller, “Gene electrotransfer clinical trials,” in Adv. Genet., 2015, 89:235-262.

58. A. Bulysheva, J. Hornef, C. Edelblute, C. Jiang, K. Schoenbach, C. Lundberg, M.A. Malik, and R. Heller, “Coalesced thermal and electrotransfer mediated delivery of plasmid DNA to the skin,” in Bioelectrochemistry, Feb. 2019, 125:127-133.

59. S. Maluta, and M. W. Kolff, “Role of hyperthermia in breast cancer locoregional recurrence: a review,” in Breast Care (Basel), Dec 2015, 10(6): 408–412.

60. D. C. Lugo, R. A. Ramirez, J. Wang and T. M. Weller, “Multilayer Dielectric End-Fire Antenna With Enhanced Gain,” in IEEE Antennas and Wireless Propagation Letters, vol. 17, no. 12, pp. 2213-2217, Dec. 2018.

61. T. Yilmaz, R. Foster and Y. Hao, “Broadband Tissue Mimicking Phantoms and a Patch Resonator for Evaluating Noninvasive Monitoring of Blood Glucose Levels,” in IEEE Transactions on Antennas and Propagation, vol. 62, no. 6, pp. 3064-3075, June 2014.

62. C Gabriel et al 1996 Phys. Med. Biol. 41 2231.

63. ASHRAE 2006, Chapter 9 - Thermal properties of foods, In: Handbook - Refrigeration, Georgia: 9.1-9.31.

64. Krishnan S. et al., “Multimodal epidermal devices for hydration monitoring”, Microsyst. Nanoeng., 3 (2017), p. 17014

65. IT’IS Foundation, “Tissue Properties,” [Online]. Available: https://itis.swiss/virtual-population/tissue-properties/database. Accessed Oct 2019.

66. Cone, Stephanie G et al. “Rise of the Pigs: Utilization of the Porcine Model to Study Musculoskeletal Biomechanics and Tissue Engineering During Skeletal Growth.” Tissue engineering. Part C, Methods vol. 23,11 (2017): 763-780.

67. M. Ngadi et al., “Dielectric Properties of Pork Muscle,” International Journal of Food Properties, 18:1, 12-20, 2015.

68. M. Lazebnik et al., “A large-scale study of the ultrawideband microwave dielectric properties of normal, benign and malignant breast tissue obtained from cancer surgeries,” in Phys. Med. Biol., vol. 52, pp. 6093-6115, 2007.

69. ANSYS® Academic Research HFSS, Release 19.2, Help System, Calculating the SAR, ANSYS, Inc.

70. Bernardi, P., M. Cavagnaro, S. Pisa, and E. Piuzzi, “Specific absorption rate and temperature elevation in a subject exposed in the far-field of radio-frequency sources operating in the 10–900- MHz range,” in IEEE Trans. Biomed. Eng., Vol. 50, No. 3, 295–304, 1998.

71. G. Muntoni, A. Fanti, G. Montisci and M. Muntoni, "A Blood Perfusion Model of a RMS Tumor in a Local Hyperthermia Multi-Physic Scenario: A Preliminary Study," in IEEE Journal of Electromagnetics, RF and Microwaves in Medicine and Biology, vol. 3, no. 1, pp. 71-78, March 2019.

72. Y. Zhang, W. Hong, and Y. Zhang, “A beam steerable plane dielectric lens antenna,” in Proc. Int. Symp. Antennas Propag., Oct. 23–25, 2013, vol. 01, pp. 476–479

73. A. Petosa, and A. Ittipiboon, "Design and performance of a perforated dielectric fresnel lens," Microwaves, Antennas and Propagation, IEE Proceedings, vol.150, no.5, pp. 309- 314, 10 Oct. 2003.

74. Marc Imbert, Anna Papió, Franco De Flaviis, Lluís Jofre, Jordi Romeu, "Design and Performance Evaluation of a Dielectric Flat Lens Antenna for Millimeter-Wave Applications", Antennas and Wireless Propagation Letters IEEE, vol. 14, pp. 342-345, 2015.

75. I. H. Uluer, M. J. Jaroszeski, J. L. Gess and T. M. Weller, "An X-Band Dielectric Rod Antenna for Subdermal Tumor Heating to Assist Electroporation-Mediated DNA Delivery," in IEEE Journal of Electromagnetics, RF and Microwaves in Medicine and Biology, doi: 10.1109/JERM.2021.3053082.

76. S. X. Ta, I. Park and R. W. Ziolkowski, "Crossed Dipole Antennas: A review," in *IEEE Antennas and Propagation Magazine*, vol. 57, no. 5, pp. 107-122, Oct. 2015, doi: 10.1109/MAP.2015.2470680.

Appendix

Appendix A : Data File Based Band Pass Filters

a) Data File Based 1.19 GHz (f_0) Band Pass Filter

```
!         Frequency           S11       S21       S12       S22
#         HZ        S         DB        R         50
0.000E+09           0         0         -1000     0         -1000     0         0         0
0.100E+09           0         0         -1000     0         -1000     0         0         0
   |                |         |           |                   |                 |         |
   |                |         |           |                   |                 |         |
   |                |         |           |                   |                 |         |
1.188E+09           0         0         -1000     0         -1000     0         0         0
1.189E+09           0         0         -1000     0         -1000     0         0         0
1.190E+09           -1000     0         0         0         0         0         -1000     0
1.191E+09           0         0         -1000     0         -1000     0         0         0
   |                |         |           |                   |                 |         |
   |                |         |           |                   |                 |         |
   |                |         |           |                   |                 |         |
2.380E+09           0         0         -1000     0         -1000     0         0         0
   |                |         |           |                   |                 |         |
   |                |         |           |                   |                 |         |
   |                |         |           |                   |                 |         |
3.760E+09           0         0         -1000     0         -1000     0         0         0
   |                |         |           |                   |                 |         |
   |                |         |           |                   |                 |         |
   |                |         |           |                   |                 |         |
4.760E+09           0         0         -1000     0         -1000     0         0         0
```

b) Data File Based 2.38 GHz ($2f_0$) Band Pass Filter

```
!         Frequency           S11       S21       S12       S22
#         HZ        S         DB        R         50
0.000E+09           0         0         -1000     0         -1000     0         0         0
0.100E+09           0         0         -1000     0         -1000     0         0         0
   |                |         |           |                   |                 |         |
   |                |         |           |                   |                 |         |
   |                |         |           |                   |                 |         |
1.190E+09           0         0         -1000     0         -1000     0         0         0
   |                |         |           |                   |                 |         |
   |                |         |           |                   |                 |         |
   |                |         |           |                   |                 |         |
2.379E+09           0         0         -1000     0         -1000     0         0         0
2.380E+09           -1000     0         0         0         0         0         -1000     0
2.381E+09           0         0         -1000     0         -1000     0         0         0
   |                |         |           |                   |                 |         |
   |                |         |           |                   |                 |         |
   |                |         |           |                   |                 |         |
3.760E+09           0         0         -1000     0         -1000     0         0         0
   |                |         |           |                   |                 |         |
   |                |         |           |                   |                 |         |
   |                |         |           |                   |                 |         |
4.760E+09           0         0         -1000     0         -1000     0         0         0
```

c) Data File Based 3.57 GHz ($3f_0$) Band Pass Filter

```
!           Frequency          S11         S21        S12         S22
#           HZ          S      DB          R          50
0.000E+09   0           0      -1000       0          -1000       0       0       0
0.100E+09   0           0      -1000       0          -1000       0       0       0
   |        |           |         |                      |                |       |
   |        |           |         |                      |                |       |
   |        |           |         |                      |                |       |
1.190E+09   0           0      -1000       0          -1000       0       0       0
   |        |           |         |                      |                |       |
   |        |           |         |                      |                |       |
   |        |           |         |                      |                |       |
2.380E+09   0           0      -1000       0          -1000       0       0       0
   |        |           |         |                      |                |       |
   |        |           |         |                      |                |       |
   |        |           |         |                      |                |       |
3.759E+09   0           0      -1000       0          -1000       0       0       0
3.760E+09   -1000       0      0           0          0           0       -1000   0
3.761E+09   0           0      -1000       0          -1000       0       0       0
   |        |           |         |                      |                |       |
   |        |           |         |                      |                |       |
   |        |           |         |                      |                |       |
4.760E+09   0           0      -1000       0          -1000       0       0       0
```

d) Data File Based 4.76 GHz ($4f_0$) Band Pass Filter

```
!           Frequency          S11         S21        S12         S22
#           HZ          S      DB          R          50
0.000E+09   0           0      -1000       0          -1000       0       0       0
0.100E+09   0           0      -1000       0          -1000       0       0       0
   |        |           |         |                      |                |       |
   |        |           |         |                      |                |       |
   |        |           |         |                      |                |       |
1.190E+09   0           0      -1000       0          -1000       0       0       0
   |        |           |         |                      |                |       |
   |        |           |         |                      |                |       |
   |        |           |         |                      |                |       |
2.380E+09   0           0      -1000       0          -1000       0       0       0
   |        |           |         |                      |                |       |
   |        |           |         |                      |                |       |
   |        |           |         |                      |                |       |
3.760E+09   0           0      -1000       0          -1000       0       0       0
   |        |           |         |                      |                |       |
   |        |           |         |                      |                |       |
   |        |           |         |                      |                |       |
4.759E+09   0           0      -1000       0          -1000       0       0       0
4.760E+09   -1000       0      0           0          0           0       -1000   0
4.761E+09   0           0      -1000       0          -1000       0       0       0
```

e) A MATLAB Code That Can Create f_0 to $4f_0$ BPF Filter Files in a Specified Folder for FDR Simulations in ADS

```
flow = 1000*input('enter lowest frequency of the bandwidth of interest in GHz');
fhigh =1000*input('enter highest frequency of the bandwidth of interest in GHz');
cd 'C:\Users\ismailuluer\Desktop\BPF';      % give the home directory
for aa=flow:1:fhigh                          % creates files with 0.001 GHz steps
   cc=aa/1000;
   currentFolder = sprintf('%.3f',cc);
   mkdir(currentFolder);
   cd(currentFolder);
   for xx=1:1:4                              %number of harmonics (4)
      yy=aa*xx/1000;
      str = sprintf('%.3f.txt',yy);
      fid = fopen(str,'wt');
      fprintf(fid,'!\tFrequency\tS11\tS21\tS12\tS22\n');
      fprintf(fid,'#\tHZ\tS\tDB\tR\t50\n');
      for bb=0:100:(flow-1)
         fprintf(fid,'%.3fE+09\t0\t0\t-1000\t0\t-1000\t0\t0\t0\n', bb/1000);
      end
      for bb=flow:1:fhigh*4
         if (xx==1 && bb ==1*aa)
               fprintf(fid,'%.3fE+09\t-1000\t0\t0\t0\t0\t0\t-1000\t0\n', bb/1000);
         elseif (xx==2 && bb ==2*aa)
               fprintf(fid,'%.3fE+09\t-1000\t0\t0\t0\t0\t0\t-1000\t0\n', bb/1000);
         elseif (xx==3 && bb ==3*aa)
               fprintf(fid,'%.3fE+09\t-1000\t0\t0\t0\t0\t0\t-1000\t0\n', bb/1000);
         elseif (xx==4 && bb ==4*aa)
               fprintf(fid,'%.3fE+09\t-1000\t0\t0\t0\t0\t0\t-1000\t0\n', bb/1000);
         else
               fprintf(fid,'%.3fE+09\t0\t0\t-1000\t0\t-1000\t0\t0\t0\n', bb/1000);
         end
      end
   fclose(fid);
   end
   cd 'C:\Users\ismailuluer\Desktop\BPF';        %back to home directory
end
```

Appendix B : Interrogator Antenna (Horn Antenna) Gain vs. Frequency

Frequency[Hz]	Gain [dBi]
6.00000000E+08	-3.52330501E+00
6.50000000E+08	4.66563211E-01
7.00000000E+08	3.62584146E+00
7.50000000E+08	5.40704455E+00
8.00000000E+08	6.18967565E+00
8.50000000E+08	6.55854509E+00
9.00000000E+08	6.74347685E+00
9.50000000E+08	6.81485589E+00
1.00000000E+09	6.81714888E+00
1.05000000E+09	6.76833313E+00
1.10000000E+09	6.66248178E+00
1.15000000E+09	6.52628801E+00
1.20000000E+09	6.46458016E+00
1.25000000E+09	6.57922459E+00
1.30000000E+09	6.88001020E+00
1.35000000E+09	7.30410020E+00
1.40000000E+09	7.76848039E+00
1.45000000E+09	8.19993131E+00
1.50000000E+09	8.55431131E+00
1.55000000E+09	8.81752064E+00
1.60000000E+09	8.99674738E+00
1.65000000E+09	9.10501383E+00
1.70000000E+09	9.14836286E+00
1.75000000E+09	9.11434248E+00
1.80000000E+09	8.95215188E+00
1.85000000E+09	8.54504718E+00
1.90000000E+09	7.72081580E+00
1.95000000E+09	6.68214422E+00
2.00000000E+09	6.75728202E+00
2.05000000E+09	7.95669341E+00
2.10000000E+09	8.90786619E+00
2.15000000E+09	9.49278791E+00
2.20000000E+09	9.98348861E+00
2.25000000E+09	1.03615819E+01
2.30000000E+09	1.05916325E+01
2.35000000E+09	1.06235074E+01
2.40000000E+09	1.05706097E+01
2.45000000E+09	1.05173241E+01
2.50000000E+09	1.04725636E+01

Appendix C : Copyright Permissions

a) Permission for Chapter II:

CCC RightsLink

Home Help Live Chat Sign in Create Account

IEEE Requesting permission to reuse content from an IEEE publication

Battery-free Mechanically-Tunable Wireless Sensors for Railroad Track Ballast Monitoring

Conference Proceedings: 2022 IEEE International Symposium on Antennas and Propagation and USNC-URSI Radio Science Meeting (AP-S/URSI)
Author: Ismail H. Uluer
Publisher: IEEE
Date: 10 July 2022

Thesis / Dissertation Reuse

The IEEE does not require individuals working on a thesis to obtain a formal reuse license, however, you may print out this statement to be used as a permission grant:

Requirements to be followed when using any portion (e.g., figure, graph, table, or textual material) of an IEEE copyrighted paper in a thesis:

1) In the case of textual material (e.g., using short quotes or referring to the work within these papers) users must give full credit to the original source (author, paper, publication) followed by the IEEE copyright line © 2011 IEEE.
2) In the case of illustrations or tabular material, we require that the copyright line © [Year of original publication] IEEE appear prominently with each reprinted figure and/or table.
3) If a substantial portion of the original paper is to be used, and if you are not the senior author, also obtain the senior author's approval.

Requirements to be followed when using an entire IEEE copyrighted paper in a thesis:

1) The following IEEE copyright/ credit notice should be placed prominently in the references: © [year of original publication] IEEE. Reprinted, with permission, from [author names, paper title, IEEE publication title, and month/year of publication]
2) Only the accepted version of an IEEE copyrighted paper can be used when posting the paper or your thesis on-line.
3) In placing the thesis on the author's university website, please display the following message in a prominent place on the website: In reference to IEEE copyrighted material which is used with permission in this thesis, the IEEE does not endorse any of [university/educational entity's name goes here]'s products or services. Internal or personal use of this material is permitted. If interested in reprinting/republishing IEEE copyrighted material for advertising or promotional purposes or for creating new collective works for resale or redistribution, please go to http://www.ieee.org/publications_standards/publications/rights/rights_link.html to learn how to obtain a License from RightsLink.

If applicable, University Microfilms and/or ProQuest Library, or the Archives of Canada may supply single copies of the dissertation.

BACK CLOSE WINDOW

b) Permission for Chapter III:

CCC RightsLink

Home Help Live Chat Sign in Create Account

IEEE Requesting permission to reuse content from an IEEE publication

A Semi-Empirical Model for Predicting the Effects of Moisture on Microwave Signal Attenuation in Fouled Railroad Ballast

Conference Proceedings: 2022 IEEE 22nd Annual Wireless and Microwave Technology Conference (WAMICON)
Author: Ismail H. Uluer
Publisher: IEEE
Date: 27 April 2022

Thesis / Dissertation Reuse

The IEEE does not require individuals working on a thesis to obtain a formal reuse license, however, you may print out this statement to be used as a permission grant:

Requirements to be followed when using any portion (e.g., figure, graph, table, or textual material) of an IEEE copyrighted paper in a thesis:

1) In the case of textual material (e.g., using short quotes or referring to the work within these papers) users must give full credit to the original source (author, paper, publication) followed by the IEEE copyright line © 2011 IEEE.
2) In the case of illustrations or tabular material, we require that the copyright line © [Year of original publication] IEEE appear prominently with each reprinted figure and/or table.
3) If a substantial portion of the original paper is to be used, and if you are not the senior author, also obtain the senior author's approval.

Requirements to be followed when using an entire IEEE copyrighted paper in a thesis:

1) The following IEEE copyright/ credit notice should be placed prominently in the references: © [year of original publication] IEEE. Reprinted, with permission, from [author names, paper title, IEEE publication title, and month/year of publication]
2) Only the accepted version of an IEEE copyrighted paper can be used when posting the paper or your thesis on-line.
3) In placing the thesis on the author's university website, please display the following message in a prominent place on the website: In reference to IEEE copyrighted material which is used with permission in this thesis, the IEEE does not endorse any of [university/educational entity's name goes here]'s products or services. Internal or personal use of this material is permitted. If interested in reprinting/republishing IEEE copyrighted material for advertising or promotional purposes or for creating new collective works for resale or redistribution, please go to http://www.ieee.org/publications_standards/publications/rights/rights_link.html to learn how to obtain a License from RightsLink.

If applicable, University Microfilms and/or ProQuest Library, or the Archives of Canada may supply single copies of the dissertation.

BACK CLOSE WINDOW

c) Permission for Chapter V:

CCC RightsLink

Home Help Live Chat Sign in Create Account

An X-Band Dielectric Rod Antenna for Subdermal Tumor Heating to Assist Electroporation-Mediated DNA Delivery

Author: Ismail H. Uluer
Publication: IEEE Journal of Electromagnetics, RF and Microwaves in Medicine and Biology
Publisher: IEEE
Date: December 2021

Thesis / Dissertation Reuse

The IEEE does not require individuals working on a thesis to obtain a formal reuse license, however, you may print out this statement to be used as a permission grant:

Requirements to be followed when using any portion (e.g., figure, graph, table, or textual material) of an IEEE copyrighted paper in a thesis:

1) In the case of textual material (e.g., using short quotes or referring to the work within these papers) users must give full credit to the original source (author, paper, publication) followed by the IEEE copyright line © 2011 IEEE.
2) In the case of illustrations or tabular material, we require that the copyright line © [Year of original publication] IEEE appear prominently with each reprinted figure and/or table.
3) If a substantial portion of the original paper is to be used, and if you are not the senior author, also obtain the senior author's approval.

Requirements to be followed when using an entire IEEE copyrighted paper in a thesis:

1) The following IEEE copyright/ credit notice should be placed prominently in the references: © [year of original publication] IEEE. Reprinted, with permission, from [author names, paper title, IEEE publication title, and month/year of publication]
2) Only the accepted version of an IEEE copyrighted paper can be used when posting the paper or your thesis on-line.
3) In placing the thesis on the author's university website, please display the following message in a prominent place on the website: In reference to IEEE copyrighted material which is used with permission in this thesis, the IEEE does not endorse any of [university/educational entity's name goes here]'s products or services. Internal or personal use of this material is permitted. If interested in reprinting/republishing IEEE copyrighted material for advertising or promotional purposes or for creating new collective works for resale or redistribution, please go to http://www.ieee.org/publications_standards/publications/rights/rights_link.html to learn how to obtain a License from RightsLink.

If applicable, University Microfilms and/or ProQuest Library, or the Archives of Canada may supply single copies of the dissertation.

BACK CLOSE WINDOW

d) Permission for Chapter VI:

CCC RightsLink

Home Help Live Chat Sign in Create Account

Dielectric Lens Designs for Antenna Beam Shaping in a Subdermal Tumor Treatment Device

Conference Proceedings: 2021 IEEE MTT-S International Microwave Symposium (IMS)
Author: Ismail H. Uluer
Publisher: IEEE
Date: 07 June 2021

Thesis / Dissertation Reuse

The IEEE does not require individuals working on a thesis to obtain a formal reuse license, however, you may print out this statement to be used as a permission grant:

Requirements to be followed when using any portion (e.g., figure, graph, table, or textual material) of an IEEE copyrighted paper in a thesis:

1) In the case of textual material (e.g., using short quotes or referring to the work within these papers) users must give full credit to the original source (author, paper, publication) followed by the IEEE copyright line © 2011 IEEE.
2) In the case of illustrations or tabular material, we require that the copyright line © [Year of original publication] IEEE appear prominently with each reprinted figure and/or table.
3) If a substantial portion of the original paper is to be used, and if you are not the senior author, also obtain the senior author's approval.

Requirements to be followed when using an entire IEEE copyrighted paper in a thesis:

1) The following IEEE copyright/ credit notice should be placed prominently in the references: © [year of original publication] IEEE. Reprinted, with permission, from [author names, paper title, IEEE publication title, and month/year of publication]
2) Only the accepted version of an IEEE copyrighted paper can be used when posting the paper or your thesis on-line.
3) In placing the thesis on the author's university website, please display the following message in a prominent place on the website: In reference to IEEE copyrighted material which is used with permission in this thesis, the IEEE does not endorse any of [university/educational entity's name goes here]'s products or services. Internal or personal use of this material is permitted. If interested in reprinting/republishing IEEE copyrighted material for advertising or promotional purposes or for creating new collective works for resale or redistribution, please go to http://www.ieee.org/publications_standards/publications/rights/rights_link.html to learn how to obtain a License from RightsLink.

If applicable, University Microfilms and/or ProQuest Library, or the Archives of Canada may supply single copies of the dissertation.

BACK CLOSE WINDOW